Fourier Transform Spectroscopic Demodulation of Fibre Bragg Grating Arrays

by

Kieran O'Mahoney

Submitted for the Degree of
Doctor of Philosophy

to

School of Science
Waterford Institute of Technology

Supervisors:

Dr. D. A. Flavin, Dr. C. Keary and Dr. P. J. Cregg
(Waterford Institute of Technology)

Prof. J. D. C. Jones
(Heriot-Watt University, Edinburgh, Scotland)

(July, 2007)

Declaration

No part of the work described in this thesis, or the thesis itself, has been submitted as an exercise for a degree at this or any other institution.

The work herein has been performed entirely by the author.

Kieran O'Mahoney.

July 2007.

In memory of

Donal Flavin (R.I.P.)

Acknowledgements

I owe a great deal of gratitude to many people who have contributed to my completing this body of work. To my supervisor, Dónal Flavin (R.I.P.), whose infectious enthusiasm extended beyond the field of optics, and encouraged me to continue on the journey to completion of this thesis.

To my co-supervisors who assumed the mantle left behind: Dr. Claire Keary and Dr. P. J. Cregg from Waterford Institute of Technology and Professor Julian Jones and Dr. William MacPherson from the Applied Optics and Photonics Group, Heriot-Watt University, Edinburgh, Scotland. I express my gratitude for your insight, guidance and continual support.

A special acknowledgement must go to Claire and Bill, who gave their time and assistance freely to aid in the completion of this thesis; I am deeply indebted and will never be able to repay.

My thanks also to the members of the Optics Research Group, John Rothwell, Ronan O'Byrne, Sergey Sergeyev and Mohammad Alhourani. In particular to John, with whom I spent five enjoyable years working in the optics lab, and Mohammad for his friendly and insightful assistance.

I would also like to thank the staff at Aston University, Birmingham, UK, where I spent an enjoyable summer performing experiments in a collaborative project with the Photonics Research Group. Most notably, I would like to thank Professor Ian Bennion and Dr. David Webb for affording me the opportunity to work with such a friendly and capable research team. Dr. Tom Allsop and Andy Main who welcomed me without reservation and were always on hand to offer advice or help with experimental set-ups and the interpretation of results.

My gratitude also goes to the staff of W.I.T. where I carried out most of the work for this thesis; the staff members of the Research and Development Office, the School of Science Office, and the Head of Department of Computing, Mathematics and Physics, Dr. Mícheál ÓhÉigeartaigh, for their support; to Frank O'Donnell and Michael Phelan for technical support whenever required; to Billy Walsh and Damien Kelly in the Electronics Department for the endless supply of electronic components; to Micheal McCarthy for his computing and engineering insight; and finally to Mairéad Meagher for proof reading this work.

I would also like to thank my parents, brother and sisters for their support throughout the duration of this work.

Last, but certainly not least, I would like to make a special thanks to Cecilia for her tolerance, encouragement and support.

Publications

The work reported in this thesis has been presented at the following international conferences:

[1] K. T. O'Mahoney, D. A. Flavin, L. Zhang, and I. Bennion., "Fourier transform-based spectral measurements on multiplexed fibre Bragg grating arrays," in *Proceedings of S.P.I.E. Second European Workshop on Optical Fibre Sensors, vol. 5502* (B. Culshaw, ed.), (Santander, Spain), pp. 423–426, 2004.

[2] K. T. O'Mahoney, D. A. Flavin, L. Zhang, and I. Bennion, "High-resolution interferometric spectroscopy for analysis of fibre Bragg grating sensor arrays." Opto-Ireland, Optical Sensing and Spectroscopy, Oral Presentation, April 2005.

[3] K. T. O'Mahoney, D. A. Flavin, L. Zhang, and I. Bennion, "Demodulation of serial fibre Bragg grating arrays by Fourier transform spectroscopy using an over-moded laser reference," in *Proceedings of S.P.I.E. 17th International Conference on Optical Fibre Sensors, vol. 5855* (M. Voet, R. Willsch, W. Ecke, J. Jones, and B. Culshaw, eds.), (Brugges, Belgium), pp. 651–654, May 2005.

[4] K. T. O'Mahoney, A. S. Main, D. J. Webb, A. Martinez, and D. A. Flavin, "Implications of high-power losses in IR femtosecond laser inscribed fiber Bragg gratings," in *Proceedings of S.P.I.E. Reliability of Optical Fiber Components, Devices, Systems, and Networks III, vol. 6193* (H. G. Limberger and M. J. Matthewson, eds.), (Strasbourg, France), May 2006.

Abstract

The application of interferometric techniques to the measurement of the thermal and strain induced shift in the resonant reflected wavelengths from an in-fibre Bragg grating array is reported in this thesis.

High power issues relating to the reliability, and subsequently to the interrogation techniques, of fibre Bragg gratings inscribed with an infrared femtosecond laser using the point-by-point writing method are reported. The study has revealed the presence of broad spectrum power losses. When high powers are used, even at wavelengths far removed from the Bragg condition, these losses produce an increase in the fibre temperature due to absorption in the coating.

The principal interest of the work is in the application of Fourier Transform Spectroscopy and Hilbert Transform Processing techniques to the calibration of interferometric delay and to provide simultaneous, high resolution measurement of all gratings in an array. These approaches are applied to interferograms captured using customised interferometric configurations. The interferometric delay is scanned by mechanical means. Calibration is based on recovery of the temporal phase vectors of the interferograms from which non-uniform delay sampling is corrected for using the temporal phase vector obtained from a reference interferogram.

This thesis demonstrates the efficacy of the Hilbert transform processing approach for long-scan delay calibration (1.2 ns delay). A referencing system based on a multiple transverse mode beam, allowing co-propagation with the measurand beam through the demodulating interferometer, is also demonstrated to provide identical Fourier transform spectral measurements.

The Hilbert transform approach to grating interrogation is also applied to an all-fibre interferometric configuration to provide ~ 3 pm wavelength resolution. The Hilbert transform technique bases measurement on the ratio of reference and measurand temporal phase vectors, providing measurement of the mean reflected wavelength of the gratings. A scheme where the reference interferogram for the all-fibre interferometer is generated by a fibre Bragg grating is also evaluated.

Contents

1 Introduction **1**

1.1 Optical Fibre Sensors 1

1.1.1 Background 1

1.1.2 Problem Definition 2

1.2 Methodology, Objectives and Scope 3

1.3 Thesis Overview 5

1.3.1 Literature Survey 5

1.3.2 Implications of high power losses in near infrared femtosecond laser inscribed fibre Bragg gratings 6

1.3.3 Long-scan Hilbert Transform Interferometric Delay Calibration . . 6

1.3.4 Long OPD Fourier Transform Spectroscopic demodulation of FBG sensors arrays 7

1.3.5 High Speed Bragg Grating Sensor Array Demodulator for Structural Health Monitoring 7

1.3.6 Conclusion 8

2 Review **11**

2.1 Optical Fibre Sensing 13

2.1.1 Wave Nature of Light 13

2.1.2 Fibre Structures and Modes 14

2.1.3 Electromagnetic Fields within Optical Waveguides 15

2.1.4 Optical Fibre Materials 18

2.1.5 Optical Fibre Losses 19

2.1.6 Optical Fibre Reliability 24

2.1.7 Fibre Optic Couplers 25
2.1.8 Fibre Optic Sensing 26
2.1.9 Modulating Effects in Fibre Sensors 28
2.1.10 Fibre Bragg Gratings 33
2.1.11 Operational Principles 35
2.1.12 FBG Fundamentals 39
2.1.13 Grating Manufacture 42
2.1.14 Classification of Fiber Bragg Gratings According to Photosensitisation 46
2.1.15 Grating Characterisation 48
2.1.16 FBG Interrogation Schemes 48
2.2 Optical Measurement 50
2.2.1 Coherence and Interference 51
2.2.2 Temporal and Spatial Coherence 51
2.2.3 Interference 52
2.2.4 Mutual Coherence and the Degree of Coherence 53
2.2.5 Polarization 55
2.2.6 Interferometry 57
2.2.7 Michelson Interferometer 57
2.2.8 Mach-Zehnder Interferometer 59
2.2.9 Interferometric Fourier Transform Spectroscopy 61
2.2.10 Hilbert Transform Technique for OPD Calibration 62
2.2.11 The Fourier Transform 62
2.2.12 The Hilbert Transform and the Analytic Signal 64
2.3 Summary and Context of Experimental Work 66

3 Implications of high power losses in IR femtosecond laser-inscribed fibre Bragg gratings 80

3.1 Introduction 80

3.1.1 Fibre Reliability 81
3.1.2 Fibre Bragg Gratings 82
3.1.3 FBG Inscription 82
3.2 Experimental Motivation and Objectives 83
3.3 Experimental Configuration 84
3.3.1 Mach Zehnder Interferometer 85
3.3.2 Optical Spectrum Analyser 89
3.4 Results and Discussion 90
3.4.1 Interferometric Analysis 90
3.4.2 OSA Observations 94
3.5 Discussion 97
3.6 Conclusion 99

4 Long-scan Hilbert Transform Interferometric Delay Calibration 103

4.1 Introduction 103
4.1.1 Fourier Transform Spectroscopy 104
4.1.2 Interferometric Fourier Transform Spectroscopy 106
4.1.3 Hilbert Transform Technique for OPD Calibration 107
4.1.4 Beam Collinearity 108
4.2 Experimental Motivation and Objectives 110
4.3 Experimental Configuration 111
4.4 Results and Discussion 113
4.4.1 Results 113
4.4.2 Discussion 118
4.5 Conclusion 119

5 Long Optical Path Difference Fourier Transform Spectroscopic demodulation of Fibre Bragg Grating sensor arrays

122

5.1 Introduction 122

5.1.1 Fibre Bragg Gratings 124

5.2 Experimental Motivation and Objectives 129

5.3 Experimental Configuration 129

5.4 Results and Discussion 131

5.4.1 Discussion 135

5.5 Conclusion 138

6 High Speed Bragg Grating Sensor Array Demodulator for Structural Health Monitoring 143

6.1 Introduction 143

6.1.1 Hilbert Transform Spectroscopy 144

6.1.2 Experimental Motivation and Objectives 147

6.2 Experimental Configuration 148

6.3 Results and Discussion 150

6.3.1 Results 150

6.3.2 Application to the Single Parameter Sensing of Temperature 153

6.3.3 Discussion 162

6.4 Conclusion 163

7 Conclusion 168

7.1 Achievement of Objectives 168

7.2 Summary of Results 171

7.3 Future Investigations 172

A Electromagnetic Wave Theory 176

List of Figures

2.1 Typical optical fibre 14

2.2 Representation of Skew modes propagating around the central axis of the fibre. 17

2.3 Plot of Bessel function of the first kind, J_l (x), for integer orders $l = 0, 1, 2$. . 17

2.4 Silica fibre losses due to absorption and scattering. The loss of the fibre at 1.55 μ m (0.2 $dBkm^{-1}$) is very close to the fundamental limit imposed by Rayleigh scattering. [Figure obtained from [14]] 20

2.5 The basic scheme for a fibre-optic gyroscope. 32

2.6 Standard UV inscription of FBGs. 44

2.7 Two beam interferometer illuminated by an extended source S [3, 64] . . . 53

2.8 Customised version of Michelson Interferometer 58

2.9 All-fibre Mach-Zehnder Interferometer 59

2.10 Illustration of the effect of non-uniform delay sampling: the number of sample points per fringe varies with scanning velocity. 66

3.1 Experimental configuration: The output from a Mach-Zehnder interferometer illuminates the sensing and reference gratings for comparison by the lock-in amplifier. 85

3.2 Output from a Mach-Zehnder interferometer illuminated by a broadband source and recorded by an Optical Spectrum Analyser. 86

3.3 Illustration of output from Mach-Zehnder interferometer as the OPD is scanned through its FSR. 87

3.4 Demodulation by OSA 89

3.5 Transmitted power versus applied power for 7 different gratings measured at the Raman laser output of 1455 nm as the power levels are increased to ~ 1.5 - 2 W 90
3.6 Phase change recorded by two gratings when subjected to temperature increases from room temperature to ~ 100°C. The slope of a linear fit to the ST10 data gives the change in phase per °C 91
3.7 Phase change and corresponding temperature change recorded for 4 gratings at high powers. 92
3.8 Phase change of grating BT2 with increase in laser power from 0 to 4.5W . 94
3.9 Phase change of grating ST9 with increase in laser power from 0 to 4.5W . 94
3.10 Spectrum of a NIR femtosecond laser inscribed grating being chirped when power levels in the fibre are increased from 0- 4.5W 95
3.11 Grating spectrum with 0 W Raman power launched down fibre. 96
3.12 Spectrum recorded by OSA at buffer melting point of 2.5 W 96
3.13 Comparison of spectra (no power) before (—) and after (-·-) melting of buffer 97
3.14 Comparison of spectra before (—) and after melting of the buffer (-·-) at 1.135 W 97

4.1 3D representation of the sinc function 105
4.2 The 2D Sinc function 106
4.3 Co-propagating reference and measurand beams in a Michelson interferometer 109
4.4 Long FTS Experimental configuration 112
4.5 Typical spectral response curves for silicon (~ 400 - 1100 nm) and InGaAs (~ 900 - 1700 nm) photodetectors. [Data obtained from [14]] 113
4.6 Interferograms obtained from (A) the singlemode and (B) the overmode beams. 114

4.7 Multimode beam intensity profile obtained an a Dalsa piranha linescan camera. 114
4.8 Cross section of the multimode beam taken with a Dalsa piranha linescan camera. 114
4.9 (A) Section of an interferogram obtained from the singlemode source. (B) High frequency content of the interferogram obtained from the boxed section of (A). 115
4.10 (A) Section of an interferogram obtained from the multimode source. (B) High frequency content of the interferogram obtained from the boxed section of (A). 115
4.11 Spectrum of the overmode interferogram before recalibration 115
4.12 Unwrapped temporal phase vector 116
4.13 Residual to fit to phase before recalibration 117
4.14 Residual to fit to phase after recalibration 117
4.15 Spectra derived from 360 mm OPD sections of the singlemode and overmode interferograms 117

5.1 Standard UV inscription of an array of FBGs. 124
5.2 FTS for demodulation of FBG arrays 130
5.3 Composite interferogram from HeNe and array 132
5.4 Interferogram obtained from 1538 nm grating alone 132
5.5 High frequency content of the composite interferogram. 132
5.6 Magnitude of the Fourier transform of the composite interferogram before recalibration 132
5.7 Magnitude of the Fourier transform of the composite interferogram after recalibration 132
5.8 1549 grating under temperature modulation 134
5.9 Quadratic dependence of Bragg wavelength to temperature. 134

5.10 Comparison of spectral detail recorded using singlemode and overmode beams . . . 134
5.11 1538 nm grating with induced chirp . . . 135
5.12 Comparison of spectral detail of chirp recorded using singlemode and overmode beams . . . 135

6.1 All-fibre demodulator for structural health monitoring. . . . 149
6.2 Pulsed sawtooth waveform applied to drive the piezoelectric controller. . 150
6.3 Interferograms obtained from the reference laser and reference grating using a sawtooth waveform applied to the demodulator of Figure 6.1 . . . 151
6.4 Phase residuals before and after recalibration . . . 151
6.5 Comparison of spectral measurements obtained using both a laser and grating reference . . . 152
6.6 Residual to a fit to the recorded resonant wavelength of the reference grating referenced from a highly stable (< 1 pm) 1534 nm telecoms laser . 153
6.7 Interferogram obtained from the grating array when a sawtooth waveform applied to the demodulator of Figure 6.1 . . . 153
6.8 Results recorded by gratings subjected to a temperature change from ~ 20^oC - 50^oC referenced from a 1534.14 nm laser and from the 1566.46 nm grating. . . . 154
6.9 Sine wave applied to the piezoelectric stretcher to generate a series of interferograms. . . . 155
6.10 All-fibre interferometer output with sinusoidal waveform applied to the piezoelectric stretcher. . . . 156
6.11 Magnitude of the Fourier transforms of the measurand and reference interferograms . . . 157
6.12 Magnitude of the Fourier transforms of the measurand and reference interferograms after OPD calibration . . . 158
6.13 Unwrapped phase vectors and residuals . . . 159

6.14 Results recorded by gratings subjected to a temperature change from 7°C to 88°C. 160
6.15 Results recorded by gratings subjected to 10 $\mu\epsilon$ steps, referenced from a 1534.14 nm reference laser and referenced from the 1566.46 nm reference grating. 161

Glossary of Terms

CW	Continuous Wave
DFT	Discrete Fourier Transform
DWDM	Dense Wavelengh Division Multiplexed
FBG	Fibre Bragg Grating
FT	Fourier Transform
FTS	Fourier Transform Spectroscopy
FOG	Fibre Optic Gyroscope
FOS	Fibre Optic Sensors
FSR	Free Spectral Range
FWHM	Full Width at Half Maximum
HeNe	Helium Neon
HTP	Hilbert Transform Processing
HTT	Hilbert Transform Technique
IFTS	Interferometric Fourier Transform Spectroscopy
InGaAs	Indium Gallium Arsenide
LPG	Long Period Grating
MZI	Mach-Zehnder Interferometer
NIR	Near Infrared
OLCR	Optical Low Coherence Reflectometry
OPD	Optical Path Difference
OSA	Optical Spectrum Analyser
PCF	Photonic Crystal Fibre
PCS	Plastic Coated Silica
SLED	Superluminescent Light Emitting Diode
SHM	Structural Health Monitoring
TE	Transverse Electric
TIR	Total Internal Reflection
TM	Transverse Magnetic
UMZI	Unbalanced Mach-Zehnder Interferometer
UV	Ultraviolet
WDM	Wavelength Division Multiplexed

Chapter 1

Introduction

1.1 Optical Fibre Sensors

1.1.1 Background

In the optical sensing community, there has been intense interest in the interaction of light with both itself and matter for sensing of measurand-induced environmental changes. Smart sensing is a recent and fast growing field of optical metrology and is closely linked to the field of structural health monitoring, which is typically implemented using optical fibre sensors. Fibre Optic Sensors (FOS) exhibit significant advantages over conventional electro-mechanical sensors such as high electromagnetic immunity, measurement of a wide range of measurands, small size and high sensitivity. Ideally, these sensors would be accompanied by a series of actuators to allow a structure to compensate or correct for any changes in position, strain or temperature which deviate from its position of equilibrium.

Fibre Bragg gratings (FBG) represent a key element in the field of optical fibre sensors. From the earliest stage of their development, fibre Bragg gratings have been considered for use as sensor elements capable of providing quasi-distributed sensing, suitable for measuring static and dynamic fields such as temperature [1], strain [2] and pressure [3]. They have become an important component in the development of smart structure technology. The key advantage of fibre Bragg gratings over other optical fibre sensors is that the measurand is directly encoded in the reflected wavelength. Since the wavelength is an absolute parameter, the signal returned from the FBG can be processed such that its information remains immune to power fluctuations along the op-

tical path. In addition, gratings can be written using a variety of inscription methods at well defined wavelengths. They can operate over application-specific ranges making them most suitable to wavelength division multiplexed (WDM) approaches. As such any interrogation system should be compatible with multiplexing, so as to reduce costs and take advantage of the suitability of these sensors for quasi-distributed sensing.

Individual lightwaves have oscillation frequencies that are too high to be individually detected with currently available technologies. Therefore, sub-wavelength resolution measurements have been obtained by means other than direct measurement of the lightwave. Fourier transform spectroscopy (FTS) is a measurement technique which bases spectral measurements on the temporal coherence of a radiative source. Interferometric spectroscopy, which is typically implemented as FTS, forms the basis for sub-wavelength resolution measurements to be made by direct comparison of a lightwave with itself or a delayed version of itself. FTS has been widely used in spectral measurement but high resolution measurement requires long delay scans. Furthermore, if the interferograms are sampled at uniform delay intervals, the modulus of the FFT is the spectrum of the reflected signals from the gratings. In practice, the delay scans are never sufficiently uniform. This broadens the peaks due to the individual gratings, thus reducing the number of gratings which can be multiplexed.

1.1.2 Problem Definition

Reliability issues have been a concern with standard ultraviolet (UV) inscribed fibre Bragg gratings because of the requirement that the buffer is stripped from the fibre due to a sensitivity to the UV light. This results in a reduction of the mechanical strength of the fibre. The development of inscription techniques by near infrared laser has removed this requirement, but there is a need for reliability testing of these gratings, particularly for use in high power applications. The telecommunications industry has adopted Fibre Bragg gratings for use in a variety of capacities such as filtering and multiplexing, dispersion compensation, amplifier gain flattening and wavelength stabilisation [4]. The reflected wavelength of the grating and the grating bandwidth's stability

assumes a greater significance as power levels increase in order to cater for the demand for greater bandwidths.

The capability to measure a grating's reflected wavelength, bandwidth and wavelength stability has also significance outside the field of optical sensing. FTS has the capability to provide the required high resolution measurements, not only on individual gratings, but on arrays of gratings multiplexed along the length of a single fibre [5].

The associated Hilbert transform technique (HTT), has been shown to generate far higher resolution over shorter optical path difference (OPD) scans. The technique provides measurement of the mean reflected wavelength of the grating [6, 7], but without measurement of the spectral detail of the individual gratings. HTT processing also overcomes the non-uniform scan velocity problem entirely in software (with no additional hardware requirements), while allowing for dense multiplexing of gratings.

The efficacy of HTT processing for calibration of interferometric optical path length over far longer delay scans than previously reported needs to be investigated for FTS applications. Such a demodulation system could provide high resolution measurement of the intra-grating spectral detail, which may be potentially valuable in the detection of non-uniform measurand fields [8].

The cost of demodulation systems in general for fibre optic sensors remains high. In the case of interferometric interrogation units, there is a need to develop demodulation systems which are not hindered by cumbersome translation stages, and which contain a reduced number of components thereby increasing the portability of the interrogation system. Such a portable demodulation scheme would be potentially useful in applications such as structural health monitoring, while at the same time maintaining the capability for demodulation over broad wavelength ranges.

1.2 Methodology, Objectives and Scope

Initially, a literature survey was conducted to determine the state-of-the-art of sensing applications of fibre Bragg gratings and interferometric interrogation systems used

for demodulation of grating arrays. Firstly, the operating principles of the Michelson interferometer were studied and an experimental bulk optic version of the interferometer and associated electronics designed. The aim of this experimental work was to determine, and then limit, sources of noise and sources of error in the interferometric configuration.

The operating principles of a single fibre Bragg grating had then to be examined, focusing on their functionality and implementation in various sensor configurations and previous applications of the devices. A working knowledge of fibre photosensitisation, fibre grating fabrication methods and reliability issues pertaining to fibre components were also garnered at this stage of the review.

A collaborative, experimental project, involving Aston University, Birmingham, and British Telecom, in which Bragg gratings were implemented in a sensing capacity revealed some relevant issues pertaining to the work conducted in later chapters. The aim of the investigation was to profile the temperature threshold for damage to occur to fibres in tight bend situations when subjected to high optical powers [9]. This experimental work led to some observations on the reliability of near infrared femtosecond laser inscribed fibre Bragg gratings when used in high power applications. In particular, it led to observations on the reliability of measurements made on interrogation systems which do not readily lend themselves to demodulation over broad wavelength ranges. Near infrared inscribed gratings were chosen as the sensing elements for this experimental work as there are reliability issues with standard ultraviolet inscribed gratings because of a requirement to strip the buffer off the fibre prior to inscription [10].

FTS requires long optical path difference scans to provide high resolution measurements [11]. Therefore, the next stage of the experimental work was to determine the capacity for the Hilbert transform technique for calibration of optical path delay in the long-scan case. In addition, an investigation of a method to reduce the error introduced in the long-scan case, caused by non-parallel propagating measurand and reference beams, where co-propagating reference and measurand beams were present

in the demodulating interferometer [7] was undertaken. This work resulted in the use of what has been termed an 'overmoded' reference beam propagating in the demodulating interferometer.

The interferometric techniques developed in the long-scan case were then applied to the demonstration of the effectiveness of FTS measurements on fibre Bragg gratings. This was done to provide repeatable high resolution measurements of the intra-grating structural detail of the gratings, which could be potentially valuable in the detection of non-uniform measurand fields [8]. The measurements made using the 'overmoded' reference were then evaluated relative to measurements made using a singlemode reference.

The final component of experimental work described was the development of a high speed, portable, grating-referenced demodulator for interrogation of grating arrays. Typically, referencing of the reflected Bragg wavelength is obtained using a narrow linewidth source, while high reflectivity gratings have bandwidths ~ 500 pm. A narrow linewidth (~ 40 pm), low reflectivity, grating was manufactured in Aston University to serve as the reference in this work. An all-fibre Michelson interferometer was chosen as the interferometric configuration to reduce the number of bulk optic components in the interferometer and render it immune to vibration.

1.3 Thesis Overview

1.3.1 Literature Survey

Chapter 2 offers a review of the fields of interferometry and optical sensing with particular focus on sensing using fibre Bragg gratings. A number of different techniques for fibre Bragg grating array demodulation are discussed. Their merits and demerits are analyzed and compared to the interferometric methods which are the subject of the later chapters in this thesis. The theory of the processing techniques, which are based on high resolution measurement of temporal phase, and are the basis for the experimental work, is developed from coherence theory. Particular attention is paid

to Fourier Transform Spectroscopy and the associated Hilbert transform technique for correction of spectral degradation arising from mechanical path length scanning of the interferometric optical path difference.

1.3.2 Implications of high power losses in near infrared femtosecond laser inscribed fibre Bragg gratings

Chapter 3 investigates reliability issues surrounding fibre optic components and in particular the implications of high power losses in near infrared femtosecond laser inscribed fibre Bragg gratings. The effects of the losses on the gratings have far reaching consequences for use in telecommunications applications, where wavelength stability is of concern in high power applications and also in sensing applications for measurement of non-uniform measurand fields. The consequences of the losses are investigated using both a commercial spectrometer and a Mach Zehnder interferometric configuration. The implications of these losses illustrate the potential problems associated with demodulation schemes which are not capable of interrogation over broad wavelength ranges.

1.3.3 Long-scan Hilbert Transform Interferometric Delay Calibration

Chapter 4 investigates the efficacy of the Hilbert transform technique for correction of spectral degradation arising from non-uniform scanning of the interferometric OPD in the **long-scan** case. Long OPD scans are required to provide high resolution Fourier transform spectroscopic measurements. Conventionally, OPD calibration is conducted using a single transverse mode reference laser which propagates parallel to the measurand beam in the interferometer [6, 7, 12–14].

In this chapter, the ability of the Hilbert transform technique to calibrate optical path length scanning when the reference beam propagates in more than one transverse mode is also investigated. This technique allows for propagation of both measurand and reference beams along identical paths in the interferometer.

1.3.4 Long OPD Fourier Transform Spectroscopic demodulation of FBG sensors arrays

Chapter 5 investigates the capability of **long-scan** Fourier transform spectroscopy using a customised Michelson interferometer for demodulation of fibre Bragg grating sensor arrays with simultaneous recovery of the spectral detail of all gratings in the array in a single scan of the interferometric OPD. The efficacy of a scheme for array demodulation based on the collinear propagation of the reference and Bragg grating beams in the demodulating interferometer is also demonstrated.

Previously reported applications of co-linearly launched reference and measurand beams have either used a zero-crossing detection circuit [12] or non-mechanically scanned delay [14]. In this work, HTT processing for delay calibration is applied to a mechanically scanned Michelson interferometer to provide high resolution measurement of the individual gratings in the array. This customised demodulator is then applied to the single-parameter sensing of temperature.

1.3.5 High Speed Bragg Grating Sensor Array Demodulator for Structural Health Monitoring

Chapter 6 develops an all-fibre Michelson interferometer for high speed grating array demodulation for structural health monitoring. The all-fibre interferometric design uses the HTT for correction of spectral degradation due to non-uniform path length scanning and for calculation of the mean reflective wavelength of the individual gratings in the array.

Previously reported applications of the HTT for calibration of delay [6, 15] have been applied on bulk-optic mechanically scanned interferometers, with calibration based on the temporal phase of a highly stable reference laser. The use of an all-fibre design has several advantages over bulk optic interferometers, chief among which are portability and immunity to vibration.

FTS and the HTT are applied to interferograms obtained on the all-fibre, mechan-

ically scanned Michelson interferometer. The interferometer is referenced from both a narrow linewidth, temperature stabilised fibre Bragg grating and a highly stable (< 1 pm) reference laser for comparison. The ability of such a scheme to demodulate a fibre Bragg grating array is demonstrated and applied to the measurement of the thermally induced mean wavelength shift and strain induced mean wavelength shift in the light reflected from a single fibre Bragg grating in the array.

1.3.6 Conclusion

Finally, in Chapter 7, a brief summary is given of the work carried out in this thesis. Initially, a review of the experimental techniques is given, and then the achieved results are presented. Suggestions for future investigations are also discussed in light of the achieved results.

References

[1] X. C. Li, F. Prinz, and J. Seim, "Thermal behaviour of a metal embedded fiber Bragg grating sensor," *Smart Materials and Structures*, vol. 10, pp. 575–579, 2001.

[2] L. Zhang, Y. Liu, J. A. R. Williams, and I. Bennion, "Enhanced FBG strain sensing multiplexing using combination of intensity and wavelength dual-coding technique," *IEEE Photonics Technology Letters*, vol. 11, pp. 1638–1640, December 1999.

[3] G. Chen, L. Liu, H. Jia, J. Yu, L. Xu, and W. Wang, "Simultaneous pressure and temperature measurement using Hi-Bi fiber Bragg gratings," *Optics Communications*, vol. 228, pp. 99–105, 2003.

[4] I. Riant, "Fiber Bragg gratings for optical telecommunications," *Comptes Rendus Physique*, vol. 4, pp. 41–49, 2003.

[5] M. Davis and A. Kersey, "Application of a Fibre Fourier Transform Spectrometer to the Detection of Wavelength Encoded Signals from Bragg Grating Sensors," *Journal of Lightwave Technology*, vol. 13, no. 7, pp. 1289–1295, 1995.

[6] D. Flavin, R. McBride, and J. D. C. Jones, "Short-Scan Interferometric Interrogation and Multiplexing of Fibre Bragg Grating Sensors," *Optics Communications*, vol. 170, no. 4-6, pp. 347–353, 1999.

[7] K. B. Rochford and S. D. Dyer, "Demultiplexing of Interferometrically Interrogated Fiber Bragg Grating Sensors Using Hilbert Transform Processing," *Journal of Lightwave Technology*, vol. 17, no. 5, pp. 831–836, 1999.

[8] S. Huang, M. LeBlanc, M. M. Ohm, and R. M. Measures, "Bragg intragrating structural sensing," *Applied Optics*, vol. 34, no. 22, pp. 5003–5009, 1995.

[9] E. S. R. Sikora, D. J. McCartney, K. Farrow, and R. Davey, "Reduction in fibre reliability due to high optical power," *Electronics Letters*, vol. 39, pp. 1043–1044, July 2003.

[10] A. Martinez, M. D. I. Khrushchev, and I. Bennion, "Direct writing of fibre Bragg gratings by femtosecond laser," *Electronic Letters*, vol. 40, pp. 1170–1172, September 2004.

[11] D. Derickson, *Fibre Optic Test and Measurement.* Prentice Hall, 1998.

[12] S. D. Dyer, P. A. Williams, R. J. Espejo, J. D. Kofler, and S. M. Etzel, "Fundamental limits in fiber Bragg grating peak wavelength measurements," in *Proceedings of SPIE* (M. Voet, R. Willsch, W. Ecke, J. Jones, and B. Culshaw, eds.), vol. 5855, (Bellingham, WA.), pp. 88–93, SPIE, 2005.

[13] S. D. Dyer and K. B. Rochford, "Low coherence interferometric measurements of fibre Bragg grating dispersion," *Electronics Letters*, vol. 35, pp. 1485–1486, August 1999.

[14] D. F. Murphy, D. A. Flavin, R. McBride, and J. D. C. Jones, "Interferometric interrogation of in-fiber Bragg grating sensors without mechanical path length scanning," *Journal of Lightwave Technology*, vol. 19, pp. 1004–1009, July 2001.

[15] D. A. Flavin, R. McBride, and J. D. C. Jones, "Short Optical Path Scan Interferometric Interrogation of a Fibre Bragg Grating Embedded in a Composite," *Electronic Letters*, vol. 33, 1997.

Chapter 2

Review

Introduction

The aim of this chapter is twofold and, as such, is divided into two sections. The first section reviews the theory associated with the use of optical fibres as sensing elements, with particular emphasis on fibre Bragg gratings (FBGs). The second details the interrogation methods which are applied to the interrogation of FBGs in the work reported in later chapters.

Optical fibre sensors are a means of sensing whereby the lightwave guided within an optical fibre can be modified in response to an external influence [1]. The theory of the wave nature of light is presented in Section 2.1.1, with Sections 2.1.2 and 2.1.3 devoted to the description of the propagation of a lightwave through an optical fibre. Optical fibre materials and associated losses or attenuation as well as reliability issues are reviewed in subsequent Sections 2.1.4, 2.1.5 and 2.1.6 respectively.

Highly sensitive fibre optic sensors (FOS) have been demonstrated for the measurement of pressure, strain, electric and magnetic fields and vibration and temperature [2]. The high resolution of FOS is due to the fact that external perturbations can lead to changes in the phase, wavelength, modal content, polarization or intensity of the lightwave propagating in the fibre [1]. An overview of fibre optical sensors with particular emphasis on the mechanisms responsible for modulation of the lightwave in an optical fibre, namely the thermo-optic and thermo-elastic coeffiecients and the photoelastic effect, is presented in Section 2.1.8.

A particular feature of FOS arises from the very large information carrying capacity

of the optical fibre [3] and consequently, there is scope for incorporating very many sensors on a single optical fibre [4] or to use a single optical fibre as a distributed sensor, interrogating the sensor at different points along its length [5]. However, to date truly distributed sensing systems have not been utilised as they offer poor resolution, weak detectable signals and cumbersome interrogation schemes [7]. Quasi-distributed sensing systems, which are based on an array of FBGs multiplexed along the length of the fibre [6,8], have been preferred in many civil engineering applications requiring multiple point sensing distributed over a long range [7].

A FBG is a periodic modulation of the refractive index of the core of an optical fibre [9]. The basic operating principle of a FBG is that the grating reflects a narrow range of wavelengths of the light propagating along the fibre when the Bragg condition (or phase match condition) is satisfied [8–11]. Each FBG acts as a sensing element offering localised measurement. The measured quantity is encoded via the peak reflected wavelength, known as the Bragg wavelength (λ_B), of the individual gratings in the array. λ_B changes as the grating is subjected to mechanical strain, temperature, pressure, etc. This wavelength encoding is a unique characteristic of FBGs [12] that offers advantages over intensity based schemes. Section 2.1.10 introduces the theory of FBG manufacture, principles of operation and sensing principles.

Prior to introducing the theory of the interferometric interrogation schemes used for grating demodulation in Section 2.2, an overview of some of the more relevant interrogation schemes is presented in Section 2.1.16. Section 2.2 commences with an overview of the theory of coherence which is the basis for all the interferometric measurements reported in the following chapters. The concepts of coherence theory are then applied to interferometric measurement in Section 2.2.6. The mathematical analysis, i.e. the Fourier transform and the Hilbert transform, used to extract the information contained in the interferometric output of the later experimental chapters is described in Section 2.2.10.

2.1 Optical Fibre Sensing

2.1.1 Wave Nature of Light

A key element in the description of light is the interdependence of the electric, **E**, and magnetic, **B**, fields. The wave nature of light can be represented in the form of the classical electromagnetic field equations of Maxwell. The simplest statement of Maxwell's equations [3] applies to the behaviour of the electric and magnetic fields in free space,

$$\oint_C \mathbf{E} \cdot dl = -\iint_A \frac{\delta \mathbf{B}}{\delta t} \cdot dS \tag{2.1.1}$$

$$\oint_C \mathbf{B} \cdot dl = \mu_0 \epsilon_0 \iint_A \frac{\delta \mathbf{E}}{\delta t} \cdot dS \tag{2.1.2}$$

$$\oiint_A \mathbf{B} \cdot dS = 0 \tag{2.1.3}$$

$$\oiint_A \mathbf{E} \cdot dS = 0 \tag{2.1.4}$$

These equations, where $\epsilon = \epsilon_0$, $\mu = \mu_0$, can be manipulated to form vector expressions [3] for the case of non-conducting media, from which standard wave equations can be derived to yield the general wave phenomena of electromagnetic fields.

$$\nabla^2 \mathbf{E} - \epsilon\mu \frac{\delta^2 \mathbf{E}}{\delta t^2} = 0 \tag{2.1.5}$$

$$\nabla^2 \mathbf{H} - \epsilon\mu \frac{\delta^2 \mathbf{H}}{\delta t^2} = 0 \tag{2.1.6}$$

Equations (2.1.5-2.1.6) are known as the standard wave equations [13]. A complete derivation of these equations can be found in Appendix A.

Every component of the electromagnetic field obeys the scalar differential wave equation [3]

$$\frac{\delta^2 \psi}{\delta x^2} + \frac{\delta^2 \psi}{\delta y^2} + \frac{\delta^2 \psi}{\delta z^2} = \frac{1}{v^2} \frac{\delta^2 \psi}{\delta t^2} \tag{2.1.7}$$

provided that $v = 1/\sqrt{\epsilon_0 \mu_0}$.

The differential wave equation reveals a property of electromagnetic waves which is the basis of the work reviewed in Section 2.2 and in the work reported in the following chapters. If two wavefunctions ψ_1 and ψ_2 are each separate solutions of the wave equation it follows from the Principle of Superposition that $(\psi_1 + \psi_2)$ is also a solution.

The resultant from the superposition of two waves depends on the phase angle between them. If the two waves are in phase they reinforce each other, whereas if they are 180° out of phase they diminish each other. This phenomenon is given the name interference [3] and is discussed in further detail in Section 2.2.1.

2.1.2 Fibre Structures and Modes

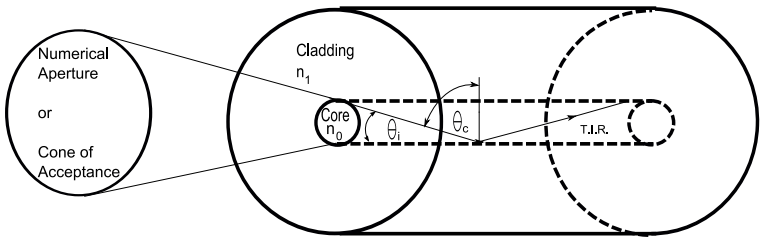

Figure 2.1: Typical optical fibre

An approximate model for the propagation of lightwaves in a fibre can be based on classical geometrical ray optics. The generic optical fibre design, with a core of high refractive index (n_0) surrounded by a cladding of lower refractive index (n_1) is shown in Figure 2.1. The treatment here will deal only with step index fibres, the solutions for graded index fibres can also be found in the cited literature. The index difference allows light, which is launched into the fibre at an angle less than $90° - \theta_c$, where θ_c is the critical angle, to be guided along the fibre by total internal reflection (T.I.R.). The critical angle, θ_c is defined as

$$\theta_c = \ sin^{-1}\left(\frac{n_1}{n_0}\right) \tag{2.1.8}$$

where n_1 is the refractive index of the cladding and n_0 is the refractive index of the core. There are only a finite number of paths which satisfy this condition and for every value

of the incident angle $\theta_i < 90° - \theta_c$ a distinct mode, or electromagnetic field distribution, can propagate along the fibre [14].

The ray model appears to allow rays at an incident angle less than $90° - \theta_c$ to propagate along the fibre. However, when the phase of the plane wave associated with the ray is taken into account, there are only rays at discrete angles less than or equal to θ_c capable of propagating along the fibre [13]. The phase of the wave changes not only as the wave propagates, but also on reflection. In order for the wave associated with a given ray to propagate, the phase of the twice reflected wave must be the same as that of the incident wave to interfere constructively, otherwise the waves will interfere destructively and cancel each other out [13, 14]. A more detailed understanding of wave propagation in an optical fibre requires solutions to Maxwell's equations subject to the boundary conditions of the fibre [15], with features of the solutions summarised below.

2.1.3 Electromagnetic Fields within Optical Waveguides

In addition to supporting a finite number of guided modes the optical fibre waveguide has an infinite continuum of radiation modes that are not guided in the core but are solutions of the same boundary problem [13]. Cladding modes result from the power that is outside the cone of acceptance or numerical aperture ($NA = \sqrt{n_0^2 - n_1^2}$) of the fibre being refracted out of the core. The finite radius of the cladding results in some of this radiation getting trapped in the cladding and propagating along the fibre [13,16]. A third category of modes, known as 'leaky modes', is also present in fibres [13,17]. 'Leaky modes' are only partially confined to the core and attenuate by radiating their power out of the core as they propagate along the fibre. The solutions to Maxwell's equations for modes at the core-cladding interface are non-trivial and will not be treated here.

A mode can remain guided along the optical fibre as long as the propagation constant, β (as defined in Equation 2.1.15), satisfies [13, 16, 17]

$$n_2 k \leq \beta \leq n_1 k \tag{2.1.9}$$

where n_1 and n_2 are the refractive indices of the core and the cladding respectively and $k = 2\pi/\lambda$. This is a consequence of the boundary conditions imposed on the solutions to the wave equation. Since discontinuities exist in the refractive index profile of the fibre (especially in step index fibres), the infinite possibilities provided by the wave equation are restricted by the waveguides physical structure. At the core-cladding interface, the tangential components of the electric and magnetic fields must match their counterparts on either side of the boundary, and in addition the electric and magnetic field vectors must tend to zero at infinity [13].

Expressed in cylindrical coordinates for the geometry of an optical fibre [13, 16–18], the wave equation becomes

$$\left[\frac{\delta^2}{\delta r^2} + \frac{1}{r}\frac{\delta}{\delta r} + \frac{1}{r^2}\frac{\delta^2}{\delta \phi^2} + \left[k^2 - \beta^2\right]\right]\begin{bmatrix} E_z \\ H_z \end{bmatrix} = 0 \tag{2.1.10}$$

Solutions by separation of variables [13, 16, 17] take the form

$$\begin{bmatrix} E_z \\ H_z \end{bmatrix} = \psi(r)e^{(\pm i l \phi)} \tag{2.1.11}$$

so that the wave equation becomes

$$\frac{\delta^2\psi}{\delta r^2} + \frac{1}{r}\frac{\delta\psi}{\delta r} + \left[k^2 - \beta^2 - \frac{l^2}{r^2}\right]\psi = 0 \tag{2.1.12}$$

which is the Bessel differential equation. The solutions inside the core are ordinary Bessel functions of order l (Figure 2.3). The solutions yield the modes propagating within the fibre which can be divided into two types: skew and meridional modes [13, 16, 17]. Skew rays are those rays which do not propagate through the central axis of the fibre (c.f Figure 2.2). The Bessel functions within the core are similar to harmonic functions as they exhibit oscillatory behavior for real k. Therefore, there will be m roots for any given l. The meridional modes are designated transverse electric, TE ($E_z = 0$), or transverse magnetic, TM ($H_z = 0$), and require two indices, l and m (corresponding

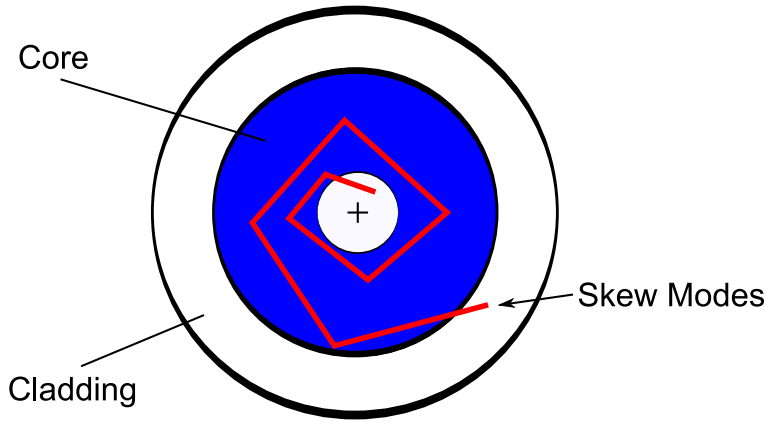

Figure 2.2: Representation of Skew modes propagating around the central axis of the fibre.

to the roots of the Bessel function), to completely specify the mode. Skew modes have components of both E and H and are designated as either $HE_{l,m}$ or $EH_{l,m}$.

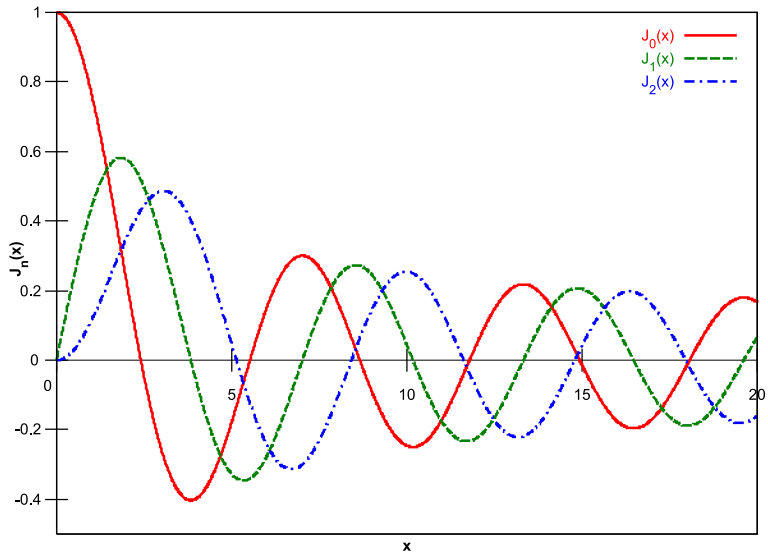

Figure 2.3: Plot of Bessel function of the first kind, J_l (x), for integer orders $l = 0, 1, 2$.

The exact expressions for the skew modes are very complicated. However, the propagation of modes along the fibre can be greatly simplified provided that the refractive indices of the core and the cladding differ by only a few percent [19, 20], i.e.

$$\Delta = \frac{n_1 - n_2}{n_1} << 1 \tag{2.1.13}$$

The full set of modes can then be approximated by a set of linearly polarized modes;

this approach is known as the weakly guiding approximation. The weakly guided modes or linearly polarized modes are designated $LP_{l,m}$ and behave like a single mode with two degrees of polarization [13, 16, 17]. The LP modes are only approximate solutions to the field equations but are sufficient for practical fibres.

Generally the properties of an optical fibre can be expressed in the form of normalised variables which allow determination of these properties from universal curves [18]. One example is the cut-off condition for fibre modes. Equation 2.1.9 stated the cut-off condition for modes in the core, $n_2 k \leq \beta \leq n_1 k$, a result of the boundary conditions imposed on the Bessel functions and the fact that the solution inside the core must be real [13]. The weakly guiding approximation implies that $n_2 k \simeq \beta \simeq n_1 k$, so that the condition for a single electromagnetic mode to propagate is that the normalised frequency, V, be < 2.405, where

$$V = \frac{2\pi a}{\lambda}\sqrt{n_1^2 + n_2^2} \tag{2.1.14}$$

where a is the core radius, λ is the free space wavelength and n_1 and n_2 are the refractive indices of the core and the cladding respectively. Therefore, from Equation 2.1.14, reducing the dimensions of the fibre can limit the number of modes propagating in the fibre. The value of 2.405 is the first zero of the lowest order Bessel function. Single mode fibres typically have core diameters between 8 and 10 μm for operation at 1550 nm.

2.1.4 Optical Fibre Materials

The basic challenges in manufacturing optical fibres are to achieve precise control of fibre dimensions and refractive index. The materials from which optical fibres are composed must also satisfy a number of criteria. The fibre material must be highly transparent to the radiation being used; it must also be possible to fabricate the basic core and cladding structures; and it must be reasonably flexible [21]. Two materials which satisfy these conditions are silica (SiO_2) and various types of plastic [13].

In silica optical fibres, the refractive index variation between the core and the cladding is obtained by doping the silica with another material [16, 21]. For example, doping with Germanium (Ge), Titanium (Ti) and Aluminium (Al) raise the refractive index, whereas Boron (B) and Fluorine (F) lower the refractive index [21]. High performance fibres have been fabricated using Ge-doped cores and F-doped cladding. Fibre manufacturing techniques are generally based on a type of vapour deposition [13, 21]. The most popular methods of manufacture are by modified chemical vapour deposition, outside vapour deposition and vapour axial deposition [13]. The refractive index change induced by doping is typically only a few percent, as the solubility of these materials in silica is limited [14], meaning that silica fibres have small numerical apertures (0.2 or less).

Fibres which have a silica core and a plastic cladding have also been manufactured, called plastic coated silica fibres (PCS) [13]. The fibre preform in this case is made from the core material only and passed through a plastic bath in the drawing process to provide the cladding. However, these fibres are only suitable for medium distance, moderate bandwidth systems as the losses are ~10 dB km^{-1} compared to ~0.15 dB km^{-1} for fused silica at 1550 nm. The loss values are significantly higher than all-silica fibres because the energy which travels in the cladding is subject to much higher attenuation [14].

All-plastic fibres have a core and cladding made from different types of plastic. A popular choice for the core of a plastic fibre is polymethyl methacrylate (PMMA, n=1.495) and a cladding of flouralkyl methacrylate (n=1.402). The main problem with plastic fibres is that they exhibit much higher attenuations than silica due to strong absorption bands associated with the molecular bonds and high Rayleigh scattering from the long chain molecules [13, 22] but the basic causes are the same, as described below.

2.1.5 Optical Fibre Losses

The 1550 nm window has become the transmission window of choice for fibre optic telecommunications, resulting from two important parameters in electromagnetic

propagation along the length of a fibre, namely attenuation and bandwidth. There are three main attenuation mechanisms in an optical fibre: absorption, scattering, (Figure 2.4) and radiative loss [14].

- Absorption losses occur mainly due to impurity (primarily OH^-) absorption and long wavelength vibrational absorption.
- Radiative losses are generally kept small by using a sufficiently thick cladding, a buffer to protect the fibre and prevention of sharp bends along the fibre.
- The fundamental scattering mechanism is Rayleigh scattering from the irregular glass structure, with each irregularity acting as a point scattering centre.

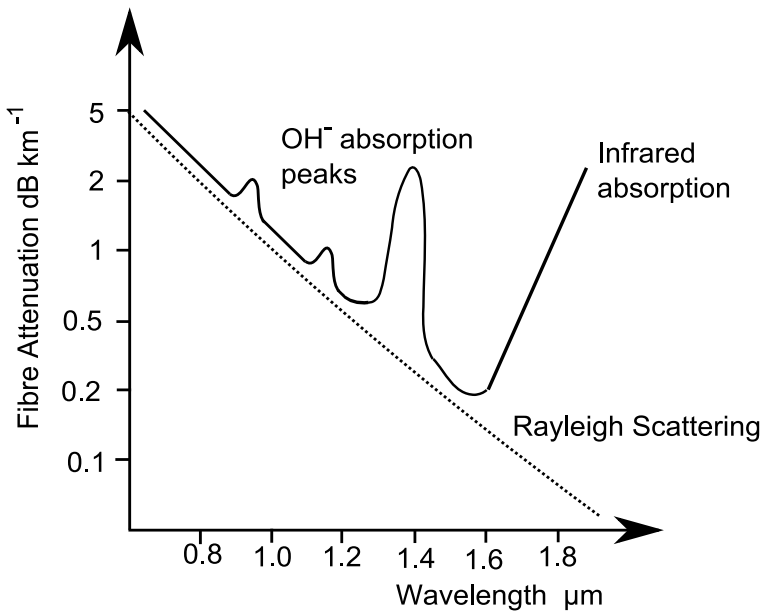

Figure 2.4: Silica fibre losses due to absorption and scattering. The loss of the fibre at 1.55 μ m (0.2 $dBkm^{-1}$) is very close to the fundamental limit imposed by Rayleigh scattering. [Figure obtained from [14]]

The window around 1550 nm shown in Figure 2.4 exhibits the lowest attenuation characteristics (0.2 dB km^{-1}). The mass production of 1550 nm single mode fibres and components for the telecommunications market has resulted in a cheaper supply of components for the optical sensing market, which would not otherwise have been readily available.

In the design of optical fibre systems, there are parameters other than fibre attenuation which have to be considered. Interference between different polarisation states is discussed in section 2.2.5 and can lead to signal fading [13]. Also the optical signal becomes distorted as it travels along the fibre. This distortion is a consequence of dispersion in the optical fibre and determines the limit of the information carrying capacity of the fibre [13]. The propagation of a mode along a fibre can be described by the propagation constant

$$\beta = \frac{2\pi n_{eff}}{\lambda} = \frac{n_{eff}\omega}{c} \tag{2.1.15}$$

where n_{eff} is the effective modal index, λ is the wavelength of the light, ω is the optical angular frequency and c is the speed of light in a vacuum. A monochromatic light wave travels along the fibre with constant phase velocity $v_p = \omega/\beta$. However, truly monochromatic light sources do not exist, instead containing a spread of frequencies each of which propagate at different phase velocities along the fibre.

Dispersion

The maximum modulation bandwidth or pulse rate of a fibre is limited by the phenomenon of dispersion. There are two principal forms of dispersion: intermodal and intramodal. Intermodal dispersion only occurs in multi-mode fibres and is not considered here. Intramodal dispersion occurs within a single mode as a result of the finite spectral width of the source and the dependence of group velocity on wavelength.

The information-carrying capacity of a fibre is at a maximum when the group delay, τ_g (the time required for a modulated signal to travel along the length of the fibre), does not vary with wavelength [23]. Dispersion manifests itself as a temporal effect on the group velocity, v_g, of the wave travelling through the medium, where

$$v_g = c\left[n - \lambda\frac{dn}{d\lambda}\right]^{-1} \tag{2.1.16}$$

and λ is the wavelength of light and c is the speed of light in a vacuum. The group velocity dispersion results in a pulse of light spreading in time because of the differ-

ent frequency components of the pulse traveling at different velocities through the medium. The group delay, therefore, is $\tau_g = L/\upsilon_g$ where L is the length of the fibre. The dispersion, D, can be designated as [13, 23]

$$D = \frac{1}{L}\frac{d\tau_g}{d\lambda} \tag{2.1.17}$$

and defines the pulse spread as a function of wavelength. It is a result of material and waveguide dispersion [13].

Material Dispersion: Material dispersion is produced by the same processes that produce fibre attenuation, namely the wavelength dependence of the waveguide material's refractive index. It is particularly important if the source has a broad spectral width. The group delay due to material dispersion, τ_{mat}, is given by [13]

$$\tau_{mat} = -\frac{L}{c}\left(n - \lambda\frac{dn}{d\lambda}\right) \tag{2.1.18}$$

Waveguide Dispersion: Waveguide dispersion occurs because of the dependence of phase and group velocity on the core radius and wavelength. For circular waveguides this dependence can be expressed as a function of the ratio a/λ [13], and is only of importance in singlemode fibres. The effect of waveguide dispersion can be approximated by assuming that the refractive index of the material is independent of wavelength. Therefore the group delay, τ_{wg}, arising from waveguide dispersion is given by [13]

$$\tau_{wg} = \frac{L}{c}\frac{d\beta}{dk} \tag{2.1.19}$$

where k (= $2\pi/\lambda$) is the free space propagation constant and β (= nk) is the z component of the propagation vector.

The total dispersion, D, in single mode fibres consists primarily of material and waveguide dispersion and is represented by Equation 2.1.17. The total broadening, σ,

of an optical pulse with a wavelength spread σ_λ is given by

$$\sigma = D(\lambda) L \sigma_\lambda \tag{2.1.20}$$

The measurement of dispersion requires examination of the pulse delay over a wide wavelength range. Such examination involves curve fitting to the Sellmeier equation as outlined below.

Sellmeier Equation: The refractive index, n, is generally a function of the frequency, or wavelength, of the light, $n = n(f)$ or $n = n(\lambda)$. The dependence of the refractive index on frequency or wavelength can be quantified empirically by the Sellmeier equation [16], as

$$n^2(\lambda) = 1 + \sum_1^i \frac{A_i \lambda^2}{\lambda^2 - \lambda_i^2} \tag{2.1.21}$$

where generally $i = 3$, and A_i and λ_i are the Sellmeier coefficients. Curve fitting using the Sellmeier equation improves dispersion measurement precision as direct differentiation of the measured group delay data tends to amplify the effect of noise [23].

Polarization and Birefringence

Most optical materials exhibit some degree of refractive index asymmetry that allows light in two orthogonal polarisation states to travel at different speeds through the material. This property is called birefringence. The polarisation states into which polarised incident light is resolved are defined by the internal structure of the material. For well-defined structures such as quartz crystal, these states are maintained through the device and are called eigenmodes. Most of the concerns in fibre optics involve imperfections which break the circular symmetry of the fibre core. In a perfectly symmetric fibre the $LP_{l,m}$ modes described in Section 2.1.3 are two independent, degenerate propagation modes with equal propagation constants. Deviations of the fibre core from circular symmetry breaks the degeneracy of the the two $LP_{l,m}$ modes, [13], and the modes propagate with different velocities.

In 1816 Sir David Brewster discovered that normally transparent isotropic materials could be made optically anistropic by the application of mechanical stress [3]. This phenomenon is known as mechanical birefringence, photoelasticity or stress birefringence. Under compression, or tension, the material takes on the properties of a negative or positive uniaxial crystal, respectively. The effective optic axis is in the direction of the stress, and the induced birefringence is proportional to the stress. If the stress is not uniform over the sample, neither is the birefringence or retardance imposed on the transmitted wave [3]. Retardance is a measure of the differential phase shift of light in the eigenmodes, more commonly referred to as the fast and slow waves. Retardance is typically expressed as a phase shift at a specified wavelength [23] as

$$\Delta\phi = \frac{2\pi}{\lambda_0} d(|n_o - n_e|) \tag{2.1.22}$$

where $\Delta\phi$ is the phase difference between the o- (ordinary) and e- (extraordinary) waves, λ_0 is the wavelength in a vacuum and $d(|n_o - n_e|)$ is the relative optical path difference between the axes. In fibre interferometry, where the method of optical path difference scanning is fibre stretching, the two polarisation states can interfere provided the source spectrum is narrow enough that the source coherence time is much larger than the difference in propagation time between the fast and slow axes of the fibre. This can lead to polarisation-induced fading (c.f. section 2.2.5) necessitating the use of Faraday rotation mirrors [24].

2.1.6 Optical Fibre Reliability

The tensile strength of silica fibres is very high when manufactured and compares favorably with that of steel [14]. Optical fibres are expected to retain most of their physical properties for $10-20$ years [25]. However, the reliability and expected lifetime for an optical fibre is closely related to handling and the environment in which it operates. The decrease in strength caused by these effects can be greatly reduced by adding a coating layer to the fibre. The properties of the protective coating contribute largely

to the mechanical properties of the fibre, which can be strongly influenced by cracks on the surface. Polymer coatings are applied to prevent a variety of types of damage occurring, e.g. the formation of surface defects through scratching and abrasion, minimisation of the influence of existing defects, and they can also act as a diffusion barrier to prevent any damage by agents reaching the surface.

Damage to optical fibres has been observed by Severin *et al* [25] when used in harsh environments such as acid environments where a reduction in breaking stress was observed in aged fibres. The reduction in failure time depended on the protective coating used, polyacrylate vs hermetic carbon, with the hermetic carbon coating providing greater protection in the acidic environment. Some other types of damage to fibres that have been reported are:

1. The fibre fuse phenomenon, which is initiated by local heating of the fibre. This causes a series of voids which propagate back along the fibre towards the light source, resulting in catastrophic damage to the fibre core [26];

2. End face damage under high powers due to contaminants which can also initiate the fibre fuse phenomenon [27];

3. Damage to the coating in tight bend situations where catastrophic damage to the fibre can occur [28, 29].

Damage occurs when the transmission path of light in the fibre is modified. Therefore, the reliability of optical components where the internal structure of the fibre has been modified, as happens with FBG inscription, also needs to be addressed. This is the focus of the work reported in chapter 3 in this thesis.

2.1.7 Fibre Optic Couplers

Fibre optic couplers are the equivalent of bulk optic beam-splitters. They are the most widely used optical components in telecommunications and sensing and are used frequently throughout the experimental work reported in this thesis. Directional

couplers are used for optical power splitting, wavelength division multiplexing / demultiplexing and polarisation splitting [30].

The principle of evanescent field coupling is used in single mode couplers. It is based on the fact that the modal field of the guided mode extends beyond the core cladding interface. When two fibre cores are brought sufficiently close to each other the fields overlap and become coupled between the fibres. For two identical single mode fibres the power launched into one fibre, $P_1(0)$, couples power between the two fibres according to

$$P_1(z) = P_1(0)cos^2 kz \tag{2.1.23}$$

$$P_2(z) = P_1(0)sin^2 kz \tag{2.1.24}$$

where P_2 is the power coupled into the second fibre, k is the coupling coefficient and z is the coupling length [30]. Fibre couplers are in general wavelength-sensitive as the propagation constants of the modes and the coupling coefficient, k, depend on wavelength as a consequence of fibre mode dispersion. A directional coupler can act as a wavelength multiplexer / demultiplexer if the coupling coefficients for the wavelengths to be multiplexed, k_1 for λ_1 and k_2 for λ_2, meet the condition $k_1.z = m\pi$ and $k_2.z = (m - 1/2)\pi$. From Equations 2.1.23 and 2.1.24 the power due to the individual wavelengths can then be filtered into individual fibres exiting the coupler.

2.1.8 Fibre Optic Sensing

Fibre optic sensors operate on the principle that environmental changes modulate the light signal propagating along the length of a fibre. A lightwave can be characterised by amplitude, polarisation, frequency and phase, all parameters which may be modulated. Fibre sensors can be categorised according to the parameter being modulated i.e. intensity [31], polarimetric [32], spectral [33] and interferometric sensors [32]. They can also be classified by the sensor configuration, which may be intrinsic or ex-

trinsic. Intrinsic sensors use the fibre itself as the sensing element whereas extrinsic sensors use an external transducer, which can be located inside or outside the fibre, to modulate the light signal [1].

As as example, an intensity based sensor is based on the modulation of the intensity of the transmitted light. In a simple extrinsic configuration for the measurement of strain, two optical fibres can be separated by a small gap which widens as strain is applied parallel to the fibres [34]. This results in a reduction in the transmitted intensity between the two fibres. However, intensity based sensors are sensitive to variations in the source intensity and to fluctuations in intensity caused by bend losses and coupling losses. Sensors which are based on phase / wavelength modulation, as described in Section 2.1.9, are more robust and suitable for use outside laboratory conditions.

The modulation of an electric field, $E(\lambda)$, propagating along an optical fibre, in response to a measurand field can be defined [32,35] as

$$E'(\lambda) = T(X,\lambda)E(\lambda) \tag{2.1.25}$$

where

(i) $E'(\lambda)$ is the electric field after modulation

(ii) $T(X,\lambda)$ is a propagation matrix which describes the sensing element

(iii) X is a vector which describes the physical environment.

T is a product of terms describing a physically observable effect on the transmitted beam, such that

$$T = ae^{i\phi}B \tag{2.1.26}$$

where a is the scalar transmittance, ϕ is the mean phase retardance and B is the birefringence matrix [35]. These parameters are both dispersive and environmentally sensitive [32].

The transmittance of the fibre shows only weak environmental sensitivity and intrinsic monomode sensors are generally based on phase and polarisation modulation,

recovered using interferometry and polarimetry respectively [35]. The phase retardance, ϕ, can be a measure of the retardance introduced between interfering beams, as occurs in a two beam interferometer (c.f. section 2.2.6), or a measure of the relative phase retardance between the linear or circular polarisation eigenmodes of the fibre. The environmental sensitivity of the fibre can be expressed in terms of the dependence of the phase on external stimuli such as temperature, T, pressure, P, and strain, δl, [32,35] such that

$$\frac{\delta\phi}{\delta X} = \frac{2\pi}{\lambda}\left[n\frac{\delta l}{\delta X} + l\frac{\delta n}{\delta X}\right]; \qquad X = T, P, \delta l.... \tag{2.1.27}$$

where l is the length of the fibre and n is the fibre refractive index. The first term inside the brackets corresponds to the physical extension of the fibre and the second term to changes in the refractive index, which can be due to one or a combination of T, P, δl.

2.1.9 Modulating Effects in Fibre Sensors

The Photoelastic Effect

The photoelastic effect describes the relation between mechanical strain and the resulting refractive index change in the material. The longitudinal and transverse strains, ϵ_l and ϵ_t, on a fibre are related to the applied stress [36] as follows:

$$\epsilon_l = \epsilon_0 + \delta\epsilon_0^2 \tag{2.1.28}$$

$$\epsilon_t = -\nu\epsilon_0 + \beta\epsilon_0^2 \tag{2.1.29}$$

where ϵ_0 is the applied stress divided by Young's modulus (Y), ν is the Poisson ratio and δ and β are two non-linearity constants. The stress is the applied force per unit area giving $\epsilon_o = F/(2\pi r^2 Y)$ where F is the applied tensile force and r is the initial radius of the fibre.

For an isotropic material, the photoelastic effect can be characterised by two strain optic coefficients. Light which propagates through a single mode fibre in a strained

state is polarised in the transverse direction [36] and sees a change in the refractive index, Δn, which is defined as

$$\Delta n = -\left(\frac{n^3}{2}\right)[S_1(P_{11}+P_{12})+S_3P_{12}] \tag{2.1.30}$$

where

(i) S_1 and S_3 are the first and third elements of the strain tensor [36]

$$S_1 = \epsilon_t + \nu^2\frac{\epsilon_0}{2} \tag{2.1.31}$$

$$S_3 = \epsilon_l + \frac{\epsilon_0}{2} \tag{2.1.32}$$

(ii) P_{11} and P_{12} are the individual strain-optic coefficients

Typical values for silica are $P_{11} = 0.113$ and $P_{12} = 0.252$ [37].

The change in refractive index has contributions from both the longitudinal and transverse strain. Neglecting the contribution due to changes in the fibre diameter (small), the phase change, $\Delta\phi$, experienced by light propagating through the fibre [36] can be expressed as

$$\Delta\phi = \frac{2\pi}{\lambda}L(n\epsilon_l + \Delta n) \tag{2.1.33}$$

where λ is the wavelength of the light, and L is the length of the fibre. The optical phase change can therefore be expressed as a function of the physical elongation of the fibre and the change in refractive index.

Thermo-optic and Thermal Expansion Coefficient

Changes in the temperature of the glass in a fibre also induce changes in both the size of the fibre and in the refractive index of the fibre. The change in refractive index induced by a temperature change is the thermo-optic coefficient [38] given by

$$\xi = \frac{1}{n}\frac{\delta n}{\delta T} \tag{2.1.34}$$

and has a typical value of $6.86x10^{-6}\ {}^{o}C^{-1}$ for Ge doped silica [38].

The change in dimension is the thermal expansion coefficient [38] given by

$$\alpha = \frac{1}{L}\frac{\delta L}{\delta T} \tag{2.1.35}$$

and has a typical value of $0.55x10^{-6o}C^{-1}$ for silica [38].

A key problem for fibre-optic sensors is that it is not possible to determine whether the fibre is uniquely sensing changes in temperature or strain, because of the interdependence of the length, L, of the fibre and the refractive index, n, on both strain and temperature (Equation 2.1.27). Discriminating between the two usually involves isolation of a sensor or part of a sensor [39] from one of the measurands to act as a reference, as described in the case of fibre Bragg grating sensors in Section 2.1.10.

Phase Measurement

Optical interferometry, which will be reviewed and discussed in Section 2.2.6, provides an accurate method for measuring path length changes in optical fibres. The phase of the light leaving a fibre can be changed by dimensional and / or refractive index changes in the fibre. Therefore, if one fibre is subjected to a different strain or temperature than the other, this difference appears as a displacement of the interference fringes, and can be measured from this displacement. The basic quantity to be calculated is the optical phase change per unit fibre length per unit of the physical stimulus being measured, i.e $\Delta\phi/SL$ where $\Delta\phi$ is the phase change in radians, L is the fibre length and S is the stimulus.

A change in temperature of the fibre, ΔT, changes the optical phase of the light propagating through it, $\Delta\phi$, due to two effects: the change in fibre length due to thermal expansion or contraction and the temperature induced change in refractive index [40] given by

$$\frac{\Delta\phi}{\Delta T} = \frac{2\pi}{\lambda}\left(n\frac{dL}{dT} + l\frac{dn}{dT}\right) \tag{2.1.27}$$

where the effects of the fibre diameter changes are negligible. The fringe displacement

obtained from this formula is given in radians / °C m.

Two of the most successful applications of FOS using phase measurement have been the fibre gyroscope and the fibre hydrophone. A brief description of the operation of these sensors follows.

Fibre Optic Gyroscope

The fibre optic gyroscope (FOG) is a Sagnac interferometer (illustrated in Figure 2.5) which measures the Sagnac phase shift induced on rotation [41]. The lightwave entering the interferometer is divided to follow two counter-propagating waves, one in the clockwise direction and one counterclockwise. The beams are then recombined at the interferometer output to interfere. The interference pattern is detected at the photodiode D. When the interferometer is rotated, the path taken by one beam is shortened in comparison to that of the other. The result is a phase shift, known as the Sagnac phase shift ϕ_s, which is proportional to the angle of rotation. ϕ_s depends on the angular rotation Ω, the number of loops of the fibre coil N and the area A enclosed by each loop according to [3, 41, 42]

$$\phi_s = \frac{8\pi N A \Omega}{\lambda c} \tag{2.1.36}$$

Low cost FOG systems have found applications in air navigation systems, land and marine navigation systems [43, 44]. Most gyroscope resolution requirements are of the order of 100 °/s, but fibre gyros have achieved rates of 5000 °/s [45]. Some of the advantages of interferometric FOGs over traditional spinning mass gyros are: short warm up time, long life, high reliability, wide dynamic range and low cost [46].

Fibre Optic Hydrophone

The fibre optic hydrophone has been implemented successfully for measurement of underwater acoustic pressure measurements [47, 48] in particular for military applications. Optical fibre sensors do not radiate electromagnetic waves, the absence of which is particularly advantageous for stealth operation. Other advantages offered by

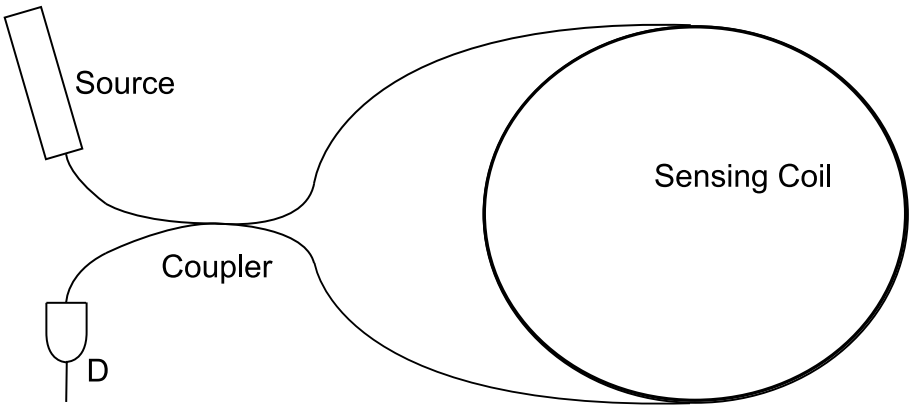

Figure 2.5: The basic scheme for a fibre-optic gyroscope.

the fibre-optic hydrophone over conventional hydrophone techniques are flexibility of design and multiplexing. As a result the fibre-optic hydrophone was primarily developed by the U.S. navy [48]. In an interferometric implementation of the hydrophone, one arm of the interferometer acts as the acoustic sensor. An acoustic signal acting on the sensing arm induces a phase change in the light traveling through the fibre. The phase change arises from two main sources; the change in length due to the applied strain, and the change in refractive index (the stress-optic effect). The change in phase, $\Delta\phi$, in a fibre of length L [48] is given by

$$\Delta\phi = k\,n\,L\,s - \frac{1}{2}n^3 k\,L\,(s_1 P_{11} + s_2 P_{12} + s_3 P_{21}) \tag{2.1.37}$$

where k is the wavenumber of the acoustic signal, n is the refractive index, s_x are the strain components and P_{xy} are the Pockel's coefficients of the stress-optic tensor which relate the strain to the refractive index change.

In general, one of the disadvantages of interferometric sensing for strain and temperature measurement is that the change measured is only with respect to the phase of the reference arm, requiring thermal and strain isolation of the reference arm. Any change in the environmental conditions to which the reference arm is exposed will manifest itself in the interferometric measurement. A FBG, however, is an optical component in which the measurand is directly encoded in the wavelength reflected from

the grating and is an absolute parameter, making it ideal for use as an embedded sensor. The theory, manufacture and operation of FBGs are reviewed in the following sections.

2.1.10 Fibre Bragg Gratings

FBG Basic Definitions and Properties

A fibre Bragg grating is a periodic modulation of the optical characteristics of an optical fibre, obtained by inducing a deformation in the fibre material or by modifying the refractive index of the core [49–51]. The latter is the standard method for grating inscription, where the grating is formed in photosensitive single mode fibre by illumination of the core with ultraviolet (UV) light. Fibre Bragg gratings are ideally suited to wavelength division multiplexed configurations as they offer substantial flexibility in their design [11, 15].

Properties that can be varied are the amplitude of the induced change in core refractive index and the length and period of the grating. Tailoring of these physical properties has a corresponding effect on the resonant wavelengths, grating intensity and bandwidth. FBGs have a number of distinguishing advantages over other implementations of fibre optic sensors. In particular the measurand is encoded in the reflected wavelength of the sensing element, unique wavelength multiplexing capacity [52] and also potentially low cost fabrication techniques when inscribed on the fibre drawing tower [53].

A more detailed description of fabrication methods may be found in Section 2.1.13.

Overview of General Applications

The engineering field of Smart Materials and Structures, sometimes called Active Materials and Adaptive Structures, has seen the development of structurally integrated fibre optic sensing systems to replace traditional electrical sensors [7]. Fibre Bragg gratings have become the most promising candidate for deployment in smart struc-

tures [54–58]. They offer localised measurement and large measurement range, high electromagnetic immunity, measurement of a wide range of measurands and potentially low cost fabrication techniques. Their small dimensions make them ideal for use as embedded sensors in composite materials. The measurand is encoded in the reflected wavelength and is an absolute parameter. They also offer high wavelength division multiplexing capacity as multiple sensors can be written along the length of a fibre, with each one reflecting at a different wavelength without overlap.

Bragg grating sensors have been demonstrated for use in sensing systems for many applications, eg, mining [54], wind turbine monitoring [55], FBG sensor based seismic geophones for oil and gas exploration [59], bridge health monitoring [56] [57] and tunnel monitoring [58]. Structural health monitoring requires that sensor measurement of temperature and strain be insensitive to each other [12]. Fibre Bragg gratings are sensitive to both. On a single measurement of the Bragg wavelength shift it is impossible to differentiate between the changes in strain and temperature. The above applications have all included some form of temperature compensation mechanism, such as a strain isolated grating in the sensing configuration to measure temperature [55] or the use of thermocouples to measure the temperature at the sensing site [56].

Numerous other schemes for discriminating between these effects have been demonstrated. Xie *et al.* [60] demonstrated a scheme where a single grating is used with one part of the grating fixed to a steel plate resulting in two reflection spectra, one of which is isolated from strain. However, limitations on the scheme, due to softening of the epoxy used to fix the grating to the steel plate, required all measurements to be taken under 40^oC. Xu *et al.* [61] demonstrated the simultaneous measurement of strain and temperature using superimposed Bragg gratings reflecting at separate wavelengths. James *et al.* [62] demonstrated a scheme based on two Bragg gratings inscribed in fibres with different diameters and spliced together where the strains experienced by the fibres are dependent on the cross-sectional area but the effects are common-mode. Xu *et al.* [63] removed the temperature dependence of a chirped FBG in tapered fibre by applying a strain gradient across the grating length. The bandwidth of the grating is

made strain-dependent when a strain gradient is introduced along the grating length.

The following section will develop the theory behind the principles of operation of FBGs as sensors, while Section 2.1.12 describes their temperature and strain sensitivities.

2.1.11 Operational Principles

The formation of gratings was first reported in 1978 by Hill *et al* [49] at the Canadian Communications Research Centre. It was reported that intense Argon ion laser radiation was launched into germanium-doped fibre. After several minutes an increase in reflected light intensity was observed, which grew until almost all of the light being launched into the fibre was being reflected. Spectral measurements confirmed that a very narrow band Bragg grating filter had been formed over the entire 1 m length of the fibre. The refractive index grating produced was due to a standing wave intensity pattern formed by the forward propagating light and the back reflected component from the end facet of the fibre. This achievement, subsequently called Hill gratings [11], established the previously unknown photosensitivity of germania fibre.

Fibre Bragg Grating Theory

In general the resulting perturbation to the effective refractive index, $\delta n_{eff}(z)$ takes the form of an amplitude and phase modulated waveform [11] as follows:

$$\delta n_{eff}(z) = \overline{\delta n}_{eff}(z)\left(1 + v\ \ cos\left[\frac{2\pi z}{\Lambda} + \phi(z)\right]\right) \tag{2.1.38}$$

where n_{eff} is the modal index, which varies along the grating length because of the variation in the average refractive index and the envelope of the grating modulation, Λ is the period of the refractive index modulation and v is the contrast of the modulation which is determined by the visibility of the UV fringe pattern.

The result of the refractive index modulation is a uniform fibre phase grating (Bragg grating) which acts as an optical diffraction grating and can be described by the grating

equation [64] as

$$n_{co}\ \ sin(\theta_2) = n_{co}\ \ sin(\theta_1) + m\frac{\lambda}{\Lambda} \tag{2.1.39}$$

where θ_1 is the incident angle of the light on the grating, θ_2 is the angle of the diffracted wave, n_{co} is the refractive index of the core and m determines the diffracted order. Generally $m = -1$ for first order diffraction which dominates in a fibre grating [65]. The reflected mode propagates in the opposite direction, yielding $n\ \ sin(\theta_2) < 0$ and recognising that $n_{eff} = n_{co} sin(\theta)$, the resonant wavelength for the reflection of a mode of index n_{eff_1} into a mode of index n_{eff_2} [11,65] is

$$\lambda = (n_{eff_1} + n_{eff_2})\Lambda \tag{2.1.40}$$

For a Bragg grating in single mode fibre the two modes are identical [11,65] yielding

$$\lambda = 2n_{eff}\Lambda \tag{2.1.41}$$

FBG Coupled Mode Theory

The grating characteristics, eg. the diffraction efficiency and the spectral dependence of fibre gratings, can be understood and modeled using coupled mode theory. A solution to Equation 2.1.12 yields the transverse component of the electric field, which may be written as a superposition of the modes [65] labeled j, in an ideal waveguide with no grating perturbation as

$$\vec{E}_t(x,y,z,t) = \sum_j \left[A_j(z)exp(i\beta_j z) + B_j(z)exp(-i\beta_j z)\right].\vec{e}_{jt}(x,y)exp(-i\omega t) \tag{2.1.42}$$

where $A_j(z)$ and $B_j(z)$ are the slowly varying amplitudes of the jth mode traveling in the +z and -z directions respectively. The modes are orthogonal in an ideal waveguide and do not couple. The presence of the grating, however, causes coupling of the modes

[65] described by

$$\frac{dA_j}{dz} = i\sum_k A_k(K^t_{kj} + K^z_{kj})exp\left[i(\beta_k - \beta_j)z\right] + i\sum_k B_k(K^t_{kj} + K^z_{kj})exp\left[i(\beta_k - \beta_j)z\right] \tag{2.1.43}$$

and

$$\frac{dB_j}{dz} = i\sum_k A_k(K^t_{kj} + K^z_{kj})exp\left[i(\beta_k - \beta_j)z\right] + i\sum_k B_k(K^t_{kj} + K^z_{kj})exp\left[i(\beta_k - \beta_j)z\right] \tag{2.1.44}$$

where, as before, A_j and B_j are the slowly varying amplitudes of the jth mode traveling in the +z and -z directions respectively. K^t_{kj} is the transverse coupling coefficient between modes j and k, defined as

$$K^t_{kj}(z) = \frac{\omega}{4}\iint_\infty dxdy\Delta\epsilon(x,y,z)\vec{e}_{kt}(x,y)\cdot\vec{e}^*_{jt}(x,y) \tag{2.1.45}$$

where $\Delta\epsilon \cong 2n\delta n$ when $\delta n \ll n$. K^z_{kj} is the longitudinal coefficient. K^z_{kj} is generally neglected as $K^z_{kj} \ll K^t_{kj}$ for fibre modes.

In most fiber gratings, the induced index change $\delta n(x,y,z)$ is uniform across the core and non-existent outside the core. The core index can be expressed as in Equation 2.1.38, with $\overline{\delta n}_{eff}(z)$ replaced with $\overline{\delta n}_{co}(z)$ [65]. A dc coupling coefficient, σ, due to the dc component of the refractive index modulation, and an ac coupling coefficient, κ, due to the periodically varying refractive index, can be defined as

$$\sigma_{kj}(z) = \frac{\omega n_{co}}{2}\overline{\delta n}_{co}(z)\iint_{CORE} dxdy\vec{e}_{kt}(x,y).\vec{e}^*_{jt}(x,y) \tag{2.1.46}$$

$$\kappa_{kj}(z) = \frac{v}{2}\sigma_{kj}(z) \tag{2.1.47}$$

The general coupling coefficient $K^t_{kj}(z)$ can then be written as [65]

$$K^t_{kj}(z) = \sigma_{kj}(z) + 2\kappa_{kj}(z)cos\left[\frac{2\pi}{\Lambda}z + \phi(z)\right] \tag{2.1.48}$$

The dominant interaction in a Bragg grating is the coupling of one mode, of amplitude $A(z)$, into an identical counter propagating mode, of amplitude $B(z)$. Equations 2.1.43 and 2.1.44 can be simplified by removing all terms except those involving the amplitude of the particular mode and [65] neglecting terms on the right hand sides of the differential equations containing a rapidly oscillating z dependence. This results in the following equations:

$$\frac{dR}{dz} = i\hat{\sigma}R(z) + i\kappa S(z) \tag{2.1.49}$$

and

$$\frac{dS}{dz} = -i\hat{\sigma}S(z) - i\kappa R(z) \tag{2.1.50}$$

where $R(z) \equiv A(z)(i\delta z - \frac{\phi}{2})$, $S(z) \equiv B(z)(-i\delta z + \frac{\phi}{2})$, κ is the ac coupling coefficient and $\hat{\sigma}$ is a general dc coupling coefficient. $\hat{\sigma}$ is defined as [65]

$$\hat{\sigma} \equiv \delta + \sigma - \frac{1}{2}\frac{d\phi}{dz} \tag{2.1.51}$$

where the detuning, δ, of the propagation constant with respect to the grating period

$$\delta \equiv \beta - \frac{\pi}{\Lambda} \tag{2.1.52}$$

$$= \beta - \beta_D \tag{2.1.53}$$

$$= 2\pi n_{eff}\left(\frac{1}{\lambda} - \frac{1}{\lambda_D}\right) \tag{2.1.54}$$

λ_D is defined as

$$\lambda_D \equiv 2n_{eff}\Lambda \tag{2.1.55}$$

When $\delta = 0$, $\lambda = 2n_{eff}\Lambda$, which is the same result as in Equation (2.1.41).

The derivative $(1/2)d\phi/dz$ describes a possible chirp of the grating period. Absorption losses can be described by a complex coefficient σ where the power loss coefficient is $\alpha = 2Im(\sigma)$.

2.1.12 FBG Fundamentals

The measured quantity is the peak reflected wavelength of the grating which changes as the grating is subjected to mechanical strain. This wavelength is usually measured using optical spectroscopy. Radiation of wavelength λ_0 will undergo strong reflection when it encounters the grating, provided that the grating equation (Equation 2.1.41) is satisfied as follows:

$$\lambda_0 = 2mn_1\Lambda \tag{2.1.56}$$

where m is an integer, n_1 is the effective refractive index and Λ is the spatial periodicity of the grating.

Typically, the grating pattern can be between 1 and 20 mm in length and, once formed, the grating behaves in a similar fashion to the Bragg acousto-optic grating. The reflectivity, R, at the Bragg wavelength can be estimated using the equation [8, 66]

$$R = tanh^2\Omega \tag{2.1.57}$$

where

$$\Omega = \pi n\left(\frac{L}{\lambda_B}\right)\left(\frac{\Delta n}{n}\right)\eta(V) \tag{2.1.58}$$

The factor

$$\eta(V) = 1 - \frac{1}{V^2}$$

is the fraction of the integrated fundamental mode intensity contained in the core. V is the normalised frequency of the fibre. R is directly proportional to the grating length, L, and the index perturbation, $\left(\frac{\Delta n}{n}\right)$, which is determined by the exposure power and time of the inscribing UV radiation for a specified fibre. The full width at half maximum (FWHM) bandwidth of a grating, $\Delta\lambda$, is given by [8]

$$\Delta\lambda = \lambda_B s\left[\left(\frac{\Delta n}{2n}\right)^2 + \left(\frac{1}{N}\right)^2\right]^{-\frac{1}{2}} \tag{2.1.59}$$

where $s \sim 1$ for strong gratings (near 100% reflectivity), $s \sim 0.5$ for weak gratings

and N is the number of grating planes. Because the index change is small, the main contribution to the linewidth is attributed to the change in modulation depth of the index perturbation.

When a thermo-mechanical strain gradient exists along the length of the grating, the reflection spectrum can broaden and develop multiple reflection peaks. The reflection spectrum of the grating under the most general strain state is given by [67]

$$I(\lambda) = \frac{I_0\sqrt{\frac{\alpha}{\pi}}}{L}\left(\left[P_x\int_{\lambda_x}\int_0^L S(\lambda)e^{-\alpha(\lambda-\lambda_{Bx}(z))^2}d\lambda dz \;+\; P_y\int_{\lambda_y}\int_0^L S(\lambda)e^{-\alpha(\lambda-\lambda_{By}(z))^2}d\lambda dz\right]\right) \tag{2.1.60}$$

P_x and P_y are given by

$$P_x = \frac{< E_{0x}^2 >}{< E_{0x}^2 > + < E_{0y}^2 >} \tag{2.1.61}$$

and

$$P_y = \frac{< E_{0y}^2 >}{< E_{0x}^2 > + < E_{0y}^2 >} \tag{2.1.62}$$

where $< E_{ox}^2 >$ and $< E_{0y}^2 >$ are the time averaged scalar magnitudes of the square of the electric fields in the $\hat{x}$ and $\hat{y}$ directions respectively. L is the length of the grating, I_0 is the intensity of the reflected light, $S(\lambda)$ is the intensity variation of the source as a function of wavelength and α is a constant which describes the FWHM of the grating spectrum. The integration takes into account the variation of the reflection spectrum along the length of the grating and the variation in the resonant wavelength for the two polarisation directions $\hat{x}$ and $\hat{y}$.

Most of the work reported in the literature using FBGs has centered on the use of the gratings for measurement of strain and temperature. The strain response arises due to two factors: the physical elongation of the sensor and the change in refractive index due to photoelastic effects. The thermal response results from the thermal expansion of the fibre and the temperature dependence of the refractive index.

Temperature and Strain Sensitivities

The response of the Bragg wavelength to both strain and temperature can be expressed as [10]

$$\Delta\lambda_B = 2n\Lambda\left(\left[1-\frac{n^2}{2}\{P_{12}-\nu(P_{11}+P_{12})\}\right]\varepsilon+[\alpha+\xi]\,\Delta T\right) \tag{2.1.63}$$

where ε is the applied strain, $P_{i,j}$ are the coefficients of the strain-optic tensor, ν is the Poisson ratio, α is the coefficient of thermal expansion of the fibre and ξ is the thermo-optic coefficient described previously.

The factor

$$\frac{n^2}{2}\left[P_{12}-\nu\left(P_{11}+P_{12}\right)\right] \tag{2.1.64}$$

is the effective photoelastic constant, p_e, and has a numerical value of 0.212 [9] for a typical silica optical fibre where P_{11} = 0.113, P_{12}=0.252, ν=0.16, and n=1.482.

Assuming isothermal conditions, the strain induced change in λ_B can therefore be expressed as [68, 69]

$$\frac{\Delta\lambda_b}{\lambda_B} = \left(1-p_e\right)\varepsilon \tag{2.1.65}$$

The term on the right of Equation 2.1.63 is the component of the wavelength shift due to temperature and is dependent on the change in dimension, the coefficient of thermal expansion, α, where

$$\alpha = \left(\frac{1}{L}\right)\left(\frac{dL}{dT}\right) \tag{2.1.66}$$

and is also dependent on the change in refractive index, the thermo-optic coefficient, ξ, where

$$\xi = \left(\frac{1}{n}\right)\left(\frac{dn}{dT}\right) \tag{2.1.67}$$

α has a numerical value of 1.1 x $10^{-6}/^{o}C$ and ξ has a value of 8.3 x $10^{-6}/^{o}C$ [60] for a silica fibre at 1550 nm.

Bragg Intra-grating Distributed Sensing

The change in the reflected Bragg wavelength with change in measurand can be obtained from [70]

$$\frac{d\lambda_B}{dX} = 2\left(\Lambda\frac{dn}{dX} + n\frac{d\Lambda}{dX}\right) \quad ; \quad X = T, P, \delta l... \tag{2.1.68}$$

where n = refractive index of the fibre, Λ = the spatial periodicity of the grating and X is the measurand in question, temperature (T), pressure (P) or strain (δl). Typical sensitivities at 1550 nm for the wavelength dependence in silica optical fibres are: strain ~ $1.2pm/\mu\epsilon$ and temperature ~ $12pm/^{o}$C [8].

The reflected wavelength of a grating, defined in Equation 2.1.41, can be related to the periodicity of the refractive index modulation along the fibre according to [71]

$$\lambda_B(z) = 2n(z)\Lambda(z) \tag{2.1.69}$$

Each section of the grating can contribute its own wavelength component to the reflected spectrum depending on the periodicity of the refractive index modulation, $\Lambda(z)$. If a uniform grating is subjected to a non-uniform measurand, the different wavelength components result in a broadened reflection spectrum and a reduction in the peak reflectivity [72]. Both the intensity and phase responses are affected and analysis of either permits calculation of $\lambda_B(z)$.

2.1.13 Grating Manufacture

Enhanced Photosensitivity

Photosensitivity of optical fibres can be thought of as the degree to which a change in the index of refraction of a fibre core can be realised following a specific exposure to UV light. The original change in refractive index observed by Hill *et al* [49] was estimated to be 10^{-6}. One of the problems associated with such a small index change is that, in order to achieve a detectable reflection, long gratings are required. Since the discovery

of the photosensitivty of fibres, there has been considerable research into increasing the photosensitivity.

While germanium (Ge) doped fibres have shown to be the most photosensitive, the germanium dopant is not essential to photosensitivity [73]. Doping of the core with Ge (≤ 10% mole), codoped with Boron (B) has achieved refractive index variations of $\sim 10^{-3}$ [73]. Hydrogen loading of optical fibres, typically carried out by diffusing hydrogen molecules into fibre cores at high pressures (> 1 atm) and temperatures (650 °C for 200 hrs), has been shown to achieve very high UV sensitivity [15]. The technique of enhancing fibre photosensitivity by hydrogenating fibres with a high concentration of germanium can achieve refractive index variations of 10^{-2} [73].

Grating Inscription

The internal writing technique of Hill *et al* [49], where the gratings are formed due to a standing wave pattern in the fibre, limits the periodicity of the grating, Λ, to the region where photosensitivity occurs, that is UV to ~ 500 nm. This in turn restricts the wavelength of the light reflected to these wavelengths. It was not until 1989, when G. Meltz and W. Morey, [50], at United Technologies Research Centre, reported that reflective gratings could be induced, or written, in germania doped fibres that gratings took on a more practical significance.

Many schemes have been proposed for grating manufacture, which may be broadly classified into two techniques, holographic and non-holographic. Holographic inscription of standard FBGs uses a beamsplitter to divide the UV beam to follow two paths to the fibre and then interfere at the fibre (an interferometer) to expose the fibre to an interfering beam of UV light. Non-holographic, or non-interferometric inscription, generally depends on exposure of the fibre to a pulsed source or exposure to a beam through a phase mask [15].

Holographic or Interferometric Inscription

This method for FBG manufacture, first demonstrated by Meltz and Morey [50], involves exposing the fibre to overlapping coherent UV beams (Figure 2.6). The incident UV beam is divided to follow two separate paths and then recombined by reflection from two mirrors. An advantage of this holographic technique is that the grating can be tailored to reflect at any wavelength by varying the angle between the beams [11,15]. Therefore, although UV light is used, the grating can be tailored to reflect at any wavelength of interest, for example, at much longer wavelengths in a spectral region more suited to applications in fibre optic communications and fibre optic sensing.

By exposing the fibre to interfering beams of UV radiation between 240 nm to 250 nm a change in refractive index of the fibre takes place, as illustrated in Figure 2.6. The change in refractive index is relatively small, typically less than 10^{-4} [74] but it is permanent once the inscription process has finished. The formation of gratings during the inscription process is described in more detail in Section 2.1.14.

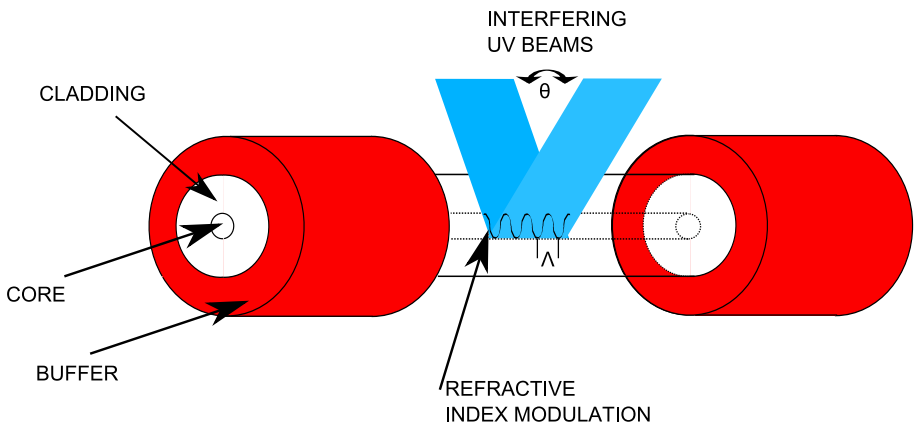

Figure 2.6: Standard UV inscription of FBGs.

A variation in the angle, θ, between the two interfering beams allows tailoring of the periodicity of the grating, Λ, as the periodicity is related to the wavelength of the light and θ by

$$\Lambda = \frac{\lambda}{2Sin\theta} \tag{2.1.70}$$

Therefore, the grating structure can be written at wavelengths where losses in optical

fibres are minimised. However, the holographic technique for grating manufacture has been largely superseded by the phase mask technique because of the advantages outlined below.

Fabrication by Phase Mask

UV light, which is incident normal to the phase mask is diffracted by the periodic corrugations in the phase mask. The phase mask is constructed to suppress the diffraction into the zero order mode. The ± 1 order diffracted beams interfere to produce an interferogram that photo-imprints a corresponding grating in the optical fibre. If the period of the phase mask is Λ_{mask}, the period of the induced grating is $\Lambda_{mask}/2$. This is again independent of the wavelength of the UV source [75].

The phase mask technique has three main advantages. Firstly, it greatly simplifies and reduces the cost of the grating manufacturing process by offering easier alignment. Secondly, there are reduced stability requirements on the inscription apparatus. Thirdly, there are lower coherence requirements on the inscribing source. It can be used to fabricate gratings with a controlled spectral response, e.g. apodisation of the secondary maxima, which is desirable in applications using Wavelength Division Multiplexing (WDM). Apodisation of the side lobes is achieved by varying the amplitude of the coupling coefficient along the length of the grating. One phase mask technique for apodisation involves varying the groove size, thereby varying the intensity of the diffracted beams and changing fringe contrast, resulting in a variation of the amplitude of the induced refractive index modulation [75]. An advantage of this technique for apodisation is that the characteristics of the gratings are reproducible.

However, the primary draw-back of the phase mask technique for inscription is that only limited tuning of the Bragg wavelength is achievable by pre-straining the fibre prior to exposure. Therefore, a separate phase mask or inscription using a tunable laser source is required for each Bragg wavelength [76].

Point by Point Method for Inscription

Another process for fabrication of gratings is the point-by-point method [77]. This method is achieved by exposure of the core to a focused pulsed source. The change in refractive index along the core is then accomplished one step at a time. The fibre is translated through a distance corresponding to the pitch of the grating in a direction parallel to the fibre core. This process is repeated to form the grating structure. The main advantage of the point by point method is flexibility in grating design. Variations in grating length, grating pitch and spectral response can easily be incorporated [9]. The point-by-point method has also been demonstrated for inscription of FBGs in the drawing process of the fibre, eliminating the need for removal of the buffer when writing using UV wavelengths [53].

The use of a focused femtosecond laser beam for point-by-point inscription, [51], has opened up the possibility for grating inscription using near infrared (NIR) laser light at a wavelength of 800 nm. Inscription using NIR lasers has the added advantage of elimination of the requirement for the stripping of the buffer from the fibre as the sensitivity to UV radiation is no longer an issue. Some disadvantages of the point-by-point method are that it is a slower method of inscription, good alignment is required and expensive translation stages are required to provide the highly accurate positioning necessary for inscription.

The different techniques for inscription of FBGs has resulted in gratings which can be classified into different types depending on the inscription mechanism.

2.1.14 Classification of Fiber Bragg Gratings According to Photosensitisation

A number of different types of FBG have been distinguished on exposure of the core of a photosensitive optical fibre to a UV laser interference pattern [78, 79]. These different types of grating can be characterized by different spectral and thermal behaviors and are caused by the UV excitation of distinct physical mechanisms. The classification of the types depends on the initial writing conditions (laser power and wavelength,

continuous wave (CW) or pulsed energy delivery) and fibre properties [80].

Type I Gratings

The standard method of grating inscription, where the amplitude of the index modulation increases with total UV irradiation fluence to saturation, is now referred to as a type I grating. This type of grating is the least stable at high temperatures.

Type IIA Gratings

Another type of grating is formed in non-hydrogen loaded fibres after exposure of the core to low intensities after long exposure. Initially, a type I grating is formed and shows different stages of evolution after continued exposure, growth, saturation, decay and disappearance. Erasure of the type I grating is followed by the growth of the N=1, or type IIA, grating which is characterised by negative refractive index changes. This grating is stronger than the original grating and able to withstand higher temperatures [79].

Type II gratings

Another, different, type of grating is produced when the energy of the writing beam is increased above approximately 30 mJ. At energy levels of 30 mJ, there is a sharp threshold above which the induced index modulation increases dramatically. Physical damage is caused in the fibre core. These gratings are referred to as type II and have very high reflectivities ~ 100% and large bandwidths [78].

Type IA gratings

Type IA gratings are fabricated in an identical fashion to type IIA gratings as described above, but only form in hydrogenated fibre [81]. Type IA gratings exhibit a large positive shift in the Bragg wavelength. This is in contrast to the negative shift seen in the fabrication of type IIA gratings.

2.1.15 Grating Characterisation

Bragg reflection characteristics of a fibre grating are controlled by the longitudinal refractive index distribution, i.e. the grating period and the depth of effective index modulation. Typically, gratings are only characterised by their reflection spectrum. However, the retrieval of the longitudinal index distribution is important for controlling the characteristics of a grating. For example, the reconstruction of refractive index profiles has been demonstrated from calculation of the envelope of index change. This was done using the complex coupling coefficient reconstructed from measurement of the intensity and phase of the Bragg reflection using an interferometric arrangement [82]. However the algorithm used is based on the coupled mode equations and simplified using Fourier transformation, resulting in limited spatial resolution. It is therefore incapable of detecting an abrupt change in the index profile.

Optical low coherence reflectometry (OLCR) is a technique that has been developed to characterise the position of weakly reflecting defects in optical waveguide elements [83]. This non-destructive method can precisely determine the location, length and coupling coefficient of the grating. This technique has been demonstrated to measure the modulation depth of the sinusoidal index variation to a relative precision of 1% [84].

2.1.16 FBG Interrogation Schemes

Considerable research has focused on fibre Bragg gratings, and particularly on systems using the gratings for sensing strain or temperature variations [61, 85]. The variation, encoded in the light reflected from the grating, requires precise measurement of the FBG wavelength shift induced by the measurand for achieving good sensor performance. An ideal interrogation system requires high resolution, typically ranging from sub-picometer to a few picometers wavelength resolution, with a large measurement range. The system should be capable of demodulating multiplexed gratings, particularly as the gratings are ideally suited to WDM [76].

The development of supercontinuum broadband sources releases the potential for serial multiplexing of fibre Bragg gratings over far greater wavelength ranges than previously reported [86, 87]. Many interrogation techniques have been demonstrated for interrogation of FBGs, such as: the drift compensated interferometric wavelength shift detection system reported by Kersey *et al* [88]; the frequency modulated laser diode reported by Ferreira [89] and the dual interferometric cavity system reported by Rao *et al* [90]. Other schemes include: interrogation by an optical spectrometer [91]; interrogation by using matched sensor and receiver grating pairs reported by Brady *et al* [92]; a combination of the interferometric wavelength scanner reported by Kersey [88] and a low resolution optical spectrometer reported by Rao *et al* [93] for multiplexed sensors; the ratiometric technique of Melle *et al* [94]; and the fibre Fourier transform spectrometer of Davis and Kersey [24].

These, and other established techniques including tunable filters [95–97], tunable lasers [89, 98, 99] and diode array [100], are limited in their abilities for interrogation over broad wavelength ranges. They are also limited in their provision of simultaneous measurement of all gratings in an array or provision of high resolution measurement of the intra-grating structural detail of the individual gratings in the sensing array, which could potentially be valuable in the detection of non-uniform measurand fields [72].

Fourier transform spectroscopy (FTS) exhibits a fundamental advantage over the above demodulation techniques because the full wavelength range is characterised within the captured interferogram. This advantage, known as the Fellgett advantage or multiplex advantage [101], will be exploited in the work reported in this thesis for the characterisation and demodulation of grating arrays over broad wavelength ranges. FTS also provides the possibility of high resolution measurement of the intra-grating structural detail. The drift compensated interferometric wavelength shift detection system reported by Kersey *et al* [88] is applied to the interrogation of a sensing grating in the work reported in chapter 3, where the inability of the system for interrogation of chirped gratings is demonstrated. The following sections will develop the measurement theory behind the interferometric techniques reported on in later chapters.

2.2 Optical Measurement

Introduction

The area of lightwave measurement is a rapidly evolving field in the science of optics. Modern sensing systems can incorporate multiple wavelength channels propagating on a single fibre [102]. Multiple wavelength systems are referred to as being wavelength division multiplexed (WDM) [23]. Fibre Bragg gratings are ideally suited to WDM where typical responses for strain and temperature are: strain $\sim 1.2pm/\mu\epsilon$ and temperature $\sim 12pm/^{o}$C [8]. Grating interrogation units, therefore, have to be capable of providing high wavelength resolution measurement (approaching picometer accuracy).

In the telecommunications field, early systems had wide wavelength spacings and therefore did not have to be especially concerned with spectral content. More recent systems have much narrower spacing between channels and are referred to as dense wavelength division multiplexed (DWDM) [23]. Consequently, for telecommunication applications, wavelengths too need to be measured with much higher accuracy.

Optical spectral analysis (the measurement of optical power as a function of wavelength) can be conducted with a variety of different instrumentation configurations which can be broadly classified into two groups [23]:

- Diffraction grating based spectrum analyzers where the light is diffracted by the grating at an angle proportional to the wavelength. Typical commercially available grating based optical spectrum analyzers have wavelength resolutions of $\sim$ 0.01 nm.

- Wavelength meters, typically interferometers, which can discriminate wavelength by filtering or by interferometric fringe counting techniques and can achieve high resolution wavelength measurement to better than $\sim$ 0.001 nm accuracy.

The interrogation units described in the later chapters of this thesis are wavelength meters, in which measurements are made by direct comparison of a lightwave with

itself or a delayed version of itself. The following sections develop the theory of the measurements made in subsequent chapters.

2.2.1 Coherence and Interference

Coherence theory describes the correlation between beams of light [64]. Neither fully coherent or completely incoherent light actually exists, so that all light may be considered partially coherent [64]. The work in this thesis is based on the use of two beam interferometers that are illuminated by partially coherent sources for measurements which are based on the recovery of interferogram phase. The degrees of coherence of the sources range from highly coherent Helium-Neon (HeNe) gas lasers to a much less coherent broadband superluminescent diode.

2.2.2 Temporal and Spatial Coherence

Coherence effects can be separated into two classifications, temporal and spatial coherence. A high degree of spatial coherence exists between wavetrains emitted from the same point in space. For example, it is helpful to consider an extended monochromatic source. In this instance, the effects of temporal coherence are greatly minimised as all of the wavetrains are emitted at the same time from spatially distinct points on the source. The spatial coherence can then be considered as the lateral distance over which the wavetrains appear to have constant phase [3].

When considering temporal coherence, if we consider a wavetrain from a continuously emitting point source with limited spatial extent, the temporal coherence can be thought of as a measure of the time over which the wavetrains appear to have constant phase [3].

As fully coherent sources are not achievable, i.e. sources containing a single frequency, the spectral line of each source has a frequency bandwidth $\delta\nu$. The frequency bandwidth is the same order of magnitude as the reciprocal of the temporal extent of the pulse [3].

$$\Delta\nu \approx \frac{1}{\Delta t} \tag{2.2.1}$$

The time that satisfies this equation is called the coherence time and the corresponding coherence length is

$$\Delta l_c = c\Delta t_c \tag{2.2.2}$$

The coherence length is the extent in space over which the wave maintains a near constant phase relationship and can therefore exhibit interference.

2.2.3 Interference

Optical interference occurs from the interaction of two or more lightwaves that yield a resultant irradiance that deviates from the sum of the component irradiances [3]. The expression which describes optical interference is a second order linear homogenous partial differentiation equation which obeys the principle of superposition. In accordance with the principle of superposition, the electric field intensity, $\hat{E}$, at a point in space arising from the separate fields of various contributing sources is

$$\hat{E} = \hat{E}_1 + \hat{E}_2 + ... \tag{2.2.3}$$

The optical disturbance, or light field $\hat{E}$, varies at an exceedingly rapid rate ($\sim 10^{14}$ Hz) making the field an impractical quantity to detect. The irradiance, however, can be detected by a wide variety of sensors. The irradiance is the time average of the electric field intensity squared [3],

$$I =< E^2 >_T \tag{2.2.4}$$

Figure 2.7 [3, 64] illustrates the operation of a two beam interferometer. The observable irradiance at points P_1 and P_2 is proportional to the mean value of $E(P,t)^2$ so that, apart from an inessential constant, [3, 64]

$$I(P) = 2 < E(P,t)^2 >_T \tag{2.2.5}$$

The disturbance at Q can then be obtained using the principle of superposition [64]

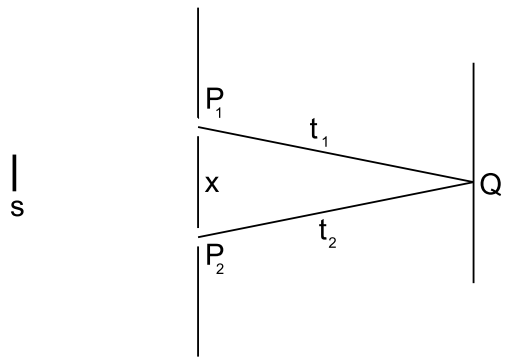

Figure 2.7: Two beam interferometer illuminated by an extended source S [3, 64]

$$E(Q) = K_1 E(P_1, t - t_1) + K_2 E(P_2, t - t_2) \tag{2.2.6}$$

where P_1 and P_2 are the centres of secondary emission and t_1 and t_2 are the times taken for the light to travel from P_1 to Q and P_2 to Q respectively. The propagators K_1 and K_2 are purely imaginary and mathematically affect the alterations in the field resulting from traversing the apertures.

The irradiance at Q is therefore, recalling Equation 2.2.4,

$$I(Q) = |K_1|^2 I_1 + |K_2|^2 I_2 + 2|K_1||K_2| I_{12} \tag{2.2.7}$$

The I_{12} term is known as the interference term and is the time average of the electric field intensities squared and is referred to as the mutual coherence function.

2.2.4 Mutual Coherence and the Degree of Coherence

The key function in the theory of partially coherent light is the mutual coherence function, a complex quantity which is the time averaged value of the cross correlation function of the electric field intensity, $\hat{E}$ denoted [3, 64]

$$\tilde{\Gamma}_{12}(\tau) = < \tilde{E}_1(t + \tau), \tilde{E}_2(t) > \tag{2.2.8}$$

This cross-correlation is fundamentally related to the spectrum of the source by the Wiener-Khintchine theorem. This theorem relates two important characteristics of a random process: the power spectrum of the process and the correlation function of the process, i.e. if

$$f(t) = \sum_n f_n \; e^{i\lambda_n t} \tag{2.2.9}$$

then

$$\lim_{T\to\infty} \frac{1}{2T} \int_{-T}^{T} f(t+\tau) \; f(t) \; dt = \sum_n |f_n|^2 \; e^{i\lambda_n \tau} \tag{2.2.10}$$

where the left hand side of Equation 2.2.10 is a correlation function and the right hand side is the power spectrum [103]. The mutual coherence function, $\tilde{\Gamma}_{12}(\tau)$, is the optical analogue of the cross power spectrum in the theory of stationary random processes [64].

Normalising $\tilde{\Gamma}_{12}(\tau)$ gives the complex degree of coherence, $\tilde{\gamma}_{12}(\tau)$, as [104]

$$\tilde{\gamma}_{12}(\tau) = \frac{\tilde{\Gamma}_{12}(\tau)}{\sqrt{\tilde{\Gamma}_{11}(0)\tilde{\Gamma}_{22}(0)}} \tag{2.2.11}$$

Equation 2.2.7, using Equations 2.2.8 and 2.2.11 [3,64], can be written as

$$I(Q) = I_1(Q) + I_2(Q) + 2\sqrt{I_1(Q)}\sqrt{I_2(Q)}\mathbf{R}[\gamma_{12}(\tau)] \tag{2.2.12}$$

where $I_1(Q) = K_1^2 I_1$ is the intensity that would be observed at Q if only aperture P_1 was open, $I_2(Q) = K_2^2 I_2$ is the intensity at Q if only P_2 was open, $\tau = t_2 - t_1$ and the oscillatory component or interference term is

$$I_{OS}(\tau) = 2\sqrt{I_1(Q)}\sqrt{I_2(Q)}\mathbf{R}[\gamma_{12}(\tau)] \tag{2.2.13}$$

The complex degree of coherence relates to the phase angle of the fields [3,64] and can be expressed as

$$\gamma_{12}(\tau) = |\gamma_{12}(\tau)| e^{i\phi_{12}(\tau)} \tag{2.2.14}$$

or

$$\mathbf{R}[\gamma_{12}(\tau)] = |\gamma_{12}(\tau)| cos[\alpha_{12}(\tau) - \phi] \tag{2.2.15}$$

where $\alpha_{12} - \phi$ yields the phase difference between the fields and results in an irradiance which can be greater than, less than, or equal to $I_1 + I_2$. The treatment of interference has so far neglected polarization effects to allow for a scalar treatment. The next section will introduce a vectorial treatment for the case of polarized fields which can lead to an effect known as polarization induced fading [105].

2.2.5 Polarization

Representation of the polarized nature of light requires a vectorial treatment. Two orthogonally polarized waves will not interfere, a fact first observed by Fresnel and Arago [3]. In a similar manner to complete coherence or complete incoherence, which represent two extremes, the variation of the field vectors is generally partially polarized.

The observable effects depend on the intensities of any two mutually orthogonal components of the electric field vector at right angles to the direction of propagation, and on any degree of correlation that exists between them. The components of the electric field can be written using the complex representation associated with real components of the electric field as [64]

$$E_x(t) = a_1(t) e^{i[\phi_1(t) - 2\pi\tilde{\nu} t]} \tag{2.2.16}$$

$$E_y(t) = a_2(t) e^{i[\phi_2(t) - 2\pi\tilde{\nu} t]} \tag{2.2.17}$$

In a manner analogous to the treatment of partially coherent light, an expression for the intensity fluctuations due to partially coherent polarised light can be obtained by introducing a complex correlation factor, j_{xy} [64]. This has a similar significance as

the complex degree of coherence, $\gamma_{12}(\tau)$, where

$$j_{xy} = |j_{xy}|e^{i\beta_{xy}} \tag{2.2.18}$$

where $|j_{xy}|$ is a measure of the 'degree of coherence' and β_{xy} is a measure of the effective phase difference.

The intensity, $I(\theta,\epsilon)$, where one component is subjected to a retardation ϵ, can be obtained from

$$I(\theta,\epsilon) = j_{xx}Cos^2\theta \ + \ j_{yy}Sin^2\theta \ + \ 2\sqrt{j_{xx}}\ \sqrt{j_{yy}}\ \ Cos\theta\ \ Sin\theta\ \ |j_{xy}|\ \ Cos(\beta_{xy}-\epsilon) \tag{2.2.19}$$

where the j_{xx},... are elements of the coherency matrix [64]

$$\mathbf{J} = \begin{bmatrix} < E_x E_x^* > & < E_{xy} E_{xy}^* > \\ < E_{yx} E_{yx}^* > & < E_{yy} E_{yy}^* > \end{bmatrix} = \begin{bmatrix} < a_1^2 > & < a_1 a_2 e^{i(\phi_1-\phi_2)} > \\ < a_1 a_2 e^{-i(\phi_1-\phi_2)} > & < a_2^2 > \end{bmatrix}$$

and assuming $j_{yx} = j_{xy}^*$ and θ is the angle that the direction of the light vibration makes with the positive xaxis, i.e.

$$E(t;\theta,\epsilon) = E_x Cos\ \theta + E_y\ \ e^{i\epsilon} Sin\ \theta \tag{2.2.20}$$

The polarization state of a lightwave propagating through non-polarization maintaining fibre can drift randomly with environmentally induced changes in the fibre residual birefringence. In a non-polarization maintaining fibre interferometer, these drifts in polarization can lead to polarization fading and reduced sensitivity [105]. In a mechanically scanned fibre interferometer, where the scanning mechanism is fibre stretching, birefringence is introduced to the fibre. The changes in the fibre birefringence due to stretching can also lead to polarization fading.

2.2.6 Interferometry

The main problem in producing interference is that the beams must be coherent. Separate, independent, adequately coherent sources do not exist apart from the laser. This dilemma was first solved 200 years ago by Thomas Young in his classic double beam experiment. In an attempt to establish the wave nature of light he repeated an experiment first attempted by Grimaldi 140 years earlier. Grimaldi admitted sunlight into a dark room through two pinholes in an opaque screen. The idea was to show that where the circles of light overlapped darkness could result. Young repeated the experiment but this time he passed the sunlight through an initial pinhole, which became the primary source. This had the effect of creating a spatially coherent beam that could identically illuminate the two apertures, known as a wavefront splitting interferometer. He took a single wavefront, split it into two coherent sources and observed them interfere [3].

An amplitude splitting interferometer works according to the same principle. An all-fibre Sagnac interferomter was illustrated in Figure 2.5. In a bulk optic, mirrored, amplitude splitting interferometer the beam entering the interferometer is passed through a semi-transparent material in which half of the beam is reflected and the other half transmitted. The two beams are forced to travel two separate paths before being recombined at a detector to produce an interference pattern, provided the original coherence between the two beams has not been destroyed.

2.2.7 Michelson Interferometer

By far the best known amplitude splitting interferometer is the Michelson interferometer [3]. A customised version can be seen in Figure 2.8. Light which is launched into the interferometer is divided to follow two different paths, one to a movable mirror M1 and the second to a fixed mirror M2. If the optical path difference between the arms of the interferometer is less than the coherence length of the source, interference fringes will be observed at the detector. As the movable mirror is displaced by $\lambda_0/2$

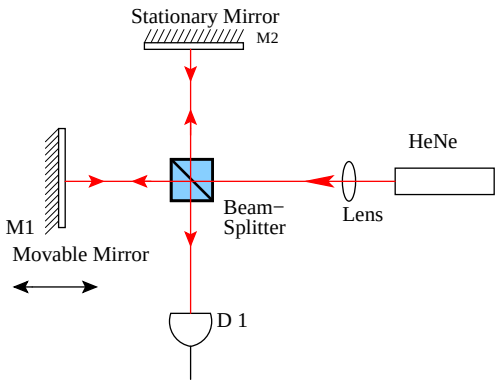

Figure 2.8: Customised version of Michelson Interferometer

each fringe will move to the position previously occupied by the adjacent fringe. Therefore, a scan of the optical path in one arm of the interferometer produces a symmetric interferogram at the detector centered about the position where all the components of the recombining beam are in phase.

If τ is the relative time delay in the arms of the interferometer, then the intensity at the detector, $I(\tau)$, can be represented as the sum of a constant component, I_0, and an oscillatory component, $I_{os}(\tau)$. The oscillatory component of the interferogram is proportional to the real component of the mutual coherence function, $\tilde{\Gamma}_{12}(\tau)$, Equation 2.2.8.

This cross-correlation is fundamentally related to the spectrum of the source through the Wiener-Khintchine theorem, as discussed in Section 2.2.4. Normalising $\tilde{\Gamma}_{12}(\tau)$ gives the complex degree of coherence, $\tilde{\gamma}_{12}(\tau)$, Equation 2.2.11, so that the oscillatory component of the interferogram $I_{os}(\tau)$ can be related to the real component of the complex degree of coherence [104] as

$$I_{os}(\tau) \propto R\left[\tilde{\gamma}_{12}(\tau)\right] \tag{2.2.21}$$

where R [ ] represents the real component of a complex number.

Assuming the fields are stationary and using the Wiener-Khintchine theorem [104],

$$\tilde{\gamma}_{12}(\tau) = \int_{-\infty}^{\infty} \hat{G}(\omega) exp(-i\phi_{12}(\omega)) exp(-i\omega\tau) d\omega \tag{2.2.22}$$

where $\hat{G}(\omega)$ is the normalised spectral distribution function of the source. It can be seen that the complex spectrum $\hat{G}(\omega)exp(-i\phi_{12}(\omega))$ and $\tilde{\gamma}_{12}(\tau)$ are a Fourier transform pair.

$$\tilde{\gamma}_{12}(\tau) = F^{-1}\left[\hat{G}(\omega)exp(-i\phi_{12}(\omega))\right] \tag{2.2.23}$$

Therefore

$$\hat{S}(\omega) \equiv \hat{G}(\omega)exp(-i\phi_{12}(\omega)) = F\{2R\left[\tilde{\gamma}_{12}(\tau)\right]\} \propto F\{I_{os}(\tau)\} \tag{2.2.24}$$

The quality of the fringes produced by an interferometric system can be described using the visibility, defined by Michelson as [106].

$$V(r) \equiv \frac{I_{max} - I_{min}}{I_{max} + I_{min}} \tag{2.2.25}$$

For two interfering beams the visibility, or contrast, is [106]

$$V(r) = \frac{2\ \sqrt{I_1}\ \sqrt{I_2}}{I_1 + I_2} \tag{2.2.26}$$

where I_1 and I_2 are the intensities due to the individual beams. The visibility is a maximum when $I_1 = I_2$.

The Michelson interferometer has been applied to high resolution spectroscopy, measurement of atomic length standards and stellar interferometry [3].

2.2.8 Mach-Zehnder Interferometer

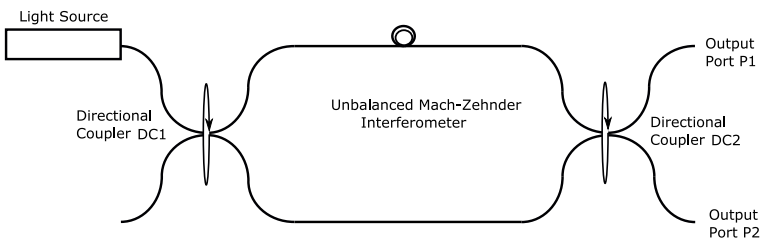

Figure 2.9: All-fibre Mach-Zehnder Interferometer

A Mach-Zehnder interferometer is another amplitude splitting interferometer, Figure 2.9 shows a fibre version, where light from the source is coupled into a sensing and reference arm by directional coupler DC1. The two beams recombine at directional coupler DC2 to produce an interferogram observable at both output ports P1 and P2. The intensity detected at the output is [35, 107]

$$I = I_0[1 \ - \ V \ Cos(\phi_a - \phi_b)] \tag{2.2.27}$$

where V is the visibility, ϕ_a and ϕ_b are the phase retardance of the signal and reference arms and I_0 is the source intensity.

In general the lengths of the two arms in the interferometer are not equal, giving rise to a path length difference $\Delta L = L_1 - L_2$. The output spectrum of a fibre Mach-Zehnder interferometer exhibits modulation [108, 109], characterized by a series of equally spaced transmission peaks enabling the use of the interferometer as a comb filter for a variety of applications [110, 111]. For light launched into the interferometer, the intensity transmission is, neglecting polarisation dependence, [110]

$$T = \frac{1}{2}\left(1 - Cos \ \phi\right) \tag{2.2.28}$$

where ϕ is the phase difference between the two arms given by

$$\phi = \beta_0 \Delta L \tag{2.2.29}$$

β_0 is the propagation constant of the fundamental mode in an optical fibre. The interference spectrum at the output can be obtained from [112]

$$S_{out}(\omega) = S_0(\omega)[1 + |\mu| Cos(\beta_0 \Delta L)]/2 \tag{2.2.30}$$

where S_0 is the source spectrum and $|\mu|$ is the spectral visibility.

This period of the transmission peaks (or spectral fringes) is inversely proportional

to the to the optical path difference between the two beams [113]. The free spectral range (FSR) is defined as

$$FSR = \frac{\lambda^2}{\Delta_{OPD}} \tag{2.2.31}$$

λ is wavelength of the illuminating light and Δ_{OPD} is the optical path difference between the arms of the interferometer.

2.2.9 Interferometric Fourier Transform Spectroscopy

Interferometry allows the retrieval of the difference in spectral phase between two time delayed light pulses. This allows measurement of the complex transfer function of an optical element by use of a broadband light source and characterisation of the electric field of an unknown pulse.

The basic Fourier transform spectrometer consisting of a Michelson interferometer usually has one arm of the interferometer linearly scanned to create an interferogram at the output. Equation 2.2.11 illustrates the dependence of the frequency spectrum obtained from an interferogram generated by scanning one arm of an intererometer on the introduced delay, τ. The frequency of the fringes, f, observed at the output is a function of the scanning velocity [24]

$$f = \frac{2V_m\nu}{c} = 2V_m\bar{\nu} \tag{2.2.32}$$

where $\bar{\nu}$ is the wavenumber of the light.

The minimum resolvable wavelength, $\delta\lambda$, in Fourier transform spectroscopy, is determined by the total path length scan, τ_Δ [23].

$$\delta\lambda = n_a\frac{\lambda^2}{c\tau_\Delta} \tag{2.2.33}$$

where n_a is the group index of air and c is the speed of light in a vacuum. This implies that long scans are required to achieve high resolution.

Non-uniform sampling of the interferometric OPD, is a consequence of the non-

uniform scanning of mechanical components. It manifests itself as uneven delay values which have the effect of broadening the correlation peaks. Many FTS approaches overcome non-uniform scan velocity by triggering the signal sampling on the zero crossings of a simultaneously captured reference interferogram [114, 115] or by phase locked loop control of the scan velocity [24].

However, a technique has been developed by Flavin *et al* [116, 117] for absolute wavelength measurement without the need for sophisticated electronics. This technique is based on the comparison of the phase vectors of the reference and measurand beams. Retrieval of the phase vectors for the beams are obtained via Hilbert transformation. The next section will introduce the concepts necessary to conduct calibration of the delay in an interferometer using the Hilbert Transform Technique.

2.2.10 Hilbert Transform Technique for OPD Calibration

In the analysis of real signals the theory of Hilbert transforms is closely tied to the theory of Fourier transformations. The signal processing techniques adopted for delay calibration in the experimental work in chapters 4, 5 and 6 are based on the retrieval of temporal phase vectors from the acquired interferograms via Fourier transformation. The extracted phase vectors effectively map the delay in the interferometer and allow for correction for non-uniformities in sampling of the delay.

2.2.11 The Fourier Transform

Fourier transformation is regularly used in signal processing to analyze the frequency content of signals. The Fourier transform of a time function, $u(t)$, is defined by the integral

$$U(f) = \int_{-\infty}^{\infty} u(t) e^{-i\omega t} dt \quad ; \quad \omega = 2\pi f \tag{2.2.34}$$

$$u(t) = \int_{-\infty}^{\infty} U(f) e^{i\omega t} df \tag{2.2.35}$$

where f is the Fourier frequency. The complex spectrum is one sided, [64, 118], i.e it only exists at positive frequencies or only at negative frequencies for the conjugate signal. The Fourier transform of a complex signal can be converted to amplitude and phase spectra via cartesian to polar coordinate conversion [118] where the real and imaginary parts of the complex number are treated as X and Y dimensions respectively.

The Fourier spectrum of a real signal exists at positive and negative frequencies [64, 118]. A real disturbance at a fixed point in space can be expressed in the form of a Fourier integral

$$u^r(t) = \int_0^\infty a(\omega) cos[\phi(\omega) - \omega t] d\omega \tag{2.2.36}$$

where $a(\omega)$ is the amplitude, $\phi(\omega)$ is the phase and $\omega = 2\pi f$ is the angular frequency, f is the frequency of the disturbance.

An associated complex function can be generated [64]

$$u(t) = \int_0^\infty a(\omega) exp\{i[\phi(\omega) - \omega t]\} d\omega \tag{2.2.37}$$

so that [64]

$$u(t) = u^r(t) + i u^i(t) \tag{2.2.38}$$

where the imaginary part $u^i(t)$ is given by

$$u^i(t) = \int_0^\infty a(\omega) Sin[\phi(\omega) - \omega t] d\omega \tag{2.2.39}$$

where $u^i(t)$ is found by replacing the phase $\phi(\omega)$ of each Fourier component by $\phi(\omega) - \pi/2$ in the real component, $u^r(t)$ [64].

If the Fourier spectrum of a complex function contains no negative frequencies, then the real and imaginary parts are Hilbert transforms of each other [64, 118].

Therefore, to retrieve information on amplitude and phase via Fourier transformation, a real signal can be represented as a complex exponential. The real part of the

complex exponential contains all of the information about the waveform of the time signal. This complex representation is known as the analytic signal and is obtained via Hilbert transformation of the real signal as described below.

2.2.12 The Hilbert Transform and the Analytic Signal

The Hilbert transform of a signal is defined to be the signal whose frequency components are phase shifted by 90° with respect to the original signal [64, 118]. The Hilbert transform is used in complex analysis to generate a complex analytic signal from a real signal.

The Hilbert transform, $y(t)$, of a time function, $x(t)$, is written in the form [118]

$$y(t) = H[x(t)] = \frac{1}{\pi}\int_{-\infty}^{\infty}\frac{x(t')}{t-t'}dt' \tag{2.2.40}$$

The divergence at t is allowed for by taking the Cauchy Principle Value of the integral [119]. The Hilbert transform is frequently written in terms of convolution notation [118]

$$H(t) = \frac{1}{\pi t} * f(t) \tag{2.2.41}$$

$$f(t) = 1\frac{1}{\pi t} * H(t) \tag{2.2.42}$$

The Fourier transform of $-(\pi t)^{-1}$ is the odd function $i\ sgn\ f$, (f is the Fourier frequency) which is equal to $+i$ for positive f and $-i$ for negative f. The Hilbert transform is equivalent to a form of filtering where the amplitudes of the spectral components are left the same but the phases are altered by $\pi/2$, positively or negatively according to the sign of f [118, 119].

A complex signal can be associated with a real signal where the imaginary part is the Hilbert transform of the real part. This is known as the analytic signal (A(t)) [118–120] and becomes

$$A(t) \;=\; x(t) + iy(t) \;=\; a(t)e^{i\phi(t)} \tag{2.2.43}$$

The analytic signal can be used to play the same role as a complex signal for more

general waveforms. Any sinusoid **A cos**$(\omega t + \phi)$ may be converted to a positive frequency complex sinusoid by generating a phase quadrature component **A sin**$(\omega t + \phi)$ to serve as the imaginary part given by

$$A e^{i(\omega t+\phi)} = A\,cos(\omega t + \phi) + i\,A\,sin(\omega t + \phi) \tag{2.2.44}$$

For a complex signal which is expressible as a sum of many sinusoids, a filter can be constructed which shifts each sinusoidal component by a quarter cycle. These filters are called Hilbert transform filters.

When a real signal, x(t), and its Hilbert transform, y(t)=H$\{x(t)\}$ are used to form a new complex signal $z(t) = x(t) + iy(t)$, the signal $z(t)$is the complex analytic signal corresponding to the real signal $x(t)$. The analytic signal can be generated via Fourier transformation of the real signal as the corresponding analytic signal for any real signal has the property that all of the negative frequencies have been filtered out [118, 119].

The analytic signal is a generalisation of the phasor [119] and the amplitude and the phase can be calculated from

$$a(t) = \sqrt{x(t)^2 + y(t)^2} \tag{2.2.45}$$

$$\phi(t) = tan^{-1}\left(\frac{y(t)}{x(t)}\right) \tag{2.2.46}$$

The analytic signal can be used to play the same role as a complex signal for more general waveforms.

The intensity of a beam at the output of an interferometer can be represented as a function of the delay, τ between the arms of the interferometer [116].

$$I(\tau) = A(\tau)cos(\omega\tau + \xi) \tag{2.2.47}$$

where ω and ξ are the frequency and initial phase terms respectively. The signal phase

can therefore be written as

$$\phi(\tau) = \omega\tau + \xi \tag{2.2.48}$$

effectively mapping the delay in the interferometer arms. The points, while equally sampled in time, are not equally sampled in terms of delay, τ, because of the non-uniform scanning velocity of the mechanical components in the interferometer [117]. This non-uniform delay sampling is represented in Figure 2.10 and is a consequence

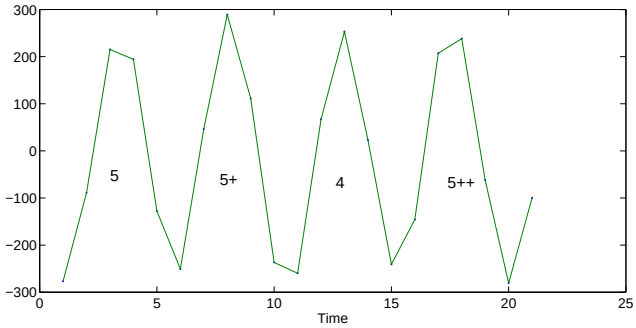

Figure 2.10: Illustration of the effect of non-uniform delay sampling: the number of sample points per fringe varies with scanning velocity.

of the voltage control loop controlling the velocity of the stage. The time between the sampled points is evenly spaced, as seen on the xaxis, but the number of points in each of the fringes varies, and therefore the delay values between the points, as the scanning velocity increases and decreases. The values of the group delay, τ, are obtained from

$$\tau = \frac{\phi(\tau)\lambda}{2\pi c} \tag{2.2.49}$$

The interferogram can then be resampled at uniform delay intervals by interpolation.

2.3 Summary and Context of Experimental Work

Fibre Bragg gratings are the most promising candidate for large scale implementation of fibre-optic sensors in the field of science and engineering known as structural health monitoring. Particular features of FBGs, such as the measurand being directly encoded in the wavelength of the light reflected from the grating and the ease of mul-

tiplexing, have already seen their implementation in a variety of structural monitoring applications.

Fourier transform spectroscopy, which is typically implemented on a Michelson interferometer, has a fundamental advantage over other interrogation techniques to interrogate over large wavelength ranges due to the Fellgett (or multiplex) advantage, as described in Section 2.1.16. However, mechanically scanned interferometers suffer from spectral degradation due to non uniform velocity of the scanning stages. One method for calibration of the delay in an interferometer is based on the mapping of the delay provided by a highly stable wavelength reference. This map is encoded in the temporal phase vector obtained via the Hilbert transform and has been applied to short delay scans. FTS, however, requires long-OPD scans to provide high resolution. This results in an accumulation of spectral content in the Fourier transform of an acquired interferogram.

The capability of mechanically scanned FTS interrogation units, where delay calibration is conducted via the HTT, to interrogate large arrays of gratings, providing quasi-distributed, simultaneous measurement of all the gratings in an array, and high resolution measurement of the intragrating spectral content, has not been addressed in the literature. The Hilbert transform technique, for delay calibration has been previously applied to scan lengths < 9 mm [121] on bulk-optic interferomters. The work reported in the later chapters of this thesis applies the Hilbert transform technique for calibration of the delay in an interferometer for scan lengths 25x those previously reported in the literature. A customised Fourier transform spectrometer is then applied to the demodulation of FBG arrays to provide high resolution measurement of the intra-grating spectral content. This spectrometer demonstrated measurement capability over a wavelength range of 900 nm.

The temporal phase vector obtained via the Hilbert transform method can also provide high resolution measurement of the mean wavelength reflected from a grating. The method is capable of providing high resolution wavelength measurement over far shorter OPD scans than achievable using FTS. This method and the Hilbert transform

technique for delay calibration have previously been applied to measurements made on bulk-optic interferometers. The capability and repeatability of the techniques when applied to all-fibre equivalents of the Michelson interferometer also needs to be assessed.

The Hilbert transform technique has also been demonstrated for measurement of the mean reflected wavelength from an array of FBGs, without measurement of the intra-grating spectral detail, providing higher resolution over shorter OPD scans (5 pm resolution for a 1.2 mm scan [117]) than conventional FTS. The work reported in chapter 6 applies this measurement technique to an all-fibre interferometric configuration.

References

[1] B. Culshaw, *Optical Fiber Sensors: Principles and Components*, vol. 1, ch. 2 Basic Concepts of Optical Fiber Sensors, pp. 9–24. Artech House, 1989. ISBN 0-89006-317-6.

[2] B. Culshaw and J. Dakin, eds., *Optical Fiber Sensors: Systems and Applications*, vol. 2. Artec House, 1989. ISBN 0-89006-376-1.

[3] E. Hecht, *Optics*. New York: Addison Wesley, 3rd ed., 1998.

[4] S. T. Vohra, *HandBook of Optical Fibre Sensing Technology: Optical Fibre Grating Applications*, ch. 23, pp. 475–504. John Wiley and Sons Ltd., 2002.

[5] J. Dakin, *Optical Fiber Sensors: Systems and Applications*, ch. 15 Distributed Optical Fiber Sensor Systems, pp. 575–598. Artech House, 1989.

[6] T. R. Parker, M. Farhadiroushan, V. A. Handerek, and A. J. Rogers, "A fully distributed simultaneous strain and temperature sensor using spontaneous Brillouin backscatter," *IEEE Photonics Technology Letters*, vol. 9, pp. 979–981, July 1997.

[7] H.-N. Li, D.-S. Li, and G.-B. Song, "Recent Applications of Fiber Optic Sensors to Health Monitoring in Civil Engineering," *Engineering Structures*, vol. 26, pp. 1647–1657, 2004.

[8] Y.-J. Rao, "In-fibre Bragg grating sensors," *Meas. Sci. Technol.*, vol. 8, pp. 355–375, 1997.

[9] A. Othonos, "Fibre Bragg Gratings," *Review of Scientific Instruments*, vol. 68, pp. 4309–4341, December 1997.

[10] A. D. Kersey, M. A. Davis, H. J. Patrick, M. LeBlanc, K. P. Koo, C. G. Askins, M. A. Putnam, and E. J. Friebele, "Fibre Grating Sensors," *Journal of Lightwave Technology*, vol. 15, no. 8, pp. 1442–1463, 1997.

[11] K. O. Hill and G. Meltz, "Fiber Bragg Grating Technology: Fundamentals and Overview," *Journal Of Lightwave Technology*, vol. 15, pp. 1263–1276, August 1997.

[12] B. Lee, "Review of the Present Status of Optical Fibre Sensors," *Optical Fibre Technology*, vol. 9, no. 2, pp. 57–59, 2003.

[13] G. Keiser, *Optical Fiber Communications.* Electrical and Electronic Engineering, Singapore: McGraw-Hill, 2nd ed., 1991. ISBN 0-07-100785-7.

[14] J. Wilson and J. Hawkes, *Optoelectronics: An Introduction.* Prentice Hall Europe, third edition ed., 1998.

[15] R. Kashyap, *Fibre Bragg Gratings.* Optics and Photonics, Academic Press, 1999.

[16] J. A. Buck, *Fundamentals of Optical Fibres.* New York: Wiley-Interscience, 1995. ISBN 0-471-30818-8.

[17] J. L. Arce-Diego, *HandBook of Optical Fibre Sensing Technology: Light and Waveguiding*, ch. 3, pp. 33–55. John Wiley and Sons Ltd., 2002.

[18] G. Lachs, *Fibre Optic Communications: Systems, Analysis and Enhancements.* McGraw-Hill, 1998, ISBN:0-07-038279-4.

[19] D. Gloge, "Weakly guiding fibers," *Applied Optics*, vol. 10, pp. 2252–2258, October 1971.

[20] A. W. Snyder and W. R. Young, "Modes of optical waveguides," *Journal of the Optical Society of America*, vol. 68, pp. 297–309, March 1978.

[21] J. Zubia and M. Lomer, *HandBook of Optical Fibre Sensing Technology: Optical Waveguides and their Manufacture*, ch. 4, pp. 57–79. John Wiley and Sons Ltd., 2002.

[22] J. Zubia and J. Arrue, "Plastic optical fibers: An introduction to their technological processes and applications," *Optical Fiber Technology*, vol. 7, pp. 101–140, 2001.

[23] D. Derickson, *Fibre Optic Test and Measurement.* Prentice Hall, 1998.

[24] M. Davis and A. Kersey, "Application of a Fibre Fourier Transform Spectrometer to the Detection of Wavelength Encoded Signals from Bragg Grating Sensors," *Journal of Lightwave Technology*, vol. 13, no. 7, pp. 1289–1295, 1995.

[25] I. Severin, R. E. Abdi, and M. Poulain, "Strength measurements of silica optical fibers under severe environment," *Optics and Laser Technology*, vol. 39, pp. 435–441, 2007.

[26] D. P. Hand and P. S. Russell, "Solitary Thermal Shock Waves and Optical Damage in Optical Fibres - The Fibre Fuse," *Optics Letters*, vol. 13, pp. 767–769, September 1988.

[27] K. Seo, N. Nishimura, and M. Shiino, "Evaluation of high-power endurance in optical fiber links," *Furukawa Review*, no. 24, pp. 17–22, 2003.

[28] R. M. Percival, E. S. R. Sikora, and R. Wyatt, "Catastrophic damage and accelerated ageing in bent fibres caused by high optical powers," *Electronics Letters*, vol. 36, pp. 414–416, March 2000.

[29] E. S. R. Sikora, D. J. McCartney, K. Farrow, and R. Davey, "Reduction in fibre reliability due to high optical power," *Electronics Letters*, vol. 39, pp. 1043–1044, July 2003.

[30] R. Willsch and W. Ecke, *HandBook of Optical Fibre Sensing Technology: Fibre and Integrated Optic Components for Sensing*, ch. 6, pp. 103–123. John Wiley and Sons Ltd., 2002.

[31] A. C. Garcia and J. E. Cuenca, *HandBook of Optical Fibre Sensing Technology: Transduction Techniques based on Intensity Modulation of Light*, ch. 11, pp. 209–226. John Wiley and Sons Ltd., 2002.

[32] J. D. Jones, *HandBook of Optical Fibre Sensing Technology: Interferometry and Polarimetry for Optical Sensing*, ch. 12, pp. 227–245. John Wiley and Sons Ltd., 2002.

[33] B. Culshaw, *HandBook of Optical Fibre Sensing Technology: Gas Spectroscopy Techniques for Optical Fibre Sensors*, ch. 13, pp. 247–270. John Wiley and Sons Ltd., 2002.

[34] D. C. Lee, J. J. Lee, I. B. Kwon, and D. C. Seo, "Monitoring of fatigue damage of composite structures by using embedded intensity-based optical fiber sensors," *Smart Materials and Structures*, vol. 10, no. 2, pp. 285–292, 2001.

[35] D. A. Jackson and J. D. C. Jones, *Optical Fiber Sensors: Systems and Applications*, vol. 2, ch. 10 Interferometers, pp. 329–380. Artech House, 1989.

[36] A. Bertholds and R. Dandliker, "Deformation of single-mode optical fibers under static longitudinal stress," *Journal of Lightwave Technology*, vol. 5, pp. 895–900, July 1988.

[37] A. Bertholds and R. Dandliker, "Determination of the individual strain-optic coefficients in single-mode optical fibers," *Journal of Lightwave Technology*, vol. 6, pp. 17–20, January 1988.

[38] B. Poumellec and F. Kherbouche, "The Photorefractive Bragg Gratings in the Fibers for Telecommunications," *Journal Physics III France*, vol. 6, pp. 1595–1624, December 1996.

[39] X. Bao, D. J. Webb, and D. A. Jackson, "Combined distributed temperature and strain sensor based on Brillouin loss in an optical fiber," *Optics Letters*, vol. 19, pp. 141–143, January 1994.

[40] J. D. C. Jones and W. N. MacPherson, *Handbook of Optical Fibre Sensing Technology: Discrimination Techniques for Optical Sensors*, ch. 19, pp. 403–420. John Wiley and Sons Ltd., 2002.

[41] S. Merlo, M. Norgia, and S. Donati, *HandBook of Optical Fibre Sensing Technology: Fiber Gyroscope Principles*, ch. 16, pp. 331–348. John Wiley and Sons Ltd., 2002.

[42] H. C. LeFevre, *Optical fiber Sensors: Systems and Applications*, vol. 2, ch. 11 Fiber Optic Gyroscope, pp. 381–429. Artec House, 1989.

[43] D. G. A. Pavlath, "Fiber optic gyros: The vision relaised," in *18th International Optical Fiber Sensors Conference Technical Digest*, no. MA3, (Washington, DC,), Optical Society of America, 2006. ISBN: 1Ą-55752Ą-817Ą-9.

[44] B. Culshaw, *Optical Fiber Sensors: Systems and Applications*, vol. 2, ch. 18: Applications of Fiber Optic Sensors in the Aerospace and Marine Industries, pp. 701–720. Artec House, 1989.

[45] R. B. Dyot, S. M. Bennet, D. Allen, and J. Brunner, "Development and commercialization of open loop fiber gyros at KVH industries (formerly at Andrews)," in *15th Optical Fiber Sensors Conference Technical Digest*, no. MA6, pp. 19–22, 2002.

[46] A. Ohno, A. Kurokawa, T. Kumagai, S. Nakamura, and K. Hotate, "Application and technical progress of fiber optic gyros in japan," in *18th International Optical Fiber Sensors Conference Technical Digest*, no. MA4, Optical Society of America, Washington DC., 2006.

[47] G. A. Cranch and P. J. Nash, "Large-scale multiplexing of interferometric fiber-optic sensors using TDM and DWDM," *Journal of Lightwave Technology*, vol. 19, pp. 687–699, May 2001.

[48] P. Nash, "Review of interferometric optical fibre hydrophone technology," in *IEE Proceedings Radar, Sonar and Navigation*, vol. 143, pp. 401–404, December 1996. ISSN: 1350-2395.

[49] K. O. Hill, Y. Fujii, D. C. Johnson, and B. S. Kawasaki, "Photosensitivity in Optical Waveguides: Application to Reflection Filter Fabrication.," *Applied Physics Letters*, vol. 32, pp. 647–649, May 1978.

[50] G. Meltz, W. W. Morey, and W. H. Glenn, "Formation of Bragg Gratings in Optical Fibres by a Transverse Holographic Method," *Optics Letters*, vol. 14, pp. 823–825, 1989.

[51] A. Martinez, M. D. I. Khrushchev, and I. Bennion, "Direct writing of fibre Bragg gratings by femtosecond laser," *Electronic Letters*, vol. 40, pp. 1170–1172, September 2004.

[52] Y. J. Rao, "Recent progress in applications of in-fibre Bragg grating sensors," *Optics and Lasers in Engineering*, vol. 31, pp. 297–324, 1999.

[53] L. Dong, J. L. Archambault, L. Reekie, P. S. J. Russell, and D. N. Payne, "Single pulse Bragg gratings written during fibre drawing," *Electronics Letters*, vol. 29, pp. 1577–1578, August 1993.

[54] P. Ferdinand and O. F. et al., "Mine Operating Accurate STABILity Control with Optical Fiber Sensing and Bragg Grating Technology: The European BRITE/EURAM STABILOS Project," *Journal of lightwave Technology*, vol. 13, pp. 1303–1313, July 1995.

[55] K. Schroeder, W. Ecke, J. Apitz, E. Lembke, and G. Lenschow, "A fibre Bragg grating sensor system monitors operational load in a wind turbine rotor blade," *Meas. Sci. Technology*, vol. 17, pp. 1167–1172, 2006.

[56] J. Seim, E. Udd, and W. Schulz, "Health monitoring of an oregon historical bridge with fibre grating strain sensors," *Proceedings SPIE*, vol. 3671, pp. 128–134, 1999.

[57] A. Quintela, C. Jauregui, J. Echevarria, and J. M. Lopez-Higeura, "Embedded temperature-strain fibre Bragg grating sensor system validation for concrete structures," *Journal of Optics A: Pure and Applied Optics*, vol. 4, pp. 387–390, November 2002.

[58] P. M. Nellen, A. Frank, R. Bronnimann, and U. Sennhauser., "Optical fibre Bragg gratings for tunnel surveillance," *Proceedings of SPIE*, vol. 3986, pp. 263–270, 2000.

[59] Y. Zhang, S. Li, B. Chen, and H. L. Cui, "Fiber-Bragg-Grating based seismic geophone for oils/gas prospecting," *Optical Engineering*, vol. 45, August 2006.

[60] F. Xie, X. Chen, L. Zhang, and M. Song, "Realisation of an effective dual parameter sensor employing a single fibre Bragg grating structure," *Optics and Lasers in Engineering*, vol. 44, pp. 1088–1095, 2006.

[61] M. G. Xu, J. L. Archambault, L. Reekie, and J. P. Dakin, "Discrimination between strain and temperature effects using dual wavelength fibre grating sensors," *Electronics Letters*, vol. 30, pp. 1085–1087, June 1994.

[62] S. W. James, M. L. Dockney, and R. P. Tatam, "Simultaneous independent temperature and strain measurement using in-fibre Bragg grating sensors," *Electronics Letters*, vol. 32, pp. 1133–1134, June 1996.

[63] M. G. Xu, L. Dong, L. Reekie, J. A. Tucknot, and J. L. Cruz, "Temperature independent strain sensor using a chirped Bragg grating in a tapered optical fibre," *Electronics Letters*, vol. 31, pp. 823–825, May 1995.

[64] M. Born and E. Wolf, *Principles of Optics*. Pergamon Press Ltd., 7th (expanded) ed., 1999.

[65] T. Erdogan, "Fiber Grating Spectra," *Journal of Lightwave Technology*, vol. 15, pp. 1277–1294, August 1997.

[66] W. Du, X. M. Tao, H. Y. Tam, and C. L. Choy, "Fundamentals and applications of optical fiber Bragg grating sensors to textile structural composites," *Composite Structures*, vol. 42, pp. 217–229, 1998.

[67] B. B. Wagreich and J. S. Sirkis, "Distinguishing Fibre Bragg Grating Strain Effects," in *OSA Technical Digest Series*, vol. 16, Optical Society of America, 1997.

[68] M. A. Davis, D. G. Bellmore, and A. D. Kersey, "Distributed fiber Bragg grating strain sensing in reinforced concrete structural components," *Cement and Concrete Composites*, vol. 19, pp. 45–47, 1997.

[69] R. M. Measures, S. Melle, and K. Liu, "Wavelength demodulated Bragg grating fiber optic sensing systems for addressing smart structure critical issues," *Smart Materials and Structures*, vol. 1, pp. 36–44, 1992.

[70] J. D. C. Jones, "Review of Fibre Sensor Techniques for Temperature-Strain Discrimination," in *Twelfth International Conference on Optical Fibre Sensors*, vol. 16 of OSA Technical Digest Series, pp. 36–39, OSA, 1997.

[71] M. LeBlanc, S. Y. Huang, M. Ohn, and R. M. Measures, "Distributed strain measurement based on a fiber Bragg grating and its reflection spectrum analysis," *Optics Letters*, vol. 21, pp. 1405–1407, September 1996.

[72] S. Huang, M. LeBlanc, M. M. Ohm, and R. M. Measures, "Bragg intragrating structural sensing," *Applied Optics*, vol. 34, no. 22, pp. 5003–5009, 1995.

[73] M. Douay, W. X. Xie, T. Taunay, P. Bernage, P. Niay, P. Cordier, B. Poumellec, L. Dong, J. F. Bayon, H. Poignant, and E. Delevaque, "Densification involved in the UV-based photosensitivity of silica glasses and optical fibers," *Journal of Lightwave Technology*, vol. 15, pp. 1329–1342, August 1997.

[74] W. W. Morey, "Bragg grating temperature and strain sensors," in *Proceedings of the 6th internation conference on Optical Fiber Sensors*, vol. 44, (Paris-France), pp. 526–531, 1989.

[75] J. Albert, K. O'Hill, B. Malo, S. Theriault, F. Bilodeau, D. C. Johnson, and L. E. Erickson, "Apodisation of the spectral response of fibre Bragg gratings using a phase mask with variable diffraction efficiency," *Electronics Letters*, vol. 31, pp. 222–223, February 1995.

[76] M. L. Dockney, S. W. James, and R. P. Tatam, "Fibre Bragg gratings fabricated using a wavelength tuneable laser source and a phase mask based interferometer," *Meas. Sci. Technology*, vol. 7, pp. 445–448, 1996.

[77] A. Dragomir and D. N. Nikogosyan, "Inscription of Fiber Bragg Gratings by Ultraviolet Femtosecond Laser Radiation," *Optics Letters*, vol. 28, pp. 2171–2173, November 2003.

[78] J. L. Archambault, L. Reekie, and P. S. J. Russell, "100reflectors produced in optical fibres by single eximer laser pulses," *Electronic Letters*, vol. 29, pp. 453–455, March 1993.

[79] N. H. Ky, H. G. Limberger, R. P. Salathe, F. Cochet, and L. Dong, "Uv-irradiation induced stress and index changes during the growth of type-I and type-IIA fiber gratings," *Optics Communications*, vol. 225, pp. 313–318, 2003.

[80] A. Othonos and K. Kalli, *Fiber Bragg Gratings: Fundamentals and Applications in Telecommunications and Sensing*. Artech House, 1999. ISBN: 0-89006-344-3.

[81] K. Kalli, A. G. Simpson, K. Zhou, L. Zhang, D. Birkin, T. Ellingham, and I. Bennion, "Spectral modification of type IA fibre Bragg gratings by high-power near-infrared lasers," *Meas. Sci. Technology*, vol. 17, pp. 968–974, 2006.

[82] D. W. Huang and C. C. Yang, "Reconstruction of fibre grating refractive index profiles from complex Bragg reflection spectra," *Applied Optics*, vol. 38, pp. 4494–4499, July 1999.

[83] K. Takada, H. Yamada, Y. Hibino, and S. Mitachi, "Range extension in optical low coherence reflectometry achieved by using a pair of retro-reflectors," *Electronics Letters*, vol. 31, pp. 1565–1567, August 1995.

[84] P. Lambelet and P. Y. Fonjallaz, "Bragg grating characterisation by optical low coherence reflectometry," *IEEE Photonics Technology Letters*, vol. 5, pp. 565–567, May 1993.

[85] P. M. Cavaleiro, F. M. Araujo, J. L. Santos, and F. Farahi, "Simultaneous measurement of strain and temperature using Bragg gratings written in Germanosilicate and Boron co-doped Germanosilicate fibers," *IEEE Photonics Technology Letters*, vol. 11, pp. 1635–1637, December 1999.

[86] J. K. Ranka, R. S. Windeler, and A. J. Stentz, "Visible continuum generation in air-silica microstructure optical fibres with anomalous dispersion at 800nm," *Optics Letters*, vol. 25, pp. 25–27, January 2000.

[87] A. K. Abeeluck and C. Headly, "High power supercontinuum generation in highly non-linear, dispersion shifted fibers by use of a continuous wave Raman fiber laser," *Optics Letters*, vol. 29, pp. 2163–2165, September 2004.

[88] A. D. Kersey and T. A. Berkoff, "Fiber-optic Bragg grating strain sensor with drift-compensated high-resolution interferometric wavelength-shift detection," *Optics Letters*, vol. 18, pp. 72–74, January 1993.

[89] L. A. Ferreira, E. V. Diatzikis, J. L. Santos, and F. Farahi, "Frequency modulated multimode laser diode for fibre Bragg grating sensors," *Journal of Lightwave Technology*, vol. 16, pp. 1620–1630, September 1998.

[90] Y. J. Rao, D. A. Jackson, L. Zhang, and I. Bennion, "Dual cavity interferometric wavelength-shift detection for in-fibre Bragg grating sensors," *Optics Letters*, vol. 21, pp. 1556–1558, October 1996.

[91] A. Ezbiri, S. E. Kanellopoulos, and V. A. Handerek, "High resolution instrumentation system for demodulation of Bragg grating aerospace sensors," *Optics Communications*, vol. 150, pp. 43–48, May 1998.

[92] G. P. Brady, S. Hope, A. B. L. Ribeiro, D. J. Webb, L. Reekie, J. L. Archambault, and D. A. Jackson, "Demultiplexing of fibre Bragg grating temperature and strain sensors," *Optics Communications*, vol. 111, pp. 51–54, September 1994.

[93] Y. J. Rao, D. J. Webb, D. A. Jackson, L. Zhang, and I. Bennion, "High-resolution, wavelength-division-multiplexed in-fibre Bragg grating sensor," *Electronics Letters*, vol. 32, pp. 924–926, May 1996.

[94] S. M. Melle, K. Liu, and R. M. Measures, "A passive wavelength demodulation system for guided wave Bragg grating sensors," *IEEE Photonics Technology Letters*, vol. 4, pp. 516–518, May 1992.

[95] S.-C. Ye, S. E. Staines, S. W. James, and R. P. Tatum, "A polarization maintaining fibre Bragg grating interrogation system for multi-axis strain sensing," *Meas. Sci. Technology*, vol. 13, pp. 1446–1449, 2002.

[96] C. Boulet, D. J. Webb, M. Douay, and P. Niay, "Simultaneous interrogation of fiber Bragg gratings using an acousto-optic tunable filter," *IEEE Photonics Technology Letters*, vol. 13, pp. 1215–1217, November 2001.

[97] M. G. Xu, H. Geiger, J. L. Archembault, L. Reekie, and J. P. Dakin, "Novel interrogating system for fibre Bragg grating sensors using an acousto-optic tunable filter," *Electronics Letters*, vol. 29, pp. 1510–1511, August 1993.

[98] K. Peters, P. Pattis, J. Botsis, and P. Giaccari, "Experimental verification of response of embedded optical fiber Bragg grating sensors in non-homogeneous strain fields," *Opticas and Lasers in Engineering*, vol. 33, pp. 107–109, 2000.

[99] A. Arie, B. Lissak, and M. Tur, "Static fiber Bragg grating strain sensing using frequency locked lasers," *Journal of Lightwave Technology*, vol. 17, pp. 1849–1855, October 1999.

[100] Y.-J. Rao, D. J. Webb, D. A. Jackson, L. Zhang, and I. Bennion, "In fiber Bragg grating temperature sensor system for medical applications," *Journal of Lightwave Technology*, vol. 15, pp. 779–785, May 1997.

[101] R. Williams, *Spectroscopy and the Fourier Transform: An Interactive Tutorial*. VCH Publishers, Inc., 1996.

[102] Y. Sano and T. Yoshino, "Fast optical wavelength interrogator employing arrayed waveguide grating for distributed fiber Bragg grating sensors," *Journal of Lightwave Technology*, vol. 21, pp. 132–139, January 2003.

[103] H. G. Gadiyar and R. Padma, "Ramanujan-Fourier series, the Wiener-Khintchine formula and the distribution of prime pairs," *Physica A*, vol. 269, pp. 503–510, 1999.

[104] D. A. Flavin, R. McBride, and J. D. C. Jones, "Interferometric fiber-optic sensing based on the modulation of group delay and first order dispersion: Application to strain-temperature measurand," *Journal of Lightwave Technology*, vol. 13, pp. 1314–1323, July 1995.

[105] D. W. Stowe, D. R. Moore, and R. G. Priest, "Polarization fading in fiber interferometric sensors," *IEEE Journal of Quantum Electronics*, vol. 18, no. 10, pp. 1644–1647, 1982.

[106] W. H. Steel, *Interferometry*. Cambridge Studies in Modern Optics, Cambridge University Press, 2 ed., 1983. ISBN: 0 521 25320 4.

[107] L. Lepetit, G. Cheriaux, and M. Joffre, "Linear techniques of phase measurement by femtosecond spectral interferometry for applications in spectroscopy," *J. Opt. Soc. Am. B*, vol. 12, pp. 2467–2474, December 1995.

[108] L. R. Jaroszewicz and M. A. Kojdecki, "New description of interference in fibre optic including coherence and polarisation," in *Proceedings SPIE: Interferometric Fiber Sensing*, vol. 2341, pp. 60–65, 1994.

[109] H. Yoshimura and T. Asakura, "Spatial Coherence Properties of Light from Optical Fibres," *Optical and Quantum Electronics*, vol. 24, pp. 631–646, 1992.

[110] H. L. An, X. Z. Lin, E. Y. B. Pun, and H. D. Liu, "Multi-wavelength operation of an erbium doped fibre ring laser using a dual pass Mach-Zehnder comb filter," *Optics Communications*, vol. 169, pp. 159–165, October 1999.

[111] J. T. Ahn, H. K. Lee, M.-Y. Jeon, D. S. Lim, and K. H. Kim, "Continuously tunable multiwavelength transmission filter based on stabilised fibre-optic interferometer," *Optics Communications*, vol. 165, pp. 33–37, July 1999.

[112] H.-K. Teng, C.-N. Chang, and K.-C. Lang, "Determination of path length difference by low coherence interference spectrum," *Optics and Lasers in Engineering*, vol. 42, pp. 437–446, 2004.

[113] S. Calvez, X. Rejeaunier, P. Mollier, J.-P. Goedgebuer, and W. T. Rhodes, "Erbium doped fiber laser tuning using two cascaded unbalanced Mach-Zehnder interferometers as intracavity filter: Numerical analysis and experimental confirmation," *Journal of Lightwave Technology*, vol. 19, pp. 893–898, June 2001.

[114] S. D. Dyer, P. A. Williams, R. J. Espejo, J. D. Kofler, and S. M. Etzel, "Fundamental limits in fiber Bragg grating peak wavelength measurements," in *Proceedings of SPIE* (M. Voet, R. Willsch, W. Ecke, J. Jones, and B. Culshaw, eds.), vol. 5855, (Bellingham, WA.), pp. 88–93, SPIE, 2005.

[115] G. M. Flockhart, R. R. J. Maier, J. S. Barton, W. N. MacPherson, J. D. C. Jones, K. E. Chisholm, L. Zhang, I. Bennion, I. Read, and P. D. Foote, "Quadratic behaviour

of fibre Bragg grating temperature coefficients," *Applied Optics*, vol. 43, no. 13, pp. 2744–2751, 2004.

[116] D. A. Flavin, R. McBride, and J. D. C. Jones, "Short Optical Path Scan Interferometric Interrogation of a Fibre Bragg Grating Embedded in a Composite," *Electronic Letters*, vol. 33, 1997.

[117] D. Flavin, R. McBride, and J. D. C. Jones, "Short-Scan Interferometric Interrogation and Multiplexing of Fibre Bragg Grating Sensors," *Optics Communications*, vol. 170, no. 4-6, pp. 347–353, 1999.

[118] S. L. Hann, *Hilbert Transforms in Signal Processing*. No. ISBN: 0-89006-886-0, Artec House, 1996.

[119] R. N. Bracewell, *The Fourier Transform and its Applications*. McGraw-Hill, 3rd ed., 2000. ISBN 0-07-303938-1.

[120] D. Pines and L. Salvino, "Structural health monitoring using empirical mode decomposition and the Hilbert phase," *Journal of Sound and Vibration*, vol. 294, no. 1-2, pp. 97–124, 2006.

[121] J. H. Rothwell and D. A. Flavin, "Dispersion Measurement by White Light Interferometry Based on Fresnel Reflections," in *CLEO-Europe*, (Munich, Germany), 2002.

Chapter 3

Implications of high power losses in IR femtosecond laser-inscribed fibre Bragg gratings

3.1 Introduction

Failure analysis and prevention are important stages in all engineering disciplines. Structural failures are generally initiated by fatigue in the constituent materials. At present, this is predominantly monitored by visual inspection, at which stage prevention is not an option as the damage has already occurred. Structural health monitoring, implemented using fibre optic sensors, offers the potential for early identification of the potential causes of material fatigue in structures. This, therefore, possibly introduces a window for failure prevention [1].

Fibre Bragg grating sensors are considered the most promising candidate for implementation of fibre-optic sensors [2]. They are versatile fibre-optic components, and have been applied in various capacities in the sensing and telecommunications fields as described in Section 2.1.10. However, the components themselves also require failure analysis and prevention stages in their development. Failure of FBGs, regardless of application, can affect the entire system in which they are applied.

This chapter presents observations on temperature increases and subsequent failure of near-infrared (NIR) femtosecond laser-inscribed FBGs when subjected to high powers. These observations were made while conducting experiments on the application of FBGs in a sensing capacity. The aim of the experiments were to profile the

temperature threshold for damage to occur to fibres in tight bend situations when subjected to high optical powers. This necessitated the use of NIR femtosecond-laser inscribed gratings, as there is no requirement for stripping of the buffer in the inscription process, leaving an intact fibre with which to establish the point at which catastrophic damage occurs to the fibre.

The work was carried out in Aston University, Birmingham, UK. The Photonics Research Group in the School of Engineering and Applied Sciences at Aston has a proven track record in fibre optic sensors. The group is an acknowledged centre of excellence in the inscription and characterisation of fibre Bragg gratings and was among the first to report the NIR femtosecond laser inscription of gratings [3].

The drift compensated high resolution interferometric wavelength shift detection technique developed by Kersey *et al.* [4] was applied to grating demodulation. The wavelength shift experienced by a grating, when exposed to high optical powers, was also recorded on an Optical Spectrum Analyser (OSA) for comparison.

3.1.1 Fibre Reliability

The requirement for higher bandwidths in telecommunications applications has seen the development of higher power Erbium doped [5] and Raman amplifiers [6]. This requires that components of systems using such amplifiers have to be able to withstand high power operation (> 1 W), which in single mode fibres (mode field diameter ~ 10 μm) gives an intensity of 2 MW/cm^2 (300 times greater than that at the surface of the sun) [7].

Damage to fibres has been observed when used in high power applications; for example, the fibre fuse phenomenon [8] has been observed with measurement of the threshold for fibre fuse to occur [9], the effects of end-face damage under high powers [9], and for damage to occur to the fibre coating [10]. The fibre coating damage can be caused by light leaking from the fibre when it is broken or bent in a high power environment, as occurs with the introduction of Raman amplifier pump lasers. This light generates heat and can possibly ignite the buffer [11]. Spectral modification of

UV inscribed type IA FBGs has also been reported by Kalli *et al.* [12] where the resonant wavelength of the grating experiences a shift when exposed to high powers.

3.1.2 Fibre Bragg Gratings

In-fibre Bragg gratings (FBGs) have been one of the most exciting developments in the telecommunications and optical sensing fields in recent years. In the optical sensing field they have proved to be one of the most promising candidates for use as embedded sensors in fibre-optic smart structures [1]. The measured quantity is the peak reflective wavelength, λ_B, of the grating which changes as the grating is subjected to strain or temperature according to [13]

$$\Delta\lambda_B = 2n\Lambda\left(\left[1 - \frac{n^2}{2}\{P_{12} - \nu(P_{11} + P_{12})\}\right]\varepsilon + [\alpha + \xi]\,\Delta T\right) \tag{2.1.63}$$

where ε is the applied strain, $P_{i,j}$ are the coefficients of the strain-optic tensor, ν is the Poisson ratio, α is the coefficient of thermal expansion of the fibre and ξ is the thermo-optic coefficient as described in Section 2.1.12.

In the telecommunications field, FBGs have been used for applications such as wavelength division multiplexing, narrow band tunable filters and for dispersion compensation [14]. Ideally for such applications, the temperature sensitivity of the gratings needs to be mitigated and can be nearly eliminated by embedding the grating in another substance [15]. The resonant wavelength's stability when used in high power applications, where an increase in temperature is not due to external environmental influences, cannot be compensated for in such a manner and assumes a greater significance.

3.1.3 FBG Inscription

The principal mechanism involved in the inscription process of standard fibre Bragg gratings is the photosensitivity of Ge-doped fibre to UV light [16]. Reliability issues are a concern for UV inscribed FBGs, unless inscribed during fibre drawing [17]. In the

writing process, there is a requirement that the buffer is stripped from the fibre, because of a sensitivity to UV light. This can result in surface strength degradation, the extent of which depends on the stripping mechanism used. Hydrogen loading to increase the photosensitivity of the fibres has also been shown to decrease mechanical strength [18]. This reduction in the mechanical strength of the fibre due to UV inscription processes renders standard UV gratings unsuitable for reliability testing of fibres.

The development of near infrared point-by-point inscription techniques for FBGs by femtosecond laser pulses has eliminated the requirement for, not only stripping off the buffer coating, but also the need for a phase mask and photosensitised fibre [3]. There is, therefore, the potential for this writing technique to significantly reduce grating production time. Femtosecond laser inscribed gratings also exhibit characteristics such as high thermal stability, large refractive index modulation and confinement of the grating within a fraction of the fibre core [3]. However, as with inscription of gratings by UV light, there are also reliability issues which need to be addressed. The refractive index changes induced when inscribing FBGs with an IR femtosecond laser are thought to be due to a densification of the irradiated region [19]. The experimental work reported in the following sections presents observations relating to the endurance of fibre which has been subjected to this type of damage. These observations have implications for the ability of the fibre to operate normally under conditions where it has been damaged and subsequently subjected to high powers.

3.2 Experimental Motivation and Objectives

The original aim of the experimental work reported in this chapter was to measure the temperature threshold for damage to occur in optical fibres when subjected to a variety of tight bend situations as reported by Percival *et al.* [10] and Sikora *et al.* [11] at the British Telecom (BT) Advanced Communications Technology Centre, Ipswich, UK. In their observations, they reported that catastrophic damage to fibres could occur at optical powers as low as 0.5 W and that the melting temperature of silica ($> 1100^{o}C$)

was reached at the bend location. The temperature increases are caused by the power lost at the bend being absorbed by the coating, eventually causing a runaway effect.

To facilitate measurement of the runaway temperature increase reported by Sikora *et al.*, NIR femtosecond laser inscribed gratings were inscribed in a series of BT grade fibre and standard 1550 nm single-mode (smf-28) fibres for comparison. The fibres containing these gratings were installed in both the sensing and reference arms of an interferometric demodulation configuration, as reported by Kersey *et al.* [4]. The fibres were then to be subjected to different bend radii at the grating location and exposed to varying power levels, with the interrogation unit providing high speed and high resolution measurement of the change in temperature recorded by the sensing grating.

However, prior to conducting bend tests on the fibres, phase changes between the two signals from the sensing and reference arms of the demodulator were recorded by the lock-in amplifier when the sensing grating was subjected to high powers from a Raman laser. These phase changes (wavelength shifts), obtained by purely optical means, would invalidate measurements on the temperature increases made at bend locations in the fibre. A preliminary test of the wavelength shift of the gratings when subjected to high powers, ~4.5 W, resulted in the buffer melting off the fibre. The experimental configuration, constructed for profiling the temperature increases at bend locations, was then applied to profiling the temperature increases due to the gratings themselves.

3.3 Experimental Configuration

Two experimental configurations were used to record the effects of high power Raman pump lasers on the NIR femtosecond inscribed FBGs. Results obtained using the original interrogation technique (Mach-Zehnder interferometer), reported melting of the buffer at a temperature of ~ 98 ^{o}C in one case, while another grating reported a temperature increase of ~ 160 ^{o}C without any observable damage to the buffer.

These results suggested that the grating, at the buffer melting point, was being chirped and reflecting at multiple wavelengths. The phase comparison interrogation

scheme employed could not demodulate more than a single wavelength shift. This necessitated the use of a demodulator allowing interrogation over broad wavelength ranges. An Anritsu optical spectrum analyser (OSA) (model no. MS9717A) was used as the interrogation unit.

3.3.1 Mach Zehnder Interferometer

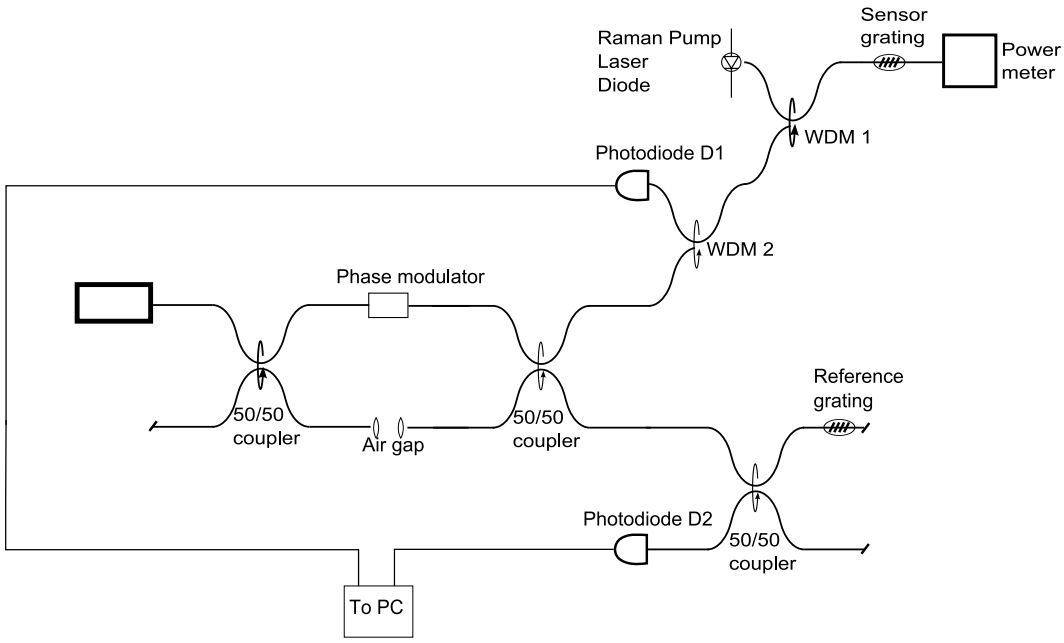

Figure 3.1: Experimental configuration: The output from a Mach-Zehnder interferometer illuminates the sensing and reference gratings for comparison by the lock-in amplifier.

In the experimental configuration in Figure 3.1, an unbalanced Mach-Zehnder interferometer (MZI) is illuminated by a 1550 nm broadband source. In a standard unbalanced Mach Zehnder interferometer (UMZI), a fixed time delay is introduced into one arm of the interferometer. The signal detected at the output of the interferometer [20] is given by

$$I = I_0[1 \ - \ V \ \ Cos(\phi_a - \phi_b)] \tag{2.2.27}$$

where where V is the visibility, ϕ_a and ϕ_b are the phase retardance of the signal and reference arms respectively and I_0 is the source intensity. The phase difference between the the two arms results in spectral fringes whose period is inversely proportional to

the optical path difference between the two beams [21]. The free spectral range was defined in chapter 2.2.8 as

$$FSR = \frac{\lambda^2}{\Delta_{OPD}} \tag{2.2.31}$$

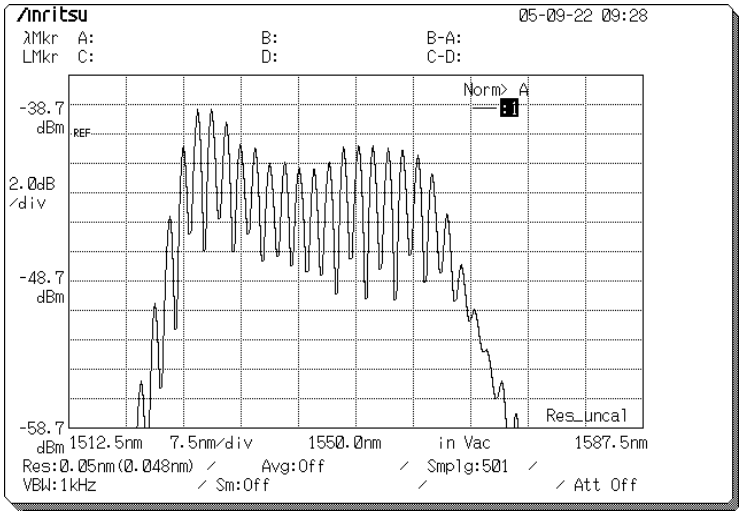

Figure 3.2: Output from a Mach-Zehnder interferometer illuminated by a broadband source and recorded by an Optical Spectrum Analyser.

The output of the UMZI, as captured by an OSA, is shown in Figure 3.2. The interference fringes along the spectral width of the source are clearly visible and the FSR of the interferometer, set to ~2 nm, can easily be determined from the wavelength of the fringes. The coherence length of the gratings is determined from the linewidth of the grating. If the OPD is shorter than the coherence length of the grating, the free spectral range of the interferometer will be greater than the grating linewidth and a sinusoidal signal will be reflected by the grating, as depicted in Figure 3.3. As the interferometer is scanned through its FSR, a signal of varying amplitude is reflected by the gratings to produce a sinusoidal signal at the detector. The amplitude of the reflected signal is dependent on the linewidth of the grating and the FSR of the interferometer. The sensing and reference Bragg gratings (Figure 3.1) each reflect a component of the interferometer output.

One arm of the interferometer contains a $LiNbO_3$ phase modulator. The second arm contains an air gap with which the non-zero optical path difference (OPD) be-

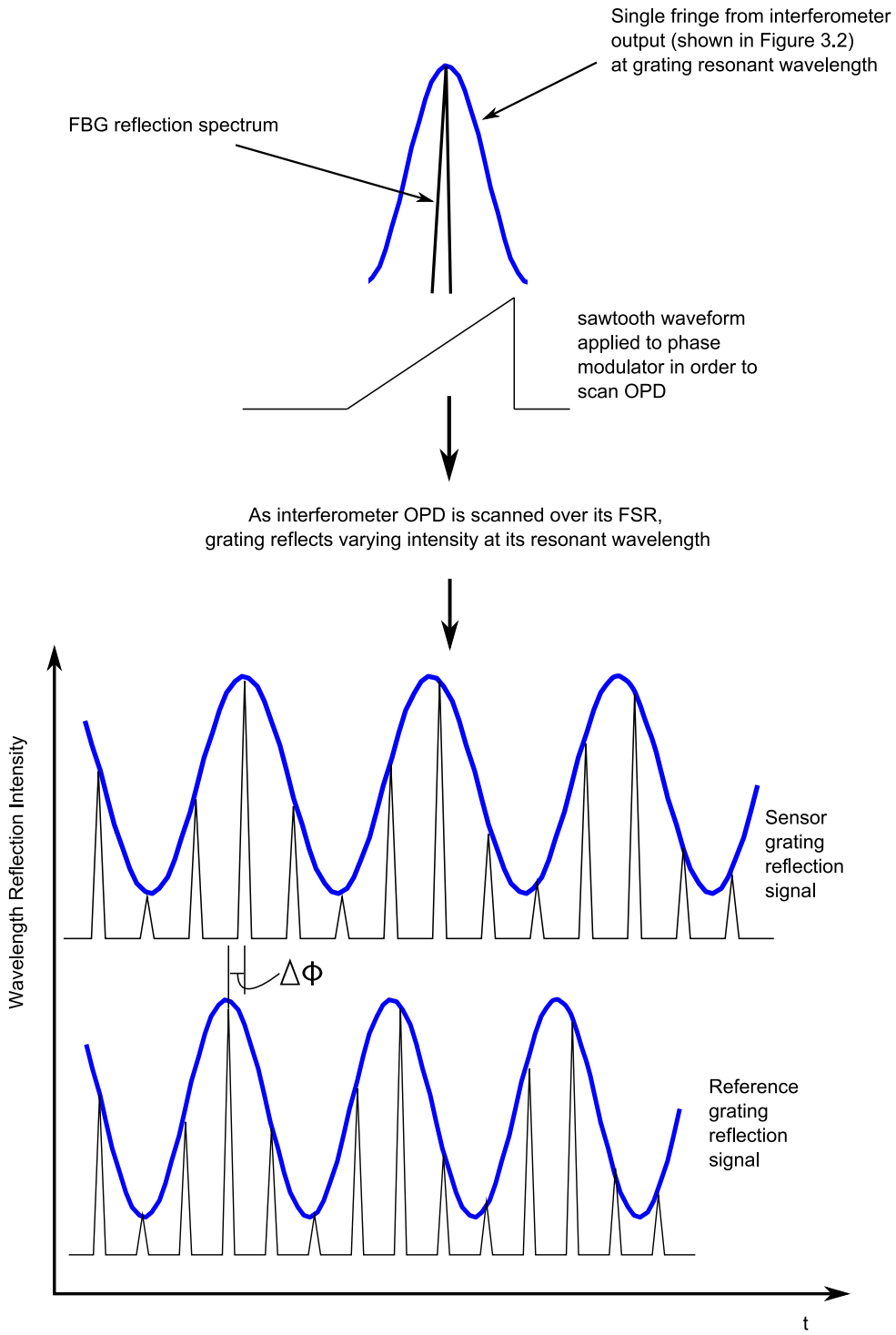

Figure 3.3: Illustration of output from Mach-Zehnder interferometer as the OPD is scanned through its FSR.

tween the two arms of the interferometer can be adjusted. By adjusting the path difference in the arms of the interferometer, the FSR of the MZI can be adjusted. The free spectral range of the interferometer was set to ~2 nm, giving an OPD in the interferometer of ~1.2 mm. The interferometer is repeatedly scanned over its FSR by applying a serrodyne (sawtooth) waveform to the phase modulator.

The sensing grating is connected to one of the output arms of the interferometer via 2 add/drop multiplexers, the first of which allows detection of the reflected signal from the grating at detector D1 and the second allows injection of light from the high power Raman laser. A reference grating is connected to the second output arm of the interferometer via a 50/50 coupler to allow detection of the reflected signal at detector D2. If the optical path imbalance between the arms of the interferometer is shorter than the coherence length of the gratings, a sinusoidal signal will be reflected from the gratings. The wavelength of the sensing grating is ~1549 nm. The component of the interferogram, generated by the UMZI, which is reflected by an FBG can be represented as a sinusoidally varying signal. A strain induced change in the reflected wavelength, $\delta\lambda$, manifests itself as a change in phase, $d\psi$, of this reflected signal, given by [4]

$$d\psi = -\frac{2\pi nd}{\lambda^2} d\lambda \tag{3.3.1}$$

where nd is the optical path difference in the interferometer. This allows a temperature induced phase change to be written as

$$\delta\psi = -\frac{2\pi nd}{\lambda} \xi \delta T \tag{3.3.2}$$

where δT is the change in temperature of the grating and ξ is the normalised temperature to wavelength shift responsivity of the grating [22]. ξ is defined as

$$\xi = \frac{1}{\lambda} \frac{\delta\lambda}{\delta T} \tag{3.3.3}$$

yielding a value of 6.67 x 10^{-6} /°C. Therefore, the temperature to phase shift response

in this case is ~1.6 deg / ^{o}C and the temperature to wavelength shift response is ~ 10.3 pm /^{o}C.

A measurand induced change in the reflective wavelength of the sensing grating induces a change in phase of the reflected signal. Both sensing and reference signals from the gratings are captured at photodiodes D1 and D2 respectively and are monitored using a lock-in amplifier to detect any phase change between the two gratings which is then recorded on a PC.

A series of femtosecond inscribed Bragg gratings were tested for damage when high power is transmitted down the fibre by replacing the sensing grating with a series of femtosecond inscribed gratings of varying lengths and reflectivities.

3.3.2 Optical Spectrum Analyser

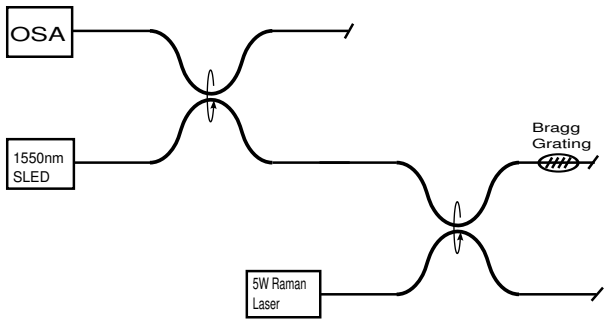

Figure 3.4: Demodulation by OSA

In Section 2.1.12, the contribution of a non-uniform measurand to the reflection spectrum of a grating was related to the periodicity of the refractive index modulation [23] by

$$\lambda_z = 2n(z)\Lambda(z) \tag{2.1.69}$$

where each section of the grating can contribute its own wavelength component to the reflection spectrum depending on the periodicity of the refractive index modulation.

The configuration illustrated in Figure 3.1 uses a lock-in amplifier to lock to a mean phase component of the sensor and reference signals and therefore is not suitable for measurement of multiple reflection peaks from the grating.

The second configuration used to demodulate the gratings is illustrated in Figure 3.4. Light from a 1550 nm SLED is launched through 2 x 50/50 couplers. The Raman pump laser is launched through the input arm of the second coupler. A femtosecond inscribed Bragg grating is spliced to the output arm of this coupler and the component of light from the 1550 nm SLED which is reflected by the grating propagates back through the two couplers and is detected by the OSA. The Raman laser power is increased from 0 - 4.5 W and the wavelength shift due to temperature increases experienced by the grating is recorded by the OSA. The OSA was set to a resolution of 0.05 nm, with a total measurement range of 6.3 nm.

3.4 Results and Discussion

3.4.1 Interferometric Analysis

Insertion Losses

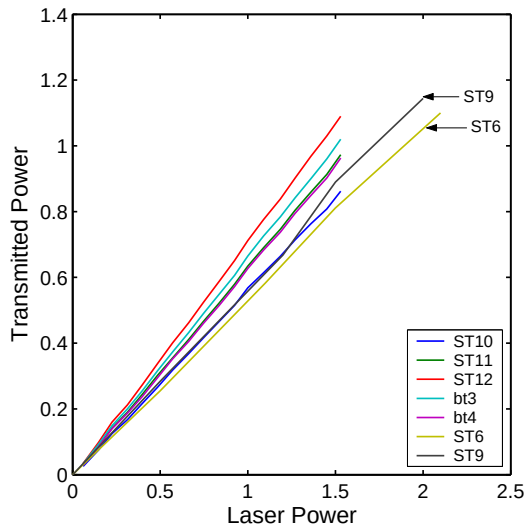

Figure 3.5: Transmitted power versus applied power for 7 different gratings measured at the Raman laser output of 1455 nm as the power levels are increased to ~ 1.5 - 2 W

Figure 3.5 displays the transmitted power through 5 NIR inscribed gratings as a function of applied power. The insertion losses for the 5 femtosecond laser inscribed gratings, three written in standard fibre (ST) and two written in BT telecom fibre (BT), were measured at the Raman laser output of 1455 nm using a power meter spliced to the sensing arm of the experimental configuration illustrated in Figure 3.1. The insertion losses for the range of gratings vary significantly, from ~ 1.5 - ~ 3 dB.

Temperature Increases

A simple temperature calibration of the gratings, conducted by immersing the individual gratings in a bath of water at room temperature and heating to ~ 100°C, gave a temperature to phase shift of ~ 1.7° /°C. The temperature of the water in the bath was monitored using two thermocouples. When the rms noise value in the signal (0.19°) is taken into account, this value is in close agreement with the value of 1.6° determined earlier. The results for two of the gratings, ST9 and ST10, are illustrated in Figure 3.6. The flattening off at both ends of the scans occurs just before heat was imparted to the system at room temperature and a reduction in the temperature increase as the water reached 100 °C.

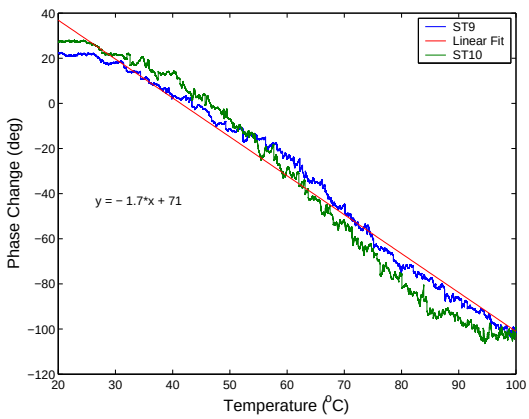

Figure 3.6: Phase change recorded by two gratings when subjected to temperature increases from room temperature to ~ 100°C. The slope of a linear fit to the ST10 data gives the change in phase per °C

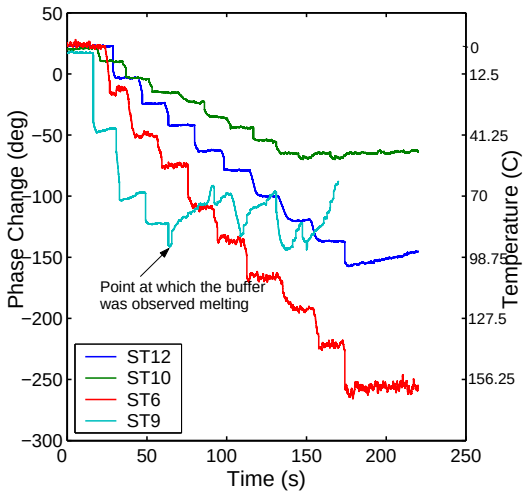

Figure 3.7: Phase change and corresponding temperature change recorded for 4 gratings at high powers.

The phase change between the signal and reference gratings is plotted for 4 gratings subjected to laser powers of 0 – 4.5 W (Figure 3.7). The laser power was incrementally increased in steps of 0.5 W. The approximate change in temperature recorded by individual gratings is plotted on the right hand axis ranging from 43 $^{\circ}C$ to 162 $^{\circ}C$ (-70 to -260° phase change) at 4.5 W.

The specifications for the gratings illustrated in Figure 3.7 were

Grating	Length	Reflectivity
ST6	>10 mm	3.5 dB
ST9	10 mm	8 dB
ST10	5 mm	8 dB
ST12	5.5 mm	5 dB

Inspection of the data for ST10, which exhibited a similar insertion loss to ST9 (Figure 3.5), exhibits the lowest temperature increase (Figure 3.7). This result could be caused by the location of the grating in the fibre core. The typical spot size of the inscribing NIR beam is ~ 3 μm, allowing positioning of the grating in the core.

ST6, the longest grating, but which had one of the lowest reflectivities, exhibited the largest observed phase change of ~ 260 °C at 4.5 W without the buffer melting off

the fibre. This phase change corresponds to a temperature increase of ~ 162 °C at a temperature to phase shift response of ~ 1.6 deg /°C.

ST9, the second longest grating, but with one of the highest reflectivities had an apparent buffer melting point of ~ 98 °C. The apparently low temperature recorded for the melting point of the buffer, in comparison to the temperature reached by grating ST6, where the buffer did not melt off the fibre, suggested that the experimental configuration above was not recording the actual change in temperature experienced by the grating. After melting of the buffer, the power levels that grating ST9 was exposed to were continually incremented to a power level of 4.5 W. These increments can be seen in the apparent temperature increases recorded by the grating after melting (Figure 3.7). However, after removal of the insulating effects of the buffer, the increased temperature levels gradually start to decay though the power levels remain constant.

Damage

To assess possible damage to the grating at high powers, the power levels to which the fibre was exposed in the earlier tests were individually switched on and then off. The wavelength at which the grating started and returned to was then recorded. Inspection of Figure 3.8 shows that BT2 returned to its original wavelength after exposure to power levels from 0 - 4.5 W. Similar tests on the gratings whose buffers did not melt off indicated the same result, i.e. they all returned to their original wavelengths. However, examination of the full scan recorded for $ST9$ (Figure 3.9) shows that there was a change between the recorded starting and finishing phase difference. In this case the buffer appeared to strip off at ~ 98 °C. The 29° change in phase equates to a 0.1 nm change in the original wavelength.

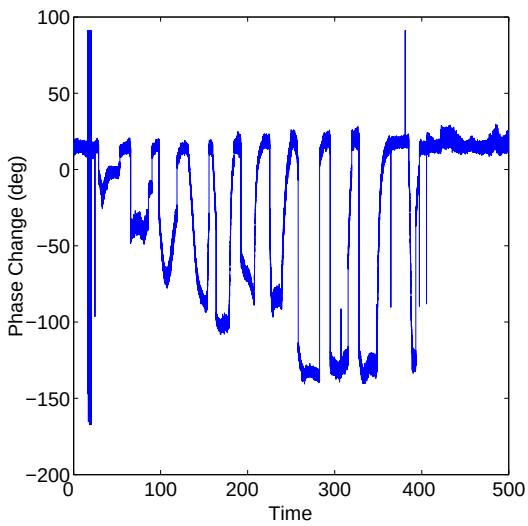

Figure 3.8: Phase change of grating BT2 with increase in laser power from 0 to 4.5W

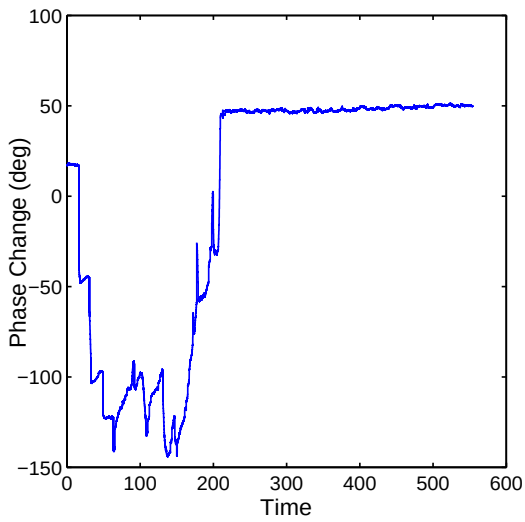

Figure 3.9: Phase change of grating ST9 with increase in laser power from 0 to 4.5W

3.4.2 OSA Observations

Spectral Broadening

Figure 3.10 illustrates the wavelength shift experienced by a NIR femtosecond laser inscribed FBG as the power levels in the fibre due to a 1455 nm Raman pump laser is increased from 0-4.5W.

The spectrum of the grating is clearly being broadened as the laser power levels launched through the fibre are increased. The peak reflected wavelength of the grating exhibits a shift of ~ 250 pm for exposure to 1 W Raman pump power. At a power level of 4.5 W the grating spectrum broadens to ~ 3.15 nm, which corresponds to an approximate temperature change of 315 °C.

This chirp, or broadening of the spectrum, resulted in a degradation of the signal being returned from the grating and subsequently recorded by the photodiode. As the chirp bandwidth approached the free spectral range of the interferometer (~ 2 nm) the grating was reflecting close to the full period of the sinusoidal signal from the interferometer. In addition, the lock-in amplifier, designed to lock in on the component closest to the reference signal, could not measure the chirp in the grating spectrum.

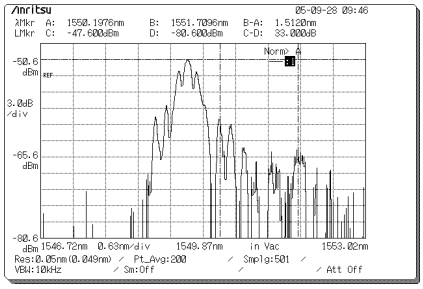

(0W)

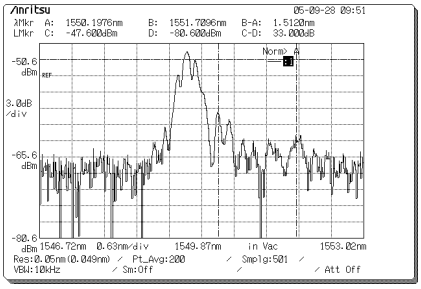

(0.5W)

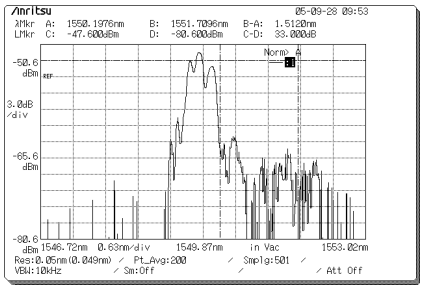

(1W)

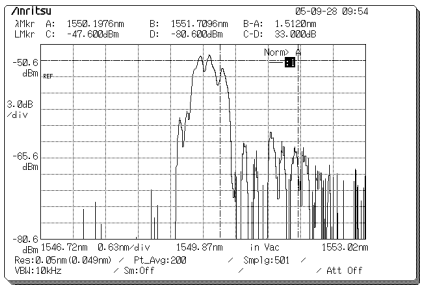

(1.5W)

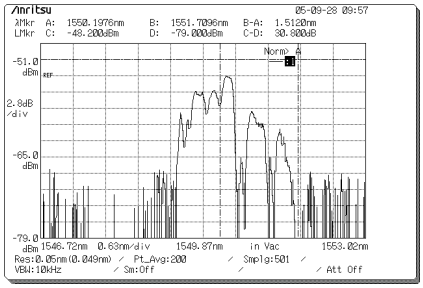

(2W)

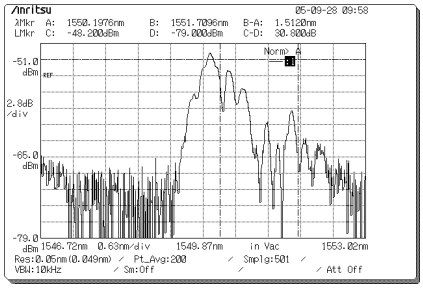

(2.5W)

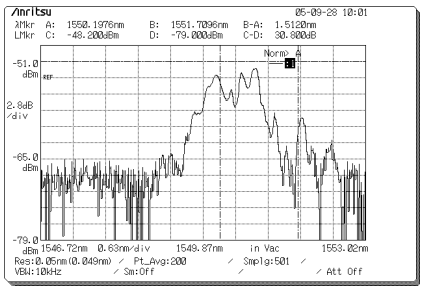

(3W)

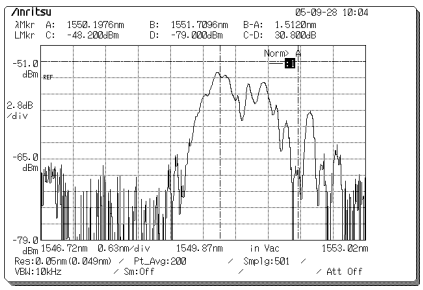

(3.5W)

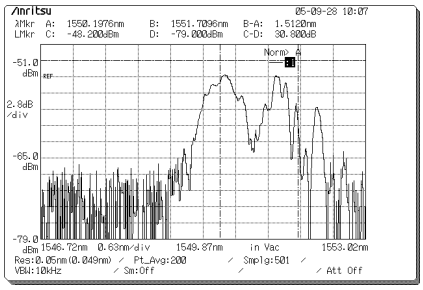

(4W)

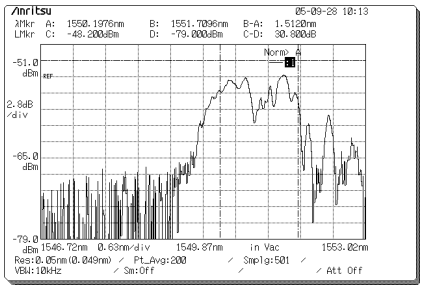

(4.5W)

Figure 3.10: Spectrum of a NIR femtosecond laser inscribed grating being chirped when power levels in the fibre are increased from 0- 4.5W

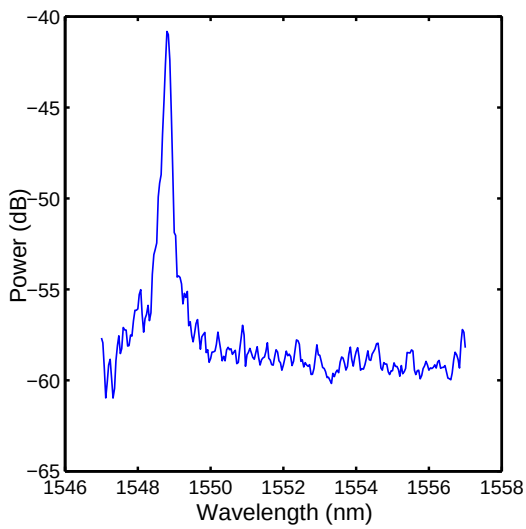

Figure 3.11: Grating spectrum with 0 W Raman power launched down fibre.

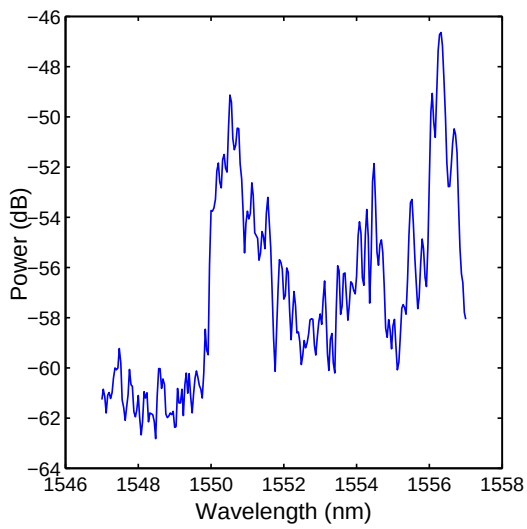

Figure 3.12: Spectrum recorded by OSA at buffer melting point of 2.5 W

Examination of another grating with similar specifications to ST9, using the OSA clearly shows broadening of the spectrum as the laser power level through the fibre is increased. Figure 3.11 illustrates the spectrum for a grating with the Raman laser switched off. Figure 3.12 shows the spectrum of this grating with 2.5 W of Raman laser power launched through the fibre. At this power level the buffer had already melted off the fibre around this grating.

The wavelength shift of the spectrum of the grating, due to the temperature increase at melting point, is more significant than that recorded using the interferometric configuration . The spectral broadening observed for this grating extends over ~ 7 nm; this is far beyond the FSR of the interrogating interferometer and hence the data produced by that system is not reliable. A wavelength shift of ~ 7 nm, at a sensitivity of ~ 11 pm /°C would correspond to an apparent temperature increase of ~ 540 °C, certainly more than enough to melt the buffer coating.

Damage

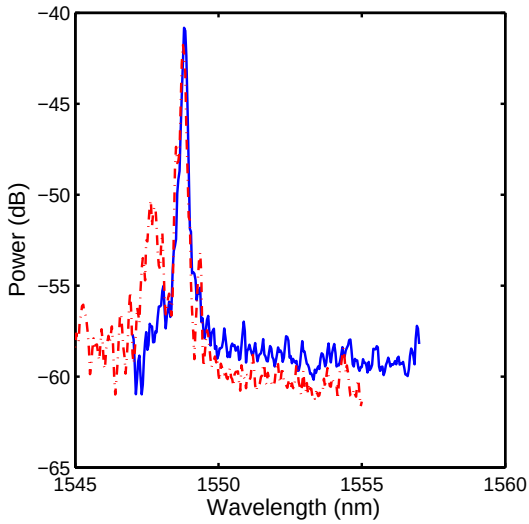

Figure 3.13: Comparison of spectra (no power) before (—) and after (-·-) melting of buffer

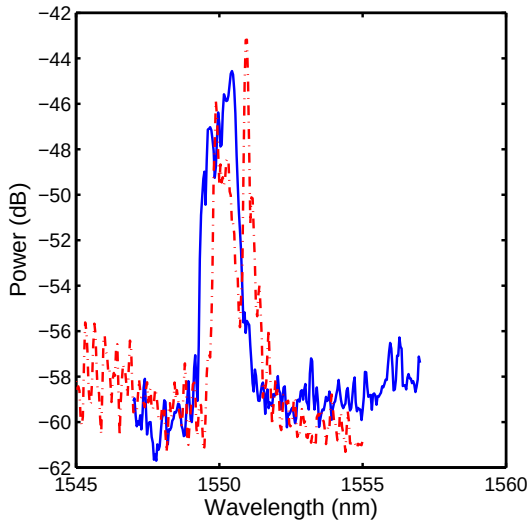

Figure 3.14: Comparison of spectra before (—) and after melting of the buffer (-·-) at 1.135 W

An examination of the spectrum of the grating after melting of the buffer with the Raman laser switched off (Figure 3.13) shows that there is extra spectral content on both sides of the grating spectrum. The addition of this spectral content, or chirping of the grating, was also reflected in the phase measurements recorded by the MZI, where a 29° change in the relative phases was observed.

The wavelength shift experienced by the grating does not diminish with the removal of the buffer. Figure 3.14 displays the spectra of the grating before and after melting of the buffer when 1.135 W of Raman power is launched through the fibre.

3.5 Discussion

The results reported in this chapter show that spectral modification of NIR femtosecond inscribed FBGs when exposed to high powers can become substantial (> 7 nm). This chirp, or broadening of the spectrum, results in a degradation of the signal being reflected from the grating and recorded at the photodiode. As the spectral bandwidth of the chirped grating approached the FSR of the interferometer (~ 2 nm), the grating

was reflecting close to the full period of the sinusoidal signal from the interferometer. This resulted in a decrease in the visibility of the signal detected at the photodiodes. In addition, the lock-in amplifier, set to lock onto the component closest to the reference signal, could not measure the chirp in the grating spectrum.

In the case of demodulation by interferometric configurations illuminated directly by the reflected component from an FBG, it would be expected that the interferometer output is affected. The spectrum broadens by a reduction in the intensity of the reflection spectrum and a decrease in the coherence length of the FBG reflection spectrum. Chang *et al.* [24] reported that the primary effect of spectral broadening due to strain gradients manifested itself as a change in the interferometer visibility for broadening > 2 nm.

In the work reported here, the ~ 2 nm FSR of the interferometer is exceeded by the spectral broadening of the grating reflection spectrum. The implications of broadening over such an extended wavelength range can be seen in the erroneous wavelength measurement returned by the configuration, with the interferometer reporting a wavelength shift (~ 1 nm) much less than the FSR. In such situations, the requirement for a demodulation scheme capable of characterising the grating reflection spectrum over its entire bandwidth becomes obvious and is the focus of the work reported in chapters 4 and 5.

There are also implications from the observations reported here for the use of NIR femtosecond laser inscribed gratings in an optical network where spectral stability is essential for deployment in applications such as tunable filters, dispersion compensation and wavelength division multiplexing. If the optical network is illuminated by a high power laser, wavelength shifts, chirps and permanent chirps or damage may be induced in the grating.

The long-term mechanical reliability of the fibre is also affected by melting of the buffer. Similar spectral modification, without melting of the buffer, has been reported in UV inscribed type IA gratings by Kalli *et al.* [12] when the grating is illuminated by high power lasers at 1410 nm and 1425 nm, coinciding with the 1400 nm absorption

band, but at much lower power levels (mW). The wavelength shift of the grating in this case was ~ 250 pm at a power level of 150 mW. The series of OSA images contained in Figure 3.4.2 illustrates the peak wavelength shift reflected by the NIR femtosecond laser inscribed gratings when the buffer melted off the fibre. In this case, the wavelength shift is ~ 250 pm for a 1 W power increase. In the work reported in [12], the authors were also able to demonstrate that standard UV inscribed type I gratings maintained a constant wavelength in the face of increasing power levels and they were also able to demonstrate partial erasure of the type IA grating after prolonged exposure to high power levels.

3.6 Conclusion

The effects of broad spectrum losses across NIR femtosecond laser inscribed gratings have been investigated. When high powers are used, even at wavelengths far removed from the Bragg condition, these losses produce an increase in the fibre temperature due to absorption in the coating. This temperature rise was monitored using the wavelength shift in the grating itself. At powers of a few watts, various temperature increases were experienced ranging from a few degrees up to the point where the buffer completely melts off the fibre at the grating site. The high temperatures can induce a permanent change in the grating profile. The work demonstrates the need to have tight control over the grating quality in high power applications.

Chirping of the grating spectrum can lead to erroneous results, depending on the interrogation unit. Fourier transform spectroscopy (FTS) exhibits a fundamental advantage over other interrogation techniques. The Fellgett or multiplex advantage can be exploited to provide broad wavelength measurement. Chapter 4 reports on the application of the Hilbert transform technique is applied to mechanically scanned interferometric measurements over long OPD scans, in order to provide high resolution measurement and exploit the Fellgett advantage of FTS.

References

[1] H.-N. Li, D.-S. Li, and G.-B. Song, "Recent Applications of Fiber Optic Sensors to Health Monitoring in Civil Engineering," *Engineering Structures*, vol. 26, pp. 1647–1657, 2004.

[2] D. C. Betz, G. Thursby, B. Culshaw, and W. J. Staszewski, "Identification of structural damage using multifunctional Bragg grating sensors: I Theory and implementation," *Smart Materials and Structures*, vol. 15, pp. 1305–1312, 2006.

[3] A. Martinez, M. D. I. Khrushchev, and I. Bennion, "Direct writing of fibre Bragg gratings by femtosecond laser," *Electronic Letters*, vol. 40, pp. 1170–1172, September 2004.

[4] A. D. Kersey and T. A. Berkoff, "Fiber-optic Bragg grating strain sensor with drift-compensated high-resolution interferometric wavelength-shift detection," *Optics Letters*, vol. 18, pp. 72–74, January 1993.

[5] T. M. Kwok, A. A. Pau, R. A. Betts, F. F. Ruhl, and G. F. Zheng, "Fabrication and characterisation of rare earth doped optical fibres," in *IEEE Region 10 Conference on Computer and Communication Systems*, vol. 1, pp. 104–108, 1990.

[6] M. N. Islam, "Raman amplifiers for telecommunications," *IEEE Journal of selscted topics in quantum electronics*, vol. 8, pp. 548–559, May/June 2002.

[7] J. Kulakofsky, W. Lewis, M. Robertson, T. Moore, and G. Krishnan, "Designing high-power components for optical communications," *Laser Induced Damage in Optical Materials: 2001*, vol. SPIE vol. 4679, pp. 198–210, March 2002.

[8] D. P. Hand and P. S. Russell, "Solitary Thermal Shock Waves and Optical Damage in Optical Fibres - The Fibre Fuse," *Optics Letters*, vol. 13, pp. 767–769, September 1988.

[9] K. Seo, N. Nishimura, and M. Shiino, "Evaluation of high-power endurance in optical fiber links," *Furukawa Review*, no. 24, pp. 17–22, 2003.

[10] R. M. Percival, E. S. R. Sikora, and R. Wyatt, "Catastrophic damage and accelerated ageing in bent fibres caused by high optical powers," *Electronics Letters*, vol. 36, pp. 414–416, March 2000.

[11] E. S. R. Sikora, D. J. McCartney, K. Farrow, and R. Davey, "Reduction in fibre reliability due to high optical power," *Electronics Letters*, vol. 39, pp. 1043–1044, July 2003.

[12] K. Kalli, A. G. Simpson, K. Zhou, L. Zhang, D. Birkin, T. Ellingham, and I. Bennion, "Spectral modification of type IA fibre Bragg gratings by high-power near-infrared lasers," *Meas. Sci. Technology*, vol. 17, pp. 968–974, 2006.

[13] A. D. Kersey, M. A. Davis, H. J. Patrick, M. LeBlanc, K. P. Koo, C. G. Askins, M. A. Putnam, and E. J. Friebele, "Fibre Grating Sensors," *Journal of Lightwave Technology*, vol. 15, no. 8, pp. 1442–1463, 1997.

[14] I. Riant, "Fiber Bragg gratings for optical telecommunications," *Comptes Rendus Physique*, vol. 4, pp. 41–49, 2003.

[15] T. Iwashima, A. Inoue, M. Shigematsu, M. Nishimura, and Y. Hattori, "Temperature compensation technique for fibre Bragg gratings using liquid crystalline polymer tubes," *Electronics Letters*, vol. 33, pp. 417–419, February 1997.

[16] Y. J. Rao, "Recent progress in applications of in-fibre Bragg grating sensors," *Optics and Lasers in Engineering*, vol. 31, pp. 297–324, 1999.

[17] L. Dong, J. L. Archambault, L. Reekie, P. S. J. Russell, and D. N. Payne, "Single pulse Bragg gratings written during fibre drawing," *Electronics Letters*, vol. 29, pp. 1577–1578, August 1993.

[18] C. Y. Wei, C. C. Ye, S. W. James, R. P. Tatam, and P. E. Irving, "The Influence of Hydrogen Loading and the Fabrication Process on the Mechanical Strength of Optical Fibre Bragg Gratings," *Optical Materials*, vol. 20, pp. 241–251, 2002.

[19] D. Homoelle, S. Wielandy, and A. L. Gaeta, "Infrared photosensitivity in silica glasses exposed to femtosecond laser pulses," *Optics Letters*, vol. 24, pp. 1311–1313, September 1999.

[20] L. Lepetit, G. Cheriaux, and M. Joffre, "Linear techniques of phase measurement by femtosecond spectral interferometry for applications in spectroscopy," *J. Opt. Soc. Am. B*, vol. 12, pp. 2467–2474, December 1995.

[21] S. Calvez, X. Rejeaunier, P. Mollier, J.-P. Goedgebuer, and W. T. Rhodes, "Erbium doped fiber laser tuning using two cascaded unbalanced Mach-Zehnder interferometers as intracavity filter: Numerical analysis and experimental confirmation," *Journal of Lightwave Technology*, vol. 19, pp. 893–898, June 2001.

[22] S. Abbenseth and S. I. Lochmann, “Distinct Enlargement of Network Size or Measurement Speed for Serial FBG Sensor Networks Utilizing SIK-DS-CDMA,” *Journal of Physics Conference Series*, vol. 15, pp. 149–154, 2005.

[23] M. LeBlanc, S. Y. Huang, M. Ohn, and R. M. Measures, “Distributed strain measurement based on a fiber Bragg grating and its reflection spectrum analysis,” *Optics Letters*, vol. 21, pp. 1405–1407, September 1996.

[24] C. C. Chang, G. A. Johnson, and S. T. Vohra, “Effects of fibre Bragg grating spectrum distortion on scanning Fabry-Perot and fiber interferometer based wavelength shift detection schemes.,” in *Proceedings of SPIE: International Conference on Optical Fiber Sensors*, vol. 3746, pp. 141–148, 1999.

Chapter 4

Long-scan Hilbert Transform Interferometric Delay Calibration

4.1 Introduction

Interferometry, the means of measuring the wavelength of light by direct comparison of a lightwave with itself or a delayed version of itself was described using the wave theory of the electromagnetic nature of light in Section 2.2.3. The resulting irradiance from the interaction of two or more lightwaves can deviate from the sum of the component irradiances to produce an interference pattern. The interference pattern, or fringes, produced in a temporally scanned interferometer are particularly suited to analysis by Fourier methods as outlined in Section 2.2.9.

However, in a temporally scanned system the frequency of the fringes observed at a detector is dependent on the velocity of the scanning mechanism. Any deviation from non-uniformity in this scanning velocity results in non-uniform sampling of the delay in the arms of the interferometer. Non-uniform delay sampling manifests itself as unwanted spectral content in the Fourier transform of the interferogram, which accumulates over long optical path difference (OPD) scans. Removal of the unwanted spectral content requires delay calibration based on referencing to a highly stable reference.

The Hilbert transform technique (HTT) for delay calibration has proved successful for short OPD scans [1]. This technique is based on retrieval of the temporal phase vector of the interferogram, which is obtained from the argument of the analytic signal. This is in turn obtained via Fourier transform processing. The efficacy of this technique for calibration of the long OPD scans required to provide high resolution

Fourier transform spectroscopic (FTS) measurements will be examined in the work in this chapter.

4.1.1 Fourier Transform Spectroscopy

Fourier Transform Spectroscopy (FTS) uses the classic Fourier relationship between the interferogram, $I_{os}(\tau)$, recovered in a temporal scan of the delay, τ, in the interferometer (Equation 2.2.21), and the power spectrum of the illuminating light (Equation 2.2.22) yielding

$$I_{os}(\tau) \propto R\left[\int_{-\infty}^{\infty} \hat{G}(\omega) exp\{-\imath\phi_{12}(\omega)\} exp\{-\imath\omega\tau\} d\omega\right] \tag{4.1.1}$$

A scan of the delay in one arm of the interferometer yields a discretely sampled interferogram of finite extent. Therefore, spectral analysis involves application of the discrete Fourier transform. The interferogram $I_{os}(\tau)$ has a discrete Fourier transform (DFT), F(ν), given by

$$F(\nu) = N^{-1} \sum_{\tau=0}^{N-1} I_{os}(\tau) e^{-i2\pi(\nu/N)\tau} \tag{4.1.2}$$

where the quantity ν/N is analogous to frequency measured in cycles per sampling interval [2]. The DFT is an approximation of the Fourier transform providing a finite set of discrete frequencies. There are inherent sources of potential error in spectral measurements using the DFT, for example:

- Aliasing. This arises if the initial sampling period is not sufficiently closely spaced to sample high frequency components in the function above that recommended by the Nyquist theorem, i.e. the sampling frequency must be greater than twice the signal bandwidth. [3].

- Truncation of data strings. This is not limited to the DFT.

The effect of the finite extent of the interferogram or truncation of data strings in the DFT is to convolve it with samples of the sinc function corresponding to the transform

of the rectangular window function describing the truncation [2]. The sinc function,

$$sinc(x) = \frac{sin(\pi x)}{\pi x} \tag{4.1.3}$$

is presented in Figures 4.1 and 4.2. The first zero of the sinc function occurs at the frequency at which the sinusoid completes one cycle in the rectangular window (length M), giving a central lobe width of 4 π /M [1, 4]. Subsequent zeros (z_i) occur for frequencies that complete i cycles in the window. The highest side lobe level of the sinc function is at ~ −13 dB below the central lobe [5]. These spectral sidelobes can be greatly reduced by choosing an appropriate windowing function [1].

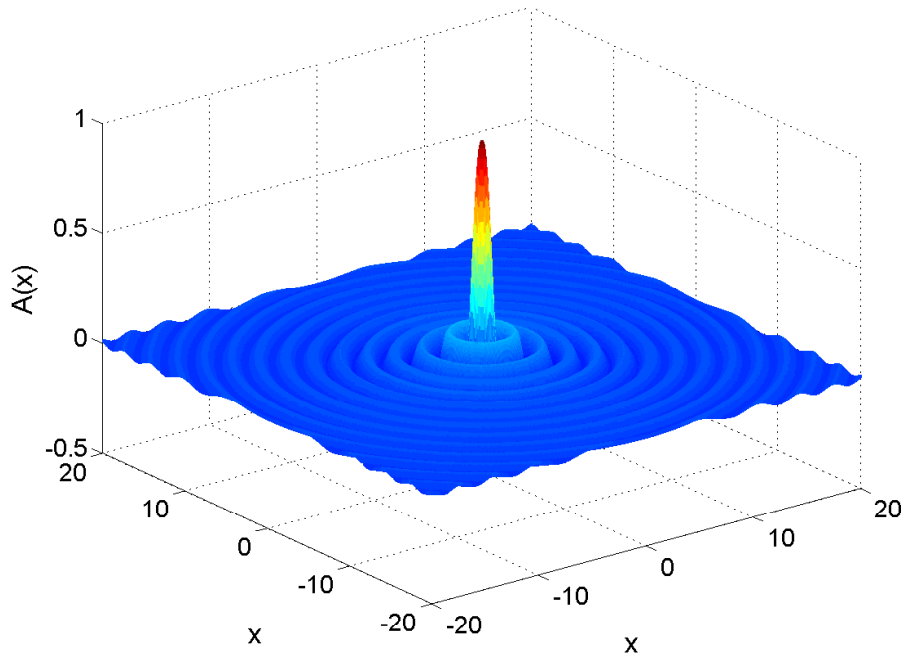

Figure 4.1: 3D representation of the sinc function

The Hamming window (which is applied to the interferograms in later sections) reduces the amplitude of the first sidelobes to ~ -43 dB below the central lobe [1, 5] at the expense of broadening the central lobe to $8\pi/M$ [1]. Equivalent figures of merit for different window types have been tabulated by Harris [5].

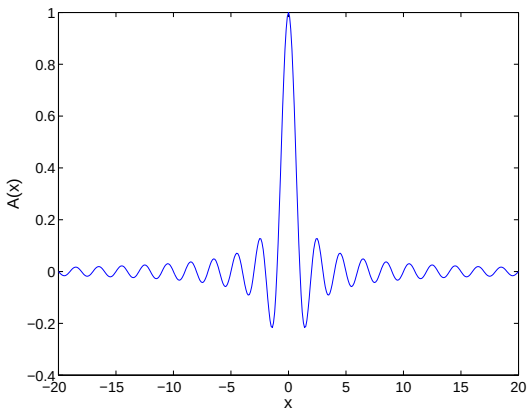

Figure 4.2: The 2D Sinc function

4.1.2 Interferometric Fourier Transform Spectroscopy

Interferometric Fourier Transform Spectroscopy (IFTS) is typically implemented on a temporally scanned Michelson interferometer and involves the scanning of an optical path difference by mechanical means. Bulk optic interferometers where the movable mirror is mounted on a translation stage are the subject of the work reported here. However, IFTS has also been implemented on all-fibre equivalents of the Michelson interferometer where the scanning mechanism is fibre stretching using piezoelectric stacks [6]. The implementation of an all-fibre mechanically scanned interferometer in the subject of the work reported in Chapter 6.

In a mechanically scanned interferometer, non-uniform scanning velocities result in non-uniform delay sampling, even when sampled evenly in time. This non-uniform sampling of the delay, τ, introduces false spectral content in the Fourier transform of the interferogram, $I_{os}(\tau)$, as described in Section 2.2.12.

For FTS, the minimum resolvable wavelength interval, $\delta(\lambda)$, is determined by the total OPD, τ_Δ and was defined in Section 2.2.9 as

$$\delta\lambda \approx n_a \frac{\lambda^2}{c\tau_\Delta} \tag{2.2.33}$$

where c is the speed of light in a vacuum and n_a is the group index of air. This implies that long OPD scans are required to provide high resolution. Therefore, a 1.2 ns delay

scan results in a wavelength resolution of ~ 1 pm at 632.8 nm which is the wavelength of the light source used for the measurements made in this chapter.

The false spectral content introduced in the Fourier transform of the acquired interferogram accumulates over long OPD scans. Conventionally, this false spectral content is corrected for by one of the following methods: by triggering sampling on the zero-crossings of a simultaneously acquired reference interferogram [7]; phase locked loop control based on a stable laser reference [6]; or by use of the Hilbert transform technique for correction of spectral degradation [1].

The method of triggering sampling on the zero-crossings of a simultaneously acquired reference has the advantages of a reduction in processing time and delay sampling accurately coinciding with the origin of delay τ. The method does however require sophisticated electronics, as does the phase locked loop control of the velocity of the scanning stages, whereas the Hilbert transform technique corrects for degradation in post processing based on the complex analytic signal of the reference interferogram.

The work reported in this chapter investigates the capability of the Hilbert transform technique to accurately calibrate the optical path difference in the interrogating interferometer in the presence of the accumulating effects of non-uniform sampling in the **long-scan** case.

4.1.3 Hilbert Transform Technique for OPD Calibration

The Hilbert transform technique for correction of spectral degradation has been extremely successful in producing constant OPD sampling. The technique involves post-processing, based on the phase evolution, $\phi(\tau)$, of the complex analytic signal, $z(\tau)$, of the interferogram derived from a Helium-Neon (HeNe) laser [1, 8] where

$$z(\tau) = A(\tau)e^{i\phi(\tau)} \tag{4.1.4}$$

The analytic signal is a complex signal, whose real component is the original signal, and has an imaginary component generated from the real signal by phase shifting all

frequency components by 90°, as described in Section 2.2.12. The analytic signal facilitates procuration of certain attributes of the real part, such as amplitude and phase. The temporal phase, $\phi(\tau)$, can be calculated from the argument of this complex temporal representation of the interferogram (see Section 2.2.12).

Despite the longitudinally multimode nature of the HeNe laser used for referencing in this work, the mean optical frequency is highly stable. Longitudinally multimode lasers have been used as the basis of the Hilbert transform approach [1], but single mode stabilised lasers are available. The signal phase effectively provides a mapping of the interferometric OPD, which, while equally sampled in time, are not equally sampled in delay, τ, due to non-uniform scanning velocity of the translation stage. The values of group delay are obtained from

$$\tau = \frac{\phi(\tau)\lambda}{2\pi c} \tag{2.2.49}$$

Previously reported applications of Hilbert transform based OPD recalibration have used scans < 9 mm [9]; the work reported here demonstrates its successful application for a 25-fold increase on that OPD.

4.1.4 Beam Collinearity

In practical applications of the Hilbert transform technique, measurement of optical properties ranging from dispersion to temperature/strain changes rely on the use of HeNe lasers to generate high coherence reference interferograms. These interferograms allow accurate calibration of the OPD by post processing using the Hilbert transform technique. This interferogram is usually captured in tandem with a measurand interferogram with both beams propagating down nearly identical paths in the demodulating interferometer (Figure 4.3). Inherent difficulties in maintaining the parallelism of the reference and measurand beams can cause measurement degradation due to pitch and yaw in the movement of the translation stage. This happens particularly in the case of long scans.

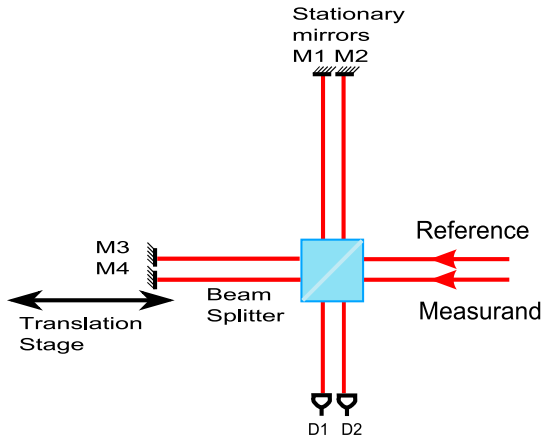

Figure 4.3: Co-propagating reference and measurand beams in a Michelson interferometer

These difficulties have been overcome by launching co-propagating reference and measurand beams through the interrogating interferometer [7, 10, 11]. Dyer [7] and Rochford *et al.* [10] used a reference beam filter and zero-crossing detection system to trigger sampling of the measurand beam. Murphy *et al.* [11] then separated the reference and measurand beams in the spectral domain, using a non-mechanically scanned system, where spectral degradation due to non-uniform velocity of a translation stage is not an issue. Spectral filtering of the signals obtained from a mechanically scanned interferometer, where spectral broadening due to non-uniform scanning velocity is an issue, requires that the wavelength separation between the reference and measurand beams is large enough to overcome this broadening and allow individual signal filtering.

The 1550 nm transmission window has become the window of choice for the telecommunications market as a result of two important parameters in electromagnetic propagation, attenuation and bandwidth (see Section 2.1.5). This has resulted in the mass production of 1550 nm single mode fibres and components which have also been deployed in optical sensing fields. The use of 632.8 nm HeNe lasers for referencing ensures a wavelength separation of ~ 900 nm between the reference and measurand beams, allowing for filtering in the spectral domain. Collinear propagation of the reference and measurand beams where referencing is based on a 632.8 nm laser requires

that the 632.8 nm reference beam propagates through fibre which is single mode at 1550 nm.

Section 2.1.3 outlined the conditions for single mode propagation in an optical fibre i.e. the normalised frequency of the fibre, V,

$$V = \frac{2\pi a}{\lambda}\sqrt{n_1^2 + n_2^2} \tag{2.1.14}$$

must be < 2.405. Therefore, a single mode fibre at 632.8 nm (HeNe wavelength) must have a core radius ~ 2.45 times smaller than the core for 1550 nm. This results in multimode 632.8 nm HeNe light propagating through the 1550 nm fibre. The number of modes propagating in a fibre can be conveniently expressed as a function of the normalised propagation constant, b, versus the normalised frequency, V [12, 13], where

$$b = \frac{(\beta/k)^2 - n_2^2}{n_1^2 - n_2^2} \tag{4.1.5}$$

giving six LP modes for a V number of 5.8 (632.8 nm light propagating in 1550 nm fibre).

The work reported in this chapter investigates the stability of long OPD Fourier transform spectroscopic interferometry where spectral measurements are based on both a single transverse mode laser reference and a multiple transverse mode laser reference.

4.2 Experimental Motivation and Objectives

The Hilbert transform technique for correction of the spectral degradation introduced in the Fourier transform of an interferogram had been successfully demonstrated for scan lengths $<$ 9 mm [9] acquired in a temporal scan of the delay in one arm of an interferometer. Fourier transform spectroscopy, however, requires long OPD scans to provide high resolution measurement. The work reported in the subsequent sections of this chapter develops a scanning interferometer for interrogation of fibre Bragg gratings at 1550 nm referenced from a 632.8 nm HeNe laser.

The effects of non-uniform scanning velocity are overcome via post-processing of high coherence interferograms using the Hilbert transform technique [1]. The use of a co-propagating reference aids alignment and minimises errors due to divergence between the measurand and reference beams. The most convenient method of achieving collinear propagation of both beams through the interrogating interferometer is to launch from a single fibre. 632.8 nm light is multimode in smf-28 fibre.

The objectives of the experimental work reported in this chapter were to investigate the robustness of **long-scan** FTS where delay calibration is conducted via Hilbert transform processing by:

- Demonstration of the effectiveness of the technique for correction of spectral degradation arising from non-uniform scanning of the interferometric OPD despite the accumulating effects over long OPD scans.
- Investigation of the reliability of a scheme based on the propagation of the HeNe beam in the demodulating interferometer despite the presence of multimodal transverse field structure in the reference beam.

4.3 Experimental Configuration

The experimental work reported in the following sections uses two sources obtained by launching a single HeNe laser into a 50/50 directional coupler. One source is single-mode at 632.8 nm and the second source is multimode at 632.8 nm. Both illuminate an interferometer and generate high coherence interferograms over long-OPD scans. The Hilbert transform technique is applied to the calibration of the delay scanned in the arms of the interferometer using both sources. A comparison of the efficacy of the technique for long-OPD recalibration using both beams is made by testing the spectral recovery of both sources.

Figure 4.4 illustrates the customised Michelson interferometer. HeNe light is injected into the single transverse mode, 633 nm downlead, via one arm of directional coupler, DC2, and exits at port P2. The second arm of coupler DC1 is spliced to a

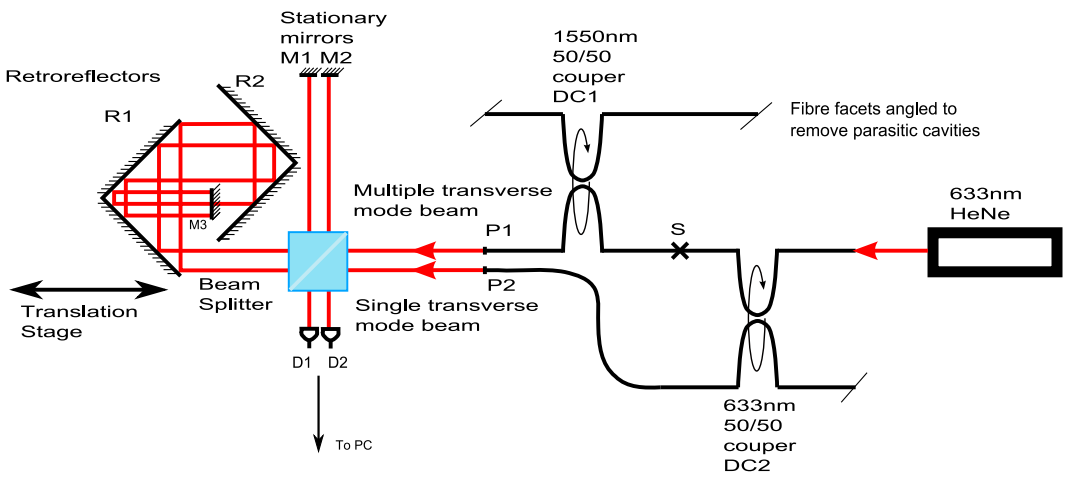

Figure 4.4: Long FTS Experimental configuration

wavelength flattened 1330-1550 nm directional coupler, DC1, giving a multiple transverse mode beam exiting the coupler at port P1. The light from both downleads is then launched simultaneously into the interferometer to follow separate but nearly parallel paths. The arrangement of retro-reflectors, R1 and R2, provides a multiplication of $6x$ the optical path difference than would normally have been obtained by scanning the translation stage through a distance of 300 mm. The translation stage was then scanned through 300 mm at a velocity of 2 mm/s, resulting in a 1.8 m scan taken in 150 s. The interference patterns generated at the output of the interferometer are detected by detectors D1 and D2.

The single mode interferogram was captured on a silicon (Si) photodiode, D1. The multimode interferogram was captured on a high speed Indium Gallium Arsenide (InGaAs) photodiode, D2. A detector sensitive to light at 1550 nm is required because of the low intensity 1550 nm measurand beam, which in a practical application would propagate along the same fibre as the 632 nm multimode reference beam. The spectral responses of the Si and InGaAs photodiodes are illustrated in Figure 4.5. The low quantum efficiency of the InGaAs detector at 632.8 nm did not prove limiting, as illustrated in Figure 4.10.

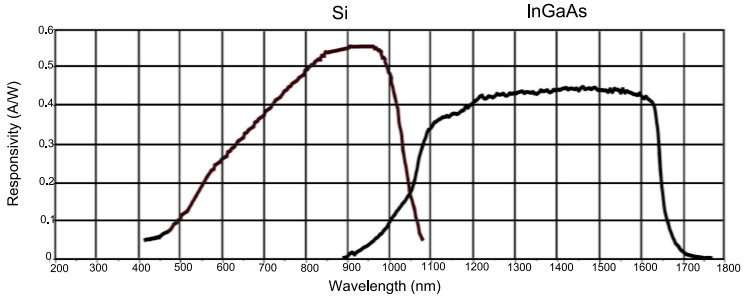

Figure 4.5: Typical spectral response curves for silicon (~ 400 - 1100 nm) and InGaAs (~ 900 - 1700 nm) photodetectors. [Data obtained from [14]]

4.4 Results and Discussion

4.4.1 Results

Interferogram Visibility

Figure 4.6 displays the interferograms derived simultaneously for the single-mode and over-mode HeNe beams from a single OPD scan of ~ 1100 mm (the higher frequency oscillations contained within the dark bands are illustrated in Figures 4.9 and 4.10). Despite the complex transverse modal structure of the multimode HeNe beam, it is obvious that the degradation in the visibility is not as significant as might be expected. The multiple modes in a source illuminating an interferometer would appear as different frequency components, thereby decreasing the coherence length of the source. Fringe amplitude/visibility remains within 6 dB of the maximum or ~ 550 mm in the single mode case and for under ~ 450 mm in the over-mode case. To illustrate the profile of the multimode beam exiting at port P1, a Dalsa piranha 8192 pixel line-scan camera was mounted on a translation stage and scanned through the beam in ~ 7 μm steps. Figure 4.7 shows the full profile of the beam with no evidence of distinct modes exiting the fibre. A single scan from the camera shown in Figure 4.8 displays a cross-sectional view of the beam through the centre. Again, while the profile is not gaussian, there are no distinct modes visible. Visual observation of the 632.8 nm beam exiting the 1550 nm fibre prior to reaching the coupler showed that two distinct modes

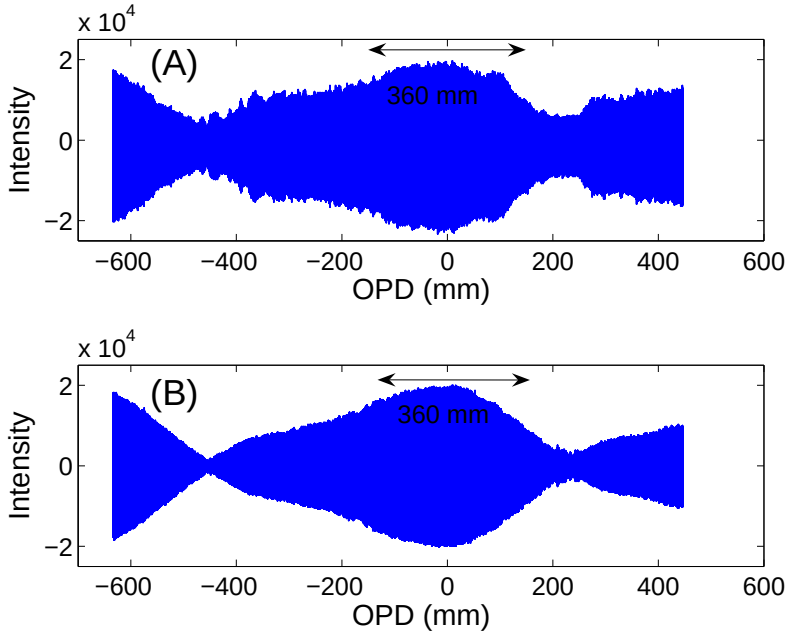

Figure 4.6: Interferograms obtained from (A) the singlemode and (B) the overmode beams.

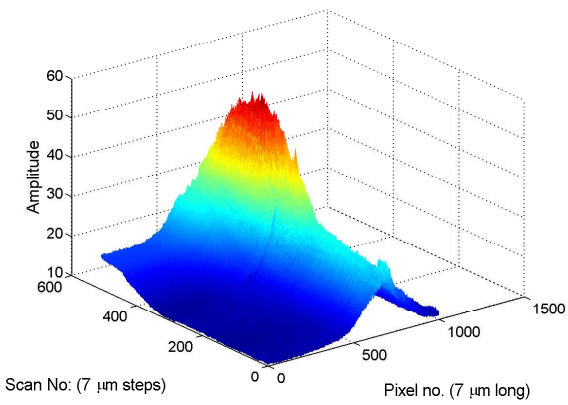

Figure 4.7: Multimode beam intensity profile obtained an a Dalsa piranha linescan camera.

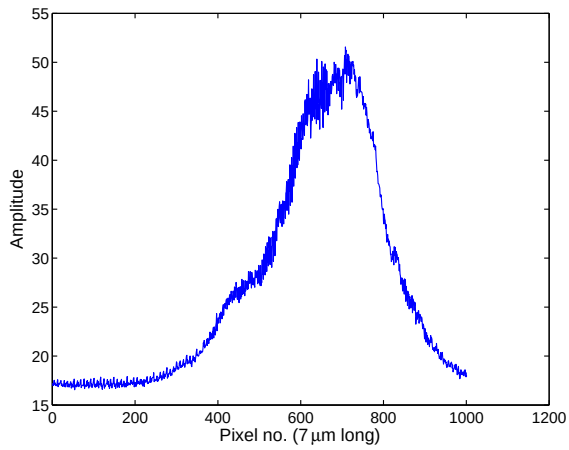

Figure 4.8: Cross section of the multimode beam taken with a Dalsa piranha linescan camera.

existed. This indicates that the couplers were having a stripping effect on the fibre modes. Figure 4.9(A) and Figure 4.10(A) illustrate the signal to noise levels (~ 10:1) obtained with the singlemode and multimode beams respectively. Figures 4.9(B) and 4.10(B) illustrate the high frequency component contained within the dark region of the interferogram with ~ 6 samples per fringe.

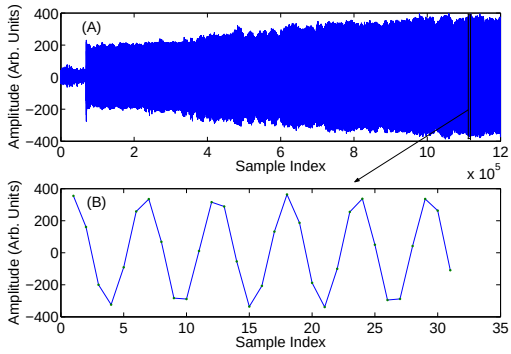

Figure 4.9: (A) Section of an interferogram obtained from the singlemode source. (B) High frequency content of the interferogram obtained from the boxed section of (A).

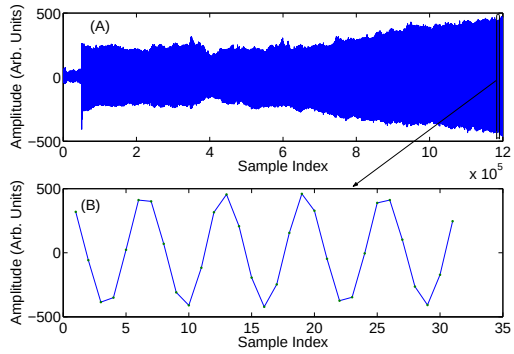

Figure 4.10: (A) Section of an interferogram obtained from the multimode source. (B) High frequency content of the interferogram obtained from the boxed section of (A).

The interferograms are Hamming windowed prior to processing to minimise spectral content due to leakage, as described in section 4.1.1. The windowed portion of the interferograms covers the central 360 mm OPD. The truncated interferograms are then fast Fourier transformed.

Interferometric Fourier Transform Spectroscopy

Figure 4.11 indicates the spectrum measured without calibration of the OPD sampling from the overmode HeNe beam. In this case, the spectral degradation can be seen to significantly broaden the spectrum recorded from the interference pattern.

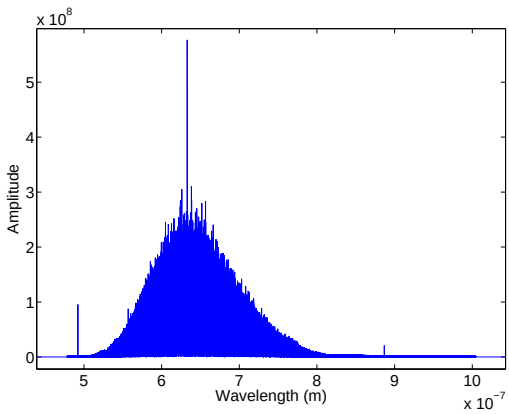

Figure 4.11: Spectrum of the overmode interferogram before recalibration

The complex analytic signal is found by doubling the inverse Fourier transform

of the positive frequency components of the Fourier transformed interferogram. The temporal phase (Figure 4.12) is calculated from the argument to this complex temporal representation of the interferogram. Delay values can be obtained from the relation-

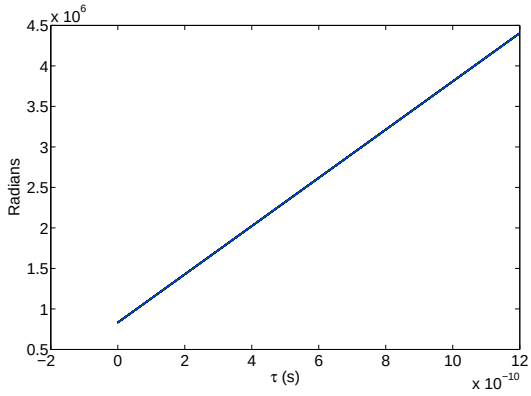

Figure 4.12: Unwrapped temporal phase vector

ship $\phi = \omega\tau$. The evolution of phase with respect to delay appears linear and well-behaved when a modulo 2π unwrapping algorithm is applied. However, the extent of the non-uniform velocity problem can be illustrated by examining a residual to a fit to the phase evolution of the interferogram before recalibration. The residual is generated through subtraction of a first order least squares fit to the phase curve. Figure 4.13 illustrates the large residual, showing non-uniformities introduced into the phase by both the non-uniform velocity of the translation stage and pitch and yaw movement of the mirror mounted on the stage.

Following delay correction using the Hilbert transform technique (described in Section 2.2.12), the residual generated from a fit to the extracted phase vector of the resampled interferogram clearly illustrates that these non-uniformities have been removed (Figure 4.14).

For a more rigorous test of the coherence attributes and for correction of the spectral degradation due to non-uniformities in the velocity of the translation stage using the Hilbert transform technique, the spectral recovery from these interferograms was tested via Fourier transformation.

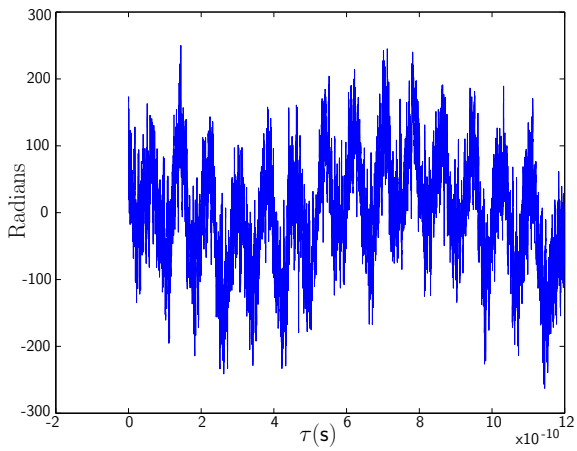

Figure 4.13: Residual to fit to phase before re-calibration

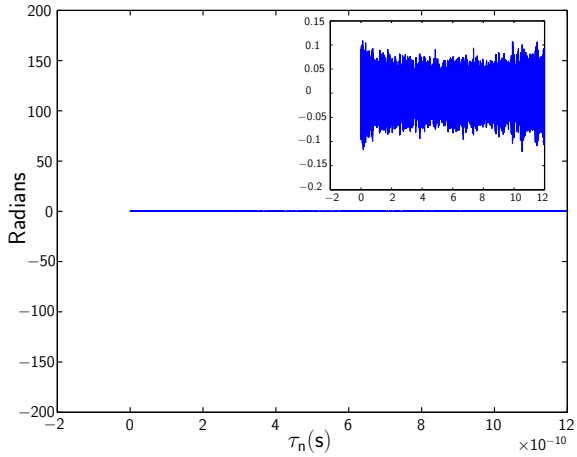

Figure 4.14: Residual to fit to phase after re-calibration

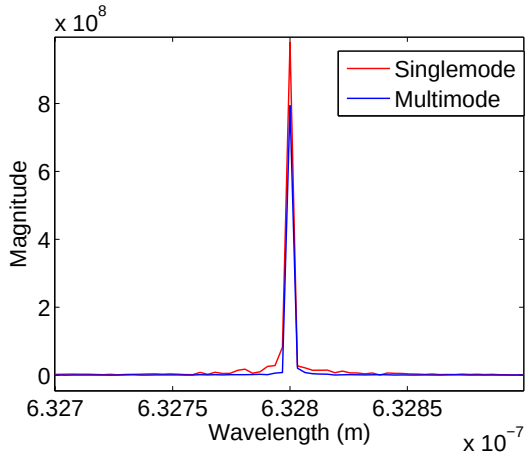

Figure 4.15: Spectra derived from 360 mm OPD sections of the singlemode and overmode interferograms

Figure 4.15 illustrates the respective HeNe spectra derived from central segments of 360 mm OPD of both interferograms after self-calibration using the Hilbert transform technique. Neglecting the minor intensity differences, the spectral recovery from each of the the interferograms are identical, within the limits of the resolution of the Fourier transform. The specifications for the HeNe laser (Melles Griot 05-LHR-151) specify a total linewidth of ~ 0.5 pm, which is less than the measurement resolution of a Fourier transformed 360 mm interferogram segment. The total linewidth of the spectra recovered in the work reported here is ~ 2 pm.

4.4.2 Discussion

OPD Calibration

The science of optical sensing requires high accuracy wavelength measurements because a wavelength measurement uncertainty as small as 1 pm leads to measurement uncertainty of $\sim 0.1^{o}C$ [15] or $\sim 1\mu\epsilon$ [16,17]. In mechanically scanned systems, the performance degradation due to non-uniform OPD scanning can accumulate over long, high speed OPD scans, leading to significant spectral broadening ($\sim$ 300 nm). This is seen in the magnitude of the Fourier transform of the interferogram (Figure 4.11). The work reported here demonstrates that the Hilbert transform technique can accurately calibrate the delay in the interferometer arms over long OPD scans ($\sim$ 360 mm) to remove the accumulated spectral content due to non-uniform sampling of the delay.

Beam Collinearity

Interferometric interrogation units using Hilbert transform processing or zero crossing detection for OPD calibration generally have reference beams based on the spectra of highly stable (< 1 pm) single transverse mode lasers [1, 7, 10, 18, 19]. The largest source of uncertainty in interferometric systems referenced by a co-propagating reference beam is the error due to coalignment of the beams [7, 10]. This uncertainty has previously been eliminated by launching the measurement and reference signals into the same fibre where both beams remained singlemode [7, 11].

In the work reported in this chapter, the fibre used to launch the 632.8 nm light into the interferometer was single mode at 1550 nm and as such should support higher order modes of the 632.8 nm beam. Visual inspection of the transverse intensity pattern from the 1550 nm fibre found it to be circular with no evidence of distinguishable higher order modes. This indicates that, at the very least, there is a dominant $LP_{0,1}$ mode propagating along the fibre, supporting the mode stripping effect of directional couplers over a larger 900 nm range. This was noted previously by Flavin *et al.* [20] when they launched 510 nm light into a fibre with a cut-off wavelength of 610 nm.

The suppression of higher order modes of 850 nm light propagating in 1550 nm

fibres has previously been eliminated by spatial filtering of the multimode beam by passing the beam through a short length of HI780 fibre [21]. Spatial filtering of the 632.8 nm reference beam in a similar manner prior to detection, however, would require the addition of an extra detection channel and associated components to the interrogation unit. This is because the losses experienced by the 1550 nm beam when propagating through ~ 10 cm of 632.8 nm fibre were significant enough not to permit detection of the 1550 nm light.

A third method for suppression of the higher order modes of the 632.8 nm reference would involve the use of endlessly singlemode photonic crystal fibre (PCF) [22]. PCF fibres are ideally suited to the interferometric interrogation of FBG arrays as the endlessly single mode nature of the fibre would allow extension of the wavelength range between measurand and reference beams propagating through the same single mode fibre. In the experimental configuration above (Figure 4.4), PCF fibre would also eliminate the requirement for the 633 nm coupler.

4.5 Conclusion

This work has demonstrated the effectiveness of the Hilbert transform technique for the correction of spectral degradation arising from non-uniform scanning of the interferometric OPD for scans $< 25x$ those previously reported [1, 11]. The stability of the technique to correct for non-uniform scanning of the OPD in the long scan case, where the multimode transverse field structure has been effectively stripped from the fibre, has been verified. The technique provides identical spectral measurements to the singlemode beam for scans up to 360 mm, providing a wavelength measurement resolution of ~ 1 pm in the Fourier transformation at 633 nm.

The customised Michelson interferometer will be applied in chapter 5 to the interrogation of fibre Bragg grating arrays for provision of high resolution measurement of light reflected from the gratings.

References

[1] D. Flavin, R. McBride, and J. D. C. Jones, "Short-Scan Interferometric Interrogation and Multiplexing of Fibre Bragg Grating Sensors," *Optics Communications*, vol. 170, no. 4-6, pp. 347–353, 1999.

[2] R. N. Bracewell, *The Fourier Transform and its Applications.* McGraw-Hill, 3rd ed., 2000. ISBN 0-07-303938-1.

[3] R. Williams, *Spectroscopy and the Fourier Transform: An Interactive Tutorial.* VCH Publishers, Inc., 1996.

[4] S. W. Smith, *The Scientist and Engineer's Guide to Digital Signal Processing.* California Technical Publishing, October 2003. ISBN : 0-9660176-3-3.

[5] F. J. Harris, "On the use of windows for harmonic analysis with the discrete fourier transform," in *Proceedings of the IEEE*, vol. 66, pp. 51–83, 1978.

[6] M. Davis and A. Kersey, "Application of a Fibre Fourier Transform Spectrometer to the Detection of Wavelength Encoded Signals from Bragg Grating Sensors," *Journal of Lightwave Technology*, vol. 13, no. 7, pp. 1289–1295, 1995.

[7] S. D. Dyer, P. A. Williams, R. J. Espejo, J. D. Kofler, and S. M. Etzel, "Fundamental limits in fiber Bragg grating peak wavelength measurements," in *Proceedings of SPIE* (M. Voet, R. Willsch, W. Ecke, J. Jones, and B. Culshaw, eds.), vol. 5855, (Bellingham, WA.), pp. 88–93, SPIE, 2005.

[8] D. A. Flavin, R. McBride, and J. D. C. Jones, "Short Optical Path Scan Interferometric Interrogation of a Fibre Bragg Grating Embedded in a Composite," *Electronic Letters*, vol. 33, 1997.

[9] J. H. Rothwell and D. A. Flavin, "Dispersion Measurement by White Light Interferometry Based on Fresnel Reflections," in *CLEO-Europe*, (Munich, Germany), 2002.

[10] K. B. Rochford and S. D. Dyer, "Demultiplexing of Interferometrically Interrogated Fiber Bragg Grating Sensors Using Hilbert Transform Processing," *Journal of Lightwave Technology*, vol. 17, no. 5, pp. 831–836, 1999.

[11] D. F. Murphy, D. A. Flavin, R. McBride, and J. D. C. Jones, "Interferometric interrogation of in-fiber Bragg grating sensors without mechanical path length scanning," *Journal of Lightwave Technology*, vol. 19, pp. 1004–1009, July 2001.

[12] G. Keiser, *Optical Fiber Communications*. Electrical and Electronic Engineering, Singapore: McGraw-Hill, 2nd ed., 1991. ISBN 0-07-100785-7.

[13] G. Lachs, *Fibre Optic Communications: Systems, Analysis and Enhancements*. McGraw-Hill, 1998, ISBN:0-07-038279-4.

[14] "www.macphersoninc.com."

[15] J. Jung, H. Nam, B. Lee, J. O. Byun, and N. S. Kim, "Fiber Bragg grating temperature sensor with controlable sensitivity," *Applied Optics*, vol. 38, pp. 2752–2754, May 1999.

[16] Y.-J. Rao, "In-fibre Bragg grating sensors," *Meas. Sci. Technol.*, vol. 8, pp. 355–375, 1997.

[17] B. Lee, "Review of the Present Status of Optical Fibre Sensors," *Optical Fibre Technology*, vol. 9, no. 2, pp. 57–59, 2003.

[18] S. D. Dyer and K. B. Rochford, "Low coherence interferometric measurements of fibre Bragg grating dispersion," *Electronics Letters*, vol. 35, pp. 1485–1486, August 1999.

[19] G. M. Flockhart, R. R. J. Maier, J. S. Barton, W. N. MacPherson, J. D. C. Jones, K. E. Chisholm, L. Zhang, I. Bennion, I. Read, and P. D. Foote, "Quadratic behaviour of fibre Bragg grating temperature coefficients," *Applied Optics*, vol. 43, no. 13, pp. 2744–2751, 2004.

[20] D. A. Flavin, R. McBride, and J. D. C. Jones, "Interferometric fiber-optic sensing based on the modulation of group delay and first order dispersion: Application to strain-temperature measurand," *Journal of Lightwave Technology*, vol. 13, pp. 1314–1323, July 1995.

[21] X. Tang, A. Mink, A. Nakassis, H. Xu, B. Hershman, J. Bienfang, D. Su, R. F. Boisvert, C. Clark, and C. Williams, "Quantum key distribution system operating at sifted key rate over 4 mbit/s," in *Proceedings of SPIE: Quantum Information and Computing IV* (E. J. Donkor, A. R. Pirich, and H. E. Brandt, eds.), vol. 6244, 2006.

[22] T. A. Birks, J. C. Knight, and P. S. J. Russell, "Endlessly single-mode photonic crystal fiber," *Optics Letters*, vol. 22, pp. 961–963, July 1997.

Chapter 5

Long Optical Path Difference Fourier Transform Spectroscopic demodulation of Fibre Bragg Grating sensor arrays

5.1 Introduction

One of the main advantages of fibre Bragg gratings (FBGs) is their unique wavelength multiplexing capacity as described previously in Section 2.1.10. Research into wavelength-division demultiplexing of serial FBG arrays continues to be an active field [1, 2], with strong potential for commercialisation [3]. The development of supercontinuum broadband sources based on supercontinuum generation in photonic crystal fibres increases the usable optical bandwidth and releases the potential for serial multiplexing of Bragg gratings over far greater wavelength ranges than previously reported [4]; for example Ranka *et al.* have reported a broad (~1200 nm), flat spectrum [5].

However, at present, established approaches to FBG demodulation—tunable laser [6–8], tunable filter [9, 10], diode array [11]— are limited in their ability to cope with such broad wavelength ranges. For example, interrogation using tunable components is limited by the tunable range and tuning speed and interrogates each grating in the array sequentially (eg. JDSU MAP tunable laser has a tunable range of ~ 110 nm with a maximum tuning speed of 100 nm/s). The acousto-optic tunable filter of Boulet *et*

al. [9] is capable of simultaneous interrogation of an array of gratings but requires amplitude modulation at different frequencies for each of the gratings in the array and bandpass filters for each of the components. Interrogation using diode arrays and a diffraction grating [11] requires the addition of detectors as the wavelength range of the array is increased.

Interferometric Fourier Transform Spectroscopy (IFTS) offers unique potential for the demodulation of FBG arrays over extended wavelength ranges because of the Fellgett (or multiplex) advantage of Fourier transform spectroscopy [12]. Short scan IFTS based on the Hilbert transform technique has been demonstrated to yield high resolution measurement of the mean grating wavelengths, but without information on the internal characteristics of the individual grating reflection spectra [13]. It has been suggested that high resolution measurement of the structural detail of FBG sensors is potentially valuable in the detection of non-uniform measurand fields within the grating [14]. Long-scan FTS has the potential to demodulate gratings over extremely broad wavelength ranges, while simultaneously characterising the intra-grating spectral detail of all component array gratings (c.f. Section 2.2.9).

Chapter 4 illustrated the spectral broadening induced by a mechanically scanned system in case of a HeNe laser spectrum. Similarly, the reflection spectrum of the individual gratings in an array of FBG sensors would be indistinguishable because of the extra spectral content introduced due to non-uniform sampling of the delay in the arms of the interrogating interferometer. The ability of the Hilbert transform technique for correction of spectral degradation due to non-uniformities in scanning of the interferometric OPD has also been demonstrated in chapter 4. The work reported in this chapter will investigate the capability of long-scan FTS for demodulation of sensor arrays while simultaneously recovering the spectral detail of all gratings in the array. Chapter 4 demonstrated the capability of a 632.8 nm reference beam propagating through a 1550 nm fibre for self-calibration. The efficacy of a calibration scheme based on the collinear propagation of the reference and Bragg grating beams in the demodulating interferometer will be demonstrated here. The relative performance of

this reference beam, relative to a single mode reference, is evaluated in the context of temperature sensing and high resolution intra-grating spectral measurements.

5.1.1 Fibre Bragg Gratings

In the optical sensing field, FBGs have proved to be one of the most promising candidates for use as embedded sensors in fibre-optic smart structures [15], while in the telecommunications field they have been used for applications such as wavelength division multiplexing (WDM), narrow band tunable filters and for dispersion compensation [16]. The ease of implementation of FBGs in WDM applications is a consequence of the grating inscription process.

FBG Inscription

As outlined in section 2.1.13, the development of side-writing techniques for grating inscription [17–20] allows tailoring of the Bragg wavelength or the peak reflective wavelength (λ_B) of the grating, to reflect at any wavelength [21–23], independent of the wavelength of the inscribing source [18] where

$$\lambda_B = 2n_{eff}\Lambda \tag{2.1.41}$$

n_{eff} is the effective refractive index and Λ is the periodicity of the refractive index variation. The interference maxima and and the index change are set by the angle between

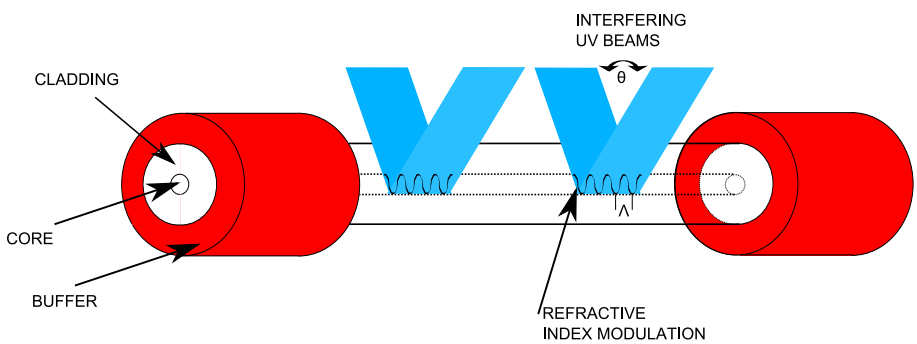

Figure 5.1: Standard UV inscription of an array of FBGs.

the interfering beams (Figure 5.1). As such, the gratings are ideally suited for WDM,

where an array of gratings can easily be inscribed along the length of a fibre by variation of the angle θ between the interfering beams.

Temperature and Strain Sensitivities

The resonant Bragg wavelength is sensitive to strain and temperature as it depends on the grating periodicity and the effective refractive index, both of which will change due to the intrinsic sensitivity of the fibre. When the grating experiences a change in temperature or strain (or both), there is a corresponding change in the reflected wavelength of the grating. A change in strain results in both a physical change in the grating period and a change in the refractive index due to the strain-optic effect. A change in temperature, T, results in both a change in the refractive index, n, due to the thermo-optic coefficient, ξ, and a change in the physical length of the grating which can be described by the thermal expansion coefficient, α, as described in Section 2.1.12. Equation 2.1.63 quantified the total contributions of the strain-optic effect and the thermo-optic coefficients [24], and is given here for convenience.

$$\Delta\lambda_B = 2n\Lambda\left(\left[1 - \frac{n^2}{2}\{P_{12} - \nu(P_{11} + P_{12})\}\right]\varepsilon + [\alpha + \xi]\,\Delta T\right) \tag{2.1.63}$$

The contribution of a wavelength component by each section of the grating to the reflection spectrum [25] was outlined in Section 2.1.12 and is given by

$$\lambda_B(z) = 2n(z)\Lambda(z) \tag{2.1.69}$$

Therefore, a uniform measurand along the length of the grating will manifest itself as a uniform shift in the reflection spectrum. A non-uniform measurand along the grating's length, however, results in a broadened reflection spectrum as demonstrated in chapter 3. The change in the reflection spectrum with a change in strain ($\Delta\epsilon$) and a change in temperature (ΔT) can be obtained from equation 2.1.69. $n_{eff}(z)$ and $\Lambda(z)$

are dependent on $\epsilon(z)$ and $T(z)$ according to

$$\begin{aligned}\Delta\lambda_B(z) &= 2\left(n_{eff}(z)\frac{\delta\Lambda(z)}{\delta\epsilon(z)} + \Lambda(z)\frac{\delta n_{eff}(z)}{\delta\epsilon(z)}\right)\Delta\epsilon(z) \\ &+ 2\left(n_{eff}(z)\frac{\delta\Lambda(z)}{\delta T(z)} + \Lambda(z)\frac{\delta n_{eff}(z)}{\delta T(z)}\right)\Delta T(z) \qquad (5.1.1)\end{aligned}$$

The first and second terms describe the contributions of strain and temperature respectively. Within these terms, the first and second terms describe the contribution due to the change in the grating periodicity Λ and the refractive index n_{eff} respectively. Typical sensitivities at 1550 nm for the wavelength dependence are: strain ~ 1.2 $pm/\mu\epsilon$ and temperature ~ 12 $pm/^{o}$C [26].

Interferometric Fourier Transform Spectroscopy

The interferometric Fourier transform spectroscopic (IFTS) approach to Bragg grating sensor demodulation, and the associated Hilbert transform technique (HTT), relies on the illumination of a Michelson interferometer by the light reflected from the grating. A temporal scan of the delay, τ, in one arm of the interferometer generates an interferogram from which the spectrum of the light reflected from an FBG array can be fully characterised from the Fourier transform (FT) of the interferogram, as described in Section 2.2.3.

For FTS, the minimum resolvable wavelength interval, $\delta\lambda$, is determined by the total OPD, τ_Δ. Therefore, long OPD scans are required to yield high resolution measurement of the spectral structure of the gratings. From Equation 2.2.33, a delay scan of τ_Δ = 800 ps will therefore provide a resolution of ~ 10 pm at 1550 nm.

Delay Calibration

The accumulating effects of non-uniform sampling of the delay in a mechanically scanned system result in unwanted spectral content in the FT of the interferogram [13]. Non-uniform delay sampling is a consequence of the non-uniform scanning speed of mechanical components as the frequency of the fringes, f, observed at the output is

a function of the scanning velocity [27](cf Section 2.2.9, Equation 2.2.32). Removal of the added spectral content requires calibration using a high-coherence reference beam, generally conducted by a zero-crossing detection circuit [28] or by the Hilbert transform technique [13].

The Hilbert transform technique for OPD calibration operates on the principle that the analytic signal (A(τ)) is obtained from the inverse Fourier transform of the positive frequency components of the interferogram. A(τ) has been previously defined in section 2.2.12 and may be rewritten as

$$A(\tau) = F^{-1}[2u(\omega)FI_{os}(\tau)] \tag{5.1.2}$$

where F denotes the Fourier transform, $u(\omega)$ is the Heaviside step function which is 0 for $\omega < 0$, 0.5 for $\omega = 0$ and unity for $\omega > 0$. A temporal phase vector ($\phi(\tau)$) can be retrieved from the argument of $A(\tau)$ [29], which effectively maps the delay in the interferometer arms through the simple relationship $\phi(\tau) = \omega\tau$ where ω is the mean frequency of the reference beam. Delay correction is then achieved through interpolation of the captured interferograms based on the expected delay intervals calculated from an ideal HeNe interferogram. This redistributes the measured interferogram intensities in delay, thus correcting for non-uniformities in delay sampling due to the non-uniform OPD scan velocity.

Beam Co-propagation

Typical referencing schemes using the Hilbert transform technique for delay calibration rely on the illumination of the interferometer with the measurand and reference beams propagating in parallel, along nearly identical paths, through the interrogating interferometer as illustrated previously in Figure 4.3. Measurement degradation can occur due to difficulties in maintaining the parallelism of the beams, particularly in the case of long OPD scans.

These difficulties may be overcome by launching co-propagating beams through

the interferometer and sampling the measurand interferogram on the zero crossings of the reference beam [28, 30]. The mass production of fibres and components in the O, E, S, C, L and U bands for telecommunications (Table 5.1) has resulted in a readily available supply of fibres and components for the optical sensing field which would not have otherwise been the case.

Telecommunications Band	Wavelength Range
O - Band	1260 - 1360 nm
E - Band	1360 - 1460 nm
S - Band	1460 - 1530 nm
C - Band	1525 - 1565 nm
L - Band	1565 - 1625 nm
U - Band	1625 - 1675 nm

Table 5.1: Telecommunications Bands [31]

Spectral domain filtering of the reference and measurand beams requires that the spectra of both beams are separable in the frequency domain. The frequency of fringes obtained in a temporal scan of the delay in one arm of an interferometer is dependent on the velocity of the translation stage (V_m) and the wavenumber of the light ($\bar{\nu}$) given by Equation 2.2.32 [27]

$$f = \frac{2V_m\nu}{c} = 2V_m\bar{\nu} \tag{2.2.32}$$

Therefore, spectral domain filtering requires that the reference and measurand beams be separated far enough in wavelength to overcome the effects of spectral broadening. Figure 4.11 in Section 4.4.1 illustrated the extent of spectral broadening (~ 300 nm) in the interferometric interrogation unit that will be applied to the demodulation of the FBG arrays later in this chapter. The use of a 632.8 nm HeNe reference laser to reference an array of gratings centered at 1550 nm allows separation of the spectra in the Fourier transform of a composite beam obtained from the HeNe and grating interferograms.

In the work reported in this chapter, the technique of accurate OPD calibration, developed in chapter 4, which is based on referencing to a transversely multimode 632.8 nm laser propagating through 1550 nm fibre, and where mode filtering is accomplished via a directional coupler is applied to the interrogation of an array of FBGs.

This method allows co-propagation of the reference and measurand beams through the interferometer when launched through a 1550 nm downlead.

5.2 Experimental Motivation and Objectives

The efficacy of the Hilbert transform technique for accurate calibration of the delay in a temporally scanned interferometer was demonstrated in Chapter 4, in the presence of the accumulating effects of non-uniform delay sampling which cause significant spectral degradation. The capability of a transversely multimode laser beam propagating through the interferometer for accurate delay calibration was also reported.

The objectives of the experimental work reported here were to apply the high-resolution interrogation unit to:

- Investigate the capability of **long-scan** FTS for demodulation of FBG sensor arrays with simultaneous recovery of spectral detail of all array gratings; all measurements are achieved in a single scan of the OPD, from an interferogram captured on a single InGaAs photodiode and are based on referencing to a transversely multimode laser.

- Evaluate the relative performance of the transversely multi-mode reference, relative to a single mode reference in the context of temperature sensing and high resolution intra-grating spectral measurement.

5.3 Experimental Configuration

An array of FBGs is attached to the long scan customised Michelson interferometer demonstrated in chapter 4. The experimental arrangement is illustrated in Figure 5.2. The Bragg grating array is illuminated by an Optospeed superluminescent diode (SLED1550S5, central wavelength 1530 - 1570 nm, -3 dB optical bandwidth > 50 nm). The gratings in the array have resonant wavelengths of 1538 nm, 1549 nm and 1565 nm. The spectral linewidths (FWHM) are in the ranges 0.2-0.5 nm. The light reflected

from the array exits coupler DC1 at the output port P1, to illuminate the interferometer. HeNe light is injected into the downlead, via directional coupler DC2, with splicing of the 633 nm and 1550 nm fibres at S. The irradiance at the output of the interferometer due to the individual beams may be obtained from Equation 4.1.1 to yield

$$I_{B,R}(\tau) = 2I_{B0,R0}\left[1 + V_{B,R}(\tau)Cos\ \phi_{B,R}(\tau)\right] \tag{5.3.1}$$

where $V(\tau)$ is the interferogram visibility and $\phi(\tau) = \bar{\omega}\tau$. The subscripts B and R refer to the Bragg grating and Reference beams respectively. The signals $I_B(\tau)$ and $I_R(\tau)$ are filtered in the spectral domain.

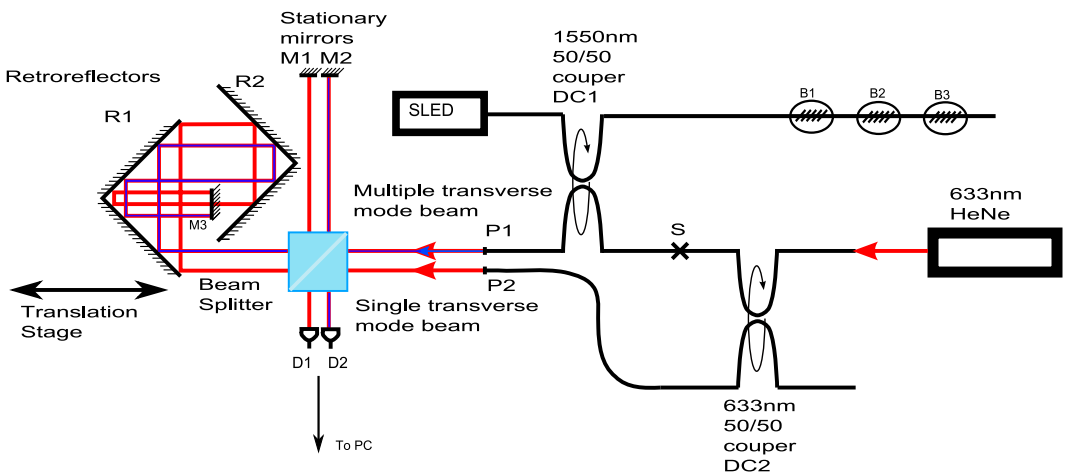

Figure 5.2: FTS for demodulation of FBG arrays

In the normal measurement system, the port P2 would be redundant but here it allows access to a single-mode (transverse) HeNe beam for experimental comparisons with the multimode (transverse) beam emerging from P1. For a measurement scan the retro-reflector R1 is scanned through a physical displacement of 60 mm—this gives a total OPD of 240 mm (via a $6x$ beam folding arrangement using retro-reflectors R1 and R2) and a resulting resolution of 10 pm in wavelength measurements at 1550 nm. The composite interferograms formed by the grating reflections and the over-mode HeNe beams are captured on a single InGaAs photodiode D2—the low quantum efficiency of

the InGaAs photodiode at 633nm did not prove limiting (cf. Section 4.3). The sampling density corresponds to 5 samples per HeNe fringe.

The temperature measurements on the gratings in the array discussed in the next section were made by placing the individual grating in the array into a specially constructed oven, with the temperature of the oven controlled by a single peltier module controlled by an MPT-10000 series thermo-electric controller giving a short-term stability of 0.005 °C over 1 hour. The oven walls were constructed from a hardened plastic, encased in insulating foam, with a circular groove cut into both ends through which the fibre Bragg grating was placed in the oven, resting in a cardboard tube. The temperature at the grating site was monitored by placing 4 thermocouples along the length of the cardboard tube directly underneath the fibre. The oven temperature was taken as the average of the 4 readings from the thermocouples.

5.4 Results and Discussion

Interferometric Fourier Transform Spectroscopy

Figure 5.3 displays the interferogram captured at the photodiode D2 for the full 240 mm OPD. Figure 5.4 displays the interferogram for the 1538 nm Bragg grating alone—the spectral content of this grating reflection is echoed in the 'lobed' structure of the interferogram (Figure 5.10). The interferograms are Hamming windowed to limit spectral leakage due to the finite data set as outlined in section 4.1.1.

Figure 5.5 displays the high frequency content of the composite interferogram. The fringes consist of both the high frequency 632.8 nm light and the lower frequency light reflected from the Bragg grating array. The sampling density was set to sample the HeNe frequency at ~ 5 samples per fringe.

Figure 5.6 shows the magnitude of the Fourier transform of the composite interferogram. The individual components of the three Bragg gratings are not resolved due to the non-uniformity of the motion of the translation stage and the consequent non-uniformity in the intervals of the OPD scanning.

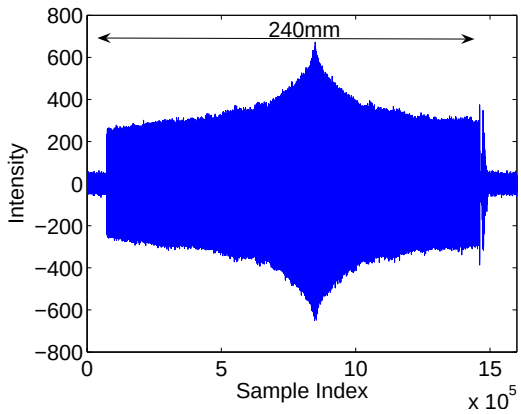

Figure 5.3: Composite interferogram from HeNe and array

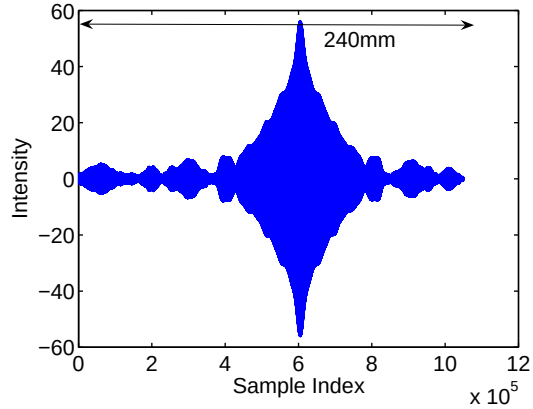

Figure 5.4: Interferogram obtained from 1538 nm grating alone

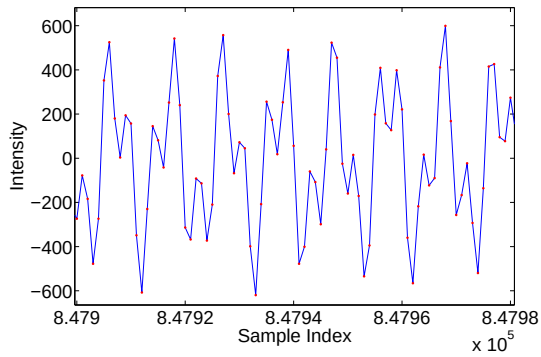

Figure 5.5: High frequency content of the composite interferogram.

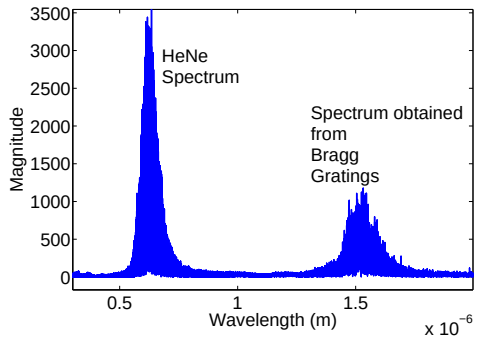

Figure 5.6: Magnitude of the Fourier transform of the composite interferogram before recalibration

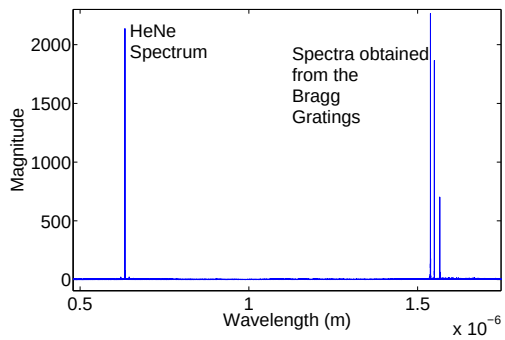

Figure 5.7: Magnitude of the Fourier transform of the composite interferogram after recalibration

The Hilbert transform method is used to recalibrate the OPD—this had previously been used in the case of shorter OPD scans where the reference HeNe beam had a single transverse mode [13, 32], but here it is successfully used for a longer scan using a

multiple transverse mode HeNe beam. Figure 5.7 indicates the spectra obtained from the recalibrated interferogram, in which the individual grating spectra are resolved. Figure 5.7 also indicates the potential measurable wavelength range for an array. In principle an array of gratings spanning the wavelength range from 630 nm to 1550 nm could be demodulated. In a more practical arrangement the configuration could readily demodulate gratings across the full range of the E, S, C and L telecommunications bands in conjunction with a suitable broadband source. The approach also opens up the possibility of the single demodulator for a strain temperature discrimination scheme based on first order and second order effects in both FBG's and long period gratings (LPGs) [33].

Sensor Array Demodulation

FTS-based demodulation of FBG arrays offers the attribute of simultaneously measuring the measurand induced shift in the peak wavelength of each grating and the individual internal grating spectral structure with high resolution. Figure 5.8 displays the measurements obtained for the Bragg wavelength of the 1549 nm grating under temperature modulation over the range 20°C to 95°C using both the single and over-mode HeNe reference beams. The measurements indicate clear evidence of the quadratic dependence of the Bragg wavelength on temperature (Figure 5.9) as has been reported recently [34]. The linear fit is also included to illustrate the potential measurement error associated ($\pm \sim 8$ pm) with linear fitting schemes.

For all of the temperature readings in this range, the peak spectral wavelengths, measured using the two different references, are equal to one another within the spectral resolution of the Fourier transformation.

Intra-grating Spectral Measurements

Figure 5.10 shows the measurements of the spectral structure of the array gratings displaying 10 pm resolution. Again, all measurements are identical within the limits of the Fourier transformation. To demonstrate the effectiveness of the approach in a

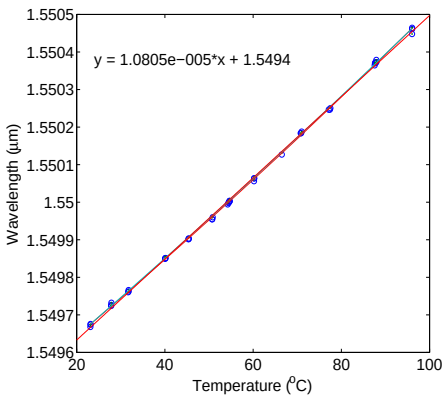

Figure 5.8: 1549 grating under temperature modulation

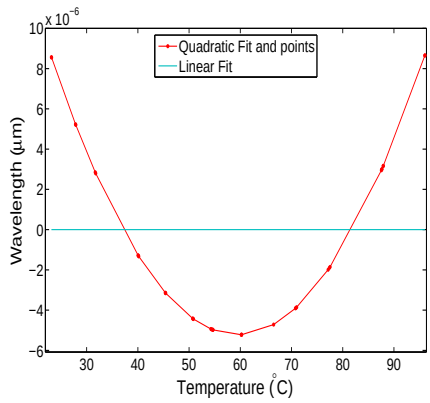

Figure 5.9: Quadratic dependence of Bragg wavelength to temperature.

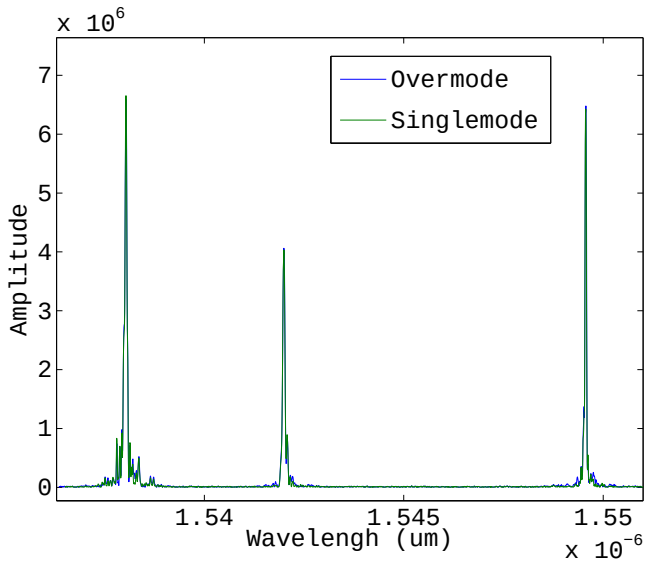

Figure 5.10: Comparison of spectral detail recorded using singlemode and overmode beams

more complex spectral case, a non-uniform temperature gradient is introduced across the 1538 nm grating. This produces a chirp, which broadens the grating's linewidth from ~ 50 pm to ~ 500 pm (Figure 5.11) To test the quality of the spectral measurements based on the over-mode reference beam, the 1549 nm grating was subjected to a similar non-uniform temperature gradient (Figure 5.12). As before, the effect is to broaden the grating linewidth and to distort its spectrum. Spectral measurements are performed using a 240 mm OPD, yielding 10 pm resolution. The arrangement of Figure 5.2 allows capture of both the composite (Bragg and over-mode HeNe) and the single-mode reference beams. Direct comparison of the grating spectra measured for

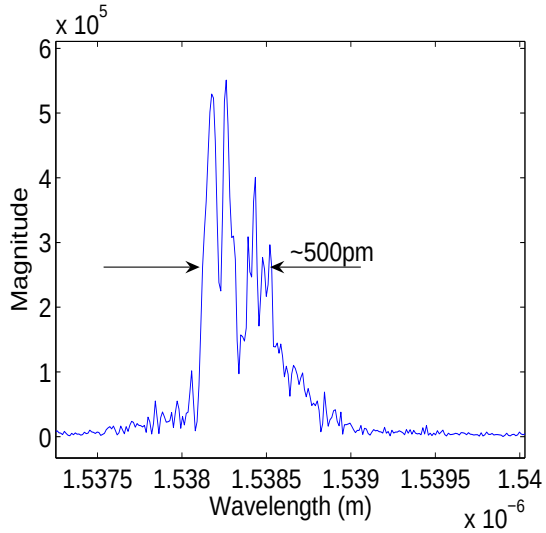

Figure 5.11: 1538 nm grating with induced chirp

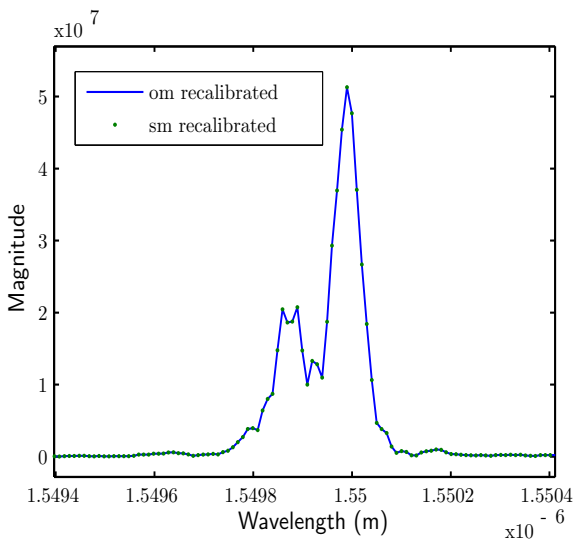

Figure 5.12: Comparison of spectral detail of chirp recorded using singlemode and overmode beams

the single-mode reference and the over-mode reference (Figure 5.12) indicate that, in this case also, the spectral measurements coincide across the full grating bandwidth, within the measurement resolution of the Fourier transformation.

5.4.1 Discussion

OPD Calibration

The experimental work conducted in chapter 4 demonstrated the efficacy of HTT

processing for delay calibration using a multiple transverse mode HeNe beam propagating through the fibre. The work in this chapter uses a multiple transverse mode reference beam as before, with mode stripping of the higher order modes through the 1550 nm coupler, to ensure collinearity of the measurand and reference beams propagating in the interrogating interferometer.

The advantage of beam collinearity for demodulation of the Bragg grating array which eliminates the largest source of uncertainty in interferometric systems referenced by a co-propagating reference beam [28] [30], (cf. chapter 4.4.2) are utilised in the experimental configuration reported here (Figure 5.2). The use of a single photodiode to capture both the reference and grating interferograms reduces the number of components. A second optical detector and associated electronics are not now required in the demodulation scheme. Such a scheme also allows for higher data acquisition rates because of the reduced requirement of sampling a single channel on the data acquisition card. Higher data acquisition rates mean that higher translation speeds are possible when scanning the interferometric delay, thus reducing the scanning time necessary to achieve high resolution.

Previous applications of co-linearly launched reference and measurand beams have either used a zero-crossing detection circuit [30] or non-mechanically scanned delay [35]. In the work reported in this chapter, HTT processing for delay calibration, conducted entirely in software, is applied to a mechanically scanned Michelson interferometer to provide high resolution measurement of the individual gratings in the array.

Fellgett Advantage

Hilbert transform processing has been reported [13,28,30,34,35] to provide high resolution measurement of the reflected wavelength of the individual gratings in an array for far shorter OPD scans. The technique is based on a comparison of the temporal phases ($\phi = \omega\tau$)of the reference and measurand beams which provides measurement of the mean reflected wavelength from the gratings but without measurement of the

spectral detail of the individual gratings in the array.

The Fellgett advantage of FTS [12] is exploited in this work for both the separation of the measurand and reference beams, and the separation of the individual gratings in the array. The capability of the interferometric Fourier transform spectrometer (Figure 5.2) to provide the high resolution required for measurement of the intra-grating spectral detail is illustrated in Figure 5.11. The spectral broadening results in a total wavelength shift (Figure 5.11) of ~ 500 pm at a sensitivity of ~ 10 pm /°C would correspond to a 50°C change in temperature at the grating site.

Figure 5.7 illustrates a potential measurement range of ~ 900 nm. However, full realisation of this large range of wavelengths, or larger, using supercontinuum generation in PCF fibre would ideally require the use of endlessly singlemode PCF fibre throughout the interrogation unit.

Processing schemes based on phase comparison, such as the high resolution drift compensated scheme of Kersey *et al.* [36] implemented in Chapter 3, and the Hilbert transform spectroscopic technique reported by Flavin *et al.* [37], would return a mean value for this temperature range at the grating site.

Quadratic Dependence of the Bragg Wavelength

The quadratic behavior of the Bragg grating temperature coefficients has previously been reported over a temperature range of −70 to +80°C by Flockhart *et al* [34] as introducing a measurement deviation from linearity of ~ 35 pm or ~ 3.5^{o}C. One of the processing schemes used for wavelength demodulation was the Hilbert transform technique [13, 28] which provides higher resolution wavelength demodulation for shorter delay scans. The experimental measurements shown in Figures 5.8 and 5.9 again illustrate this quadratic dependence, with a deviation from linearity of ~ ±7 pm or ~ 0.7°C assuming a thermal response of ~ 10 pm/°C. Sensing systems which ignore the second order term limits the measurement accuracy over the range 20°C to 95°C to ~ ±0.7°C or ~ ±7$\mu\epsilon$.

5.5 Conclusion

This work has demonstrated the capability of **long-scan** IFTS (240 mm OPD), and the associated Hilbert transform technique for OPD calibration, for interrogation of FBG sensor arrays. The configuration provides simultaneous recovery of spectral detail of all gratings in the array. All measurements are achieved in a single scan of the OPD from an interferogram captured on a single InGaAs photodiode. OPD calibration and absolute wavelength calculation is based on referencing to a transversely multimode HeNe laser propagating through 1550 nm fibre, providing identical measurements within the wavelength resolution of the Fourier transform.

The performance of the transversely multi-mode reference, where the higher order modes have been suppressed using a 50/50 coupler, relative to a single mode reference, has been evaluated in the context of temperature sensing and in the context of high resolution intra-grating spectral measurement providing identical measurements, again within the limits of the resolution of the Fourier transform. The error to the quadratic fit over the temperature range for the five scans plotted at each temperature is $\pm \sim 10$ pm, corresponding to a temperature resolution of ~ 1 °C for both references.

The customised Michelson interferometer applied to the work reported here uses retro-reflectors and mirrors to recombine the beams to produce the interferogram. The combination of the retro-reflectors and the mirrors, although shortening the length of translation stage required to provide high resolution FTS measurements, remains bulky and unsuitable for portable systems. The work reported in the next chapter will apply the Hilbert transform technique of Flavin *et al.* [13] to OPD calibration and Bragg wavelength interrogation on a more portable all-fibre design. This design will also allow for higher OPD scanning speeds than those achieved with the customised Michelson interferometer reported in this chapter (~ 3 mm/s).

References

[1] S. Abbenseth and S. I. Lochmann, "Distinct Enlargement of Network Size or Measurement Speed for Serial FBG Sensor Networks Utilizing SIK-DS-CDMA," *Journal of Physics Conference Series*, vol. 15, pp. 149–154, 2005.

[2] J. Mandal, T. Sun, K. T. V. Grattan, R. T. Zheng, N. Q. Ngo, and A. T. Augousti, "A parallel multiplexed temperature sensor system using Bragg-grating-based fiber lasers," *IEEE Sensors Journal*, vol. 6, pp. 986–995, August 2006.

[3] B. Lee, "Review of the Present Status of Optical Fibre Sensors," *Optical Fibre Technology*, vol. 9, no. 2, pp. 57–59, 2003.

[4] W. J. Wadsworth, A. Ortigosa-Blanch, J. C. Knight, T. A. Birks, T. P. M. Man, and P. S. Russell, "Supercontinuum Generation in Photonic Crystal Fibers and Optical Fibre Tapers: A Novel Light Source," *Journal of the Optical Society of America B-Optical Physics*, vol. 19, no. 9, pp. 2148–2155, 2002.

[5] J. K. Ranka, R. S. Windeler, and A. J. Stenz, "Visible Continuum Generation in Air Silica Micro Structure Optical Fibres with Analomous Dispersion at 800 nm," *Optics Letters*, vol. 25, pp. 25–27, January 2000.

[6] L. A. Ferreira, E. V. Diatzikis, J. L. Santos, and F. Farahi, "Frequency modulated multimode laser diode for fibre Bragg grating sensors," *Journal of Lightwave Technology*, vol. 16, pp. 1620–1630, September 1998.

[7] K. Peters, P. Pattis, J. Botsis, and P. Giaccari, "Experimental verification of response of embedded optical fiber Bragg grating sensors in non-homogeneous strain fields," *Opticas and Lasers in Engineering*, vol. 33, pp. 107–109, 2000.

[8] A. Arie, B. Lissak, and M. Tur, "Static fiber Bragg grating strain sensing using frequency locked lasers," *Journal of Lightwave Technology*, vol. 17, pp. 1849–1855, October 1999.

[9] C. Boulet, D. J. Webb, M. Douay, and P. Niay, "Simultaneous interrogation of fiber Bragg gratings using an acousto-optic tunable filter," *IEEE Photonics Technology Letters*, vol. 13, pp. 1215–1217, November 2001.

[10] M. G. Xu, H. Geiger, J. L. Archembault, L. Reekie, and J. P. Dakin, "Novel interrogating system for fibre Bragg grating sensors using an acousto-optic tunable filter," *Electronics Letters*, vol. 29, pp. 1510–1511, August 1993.

[11] Y.-J. Rao, D. J. Webb, D. A. Jackson, L. Zhang, and I. Bennion, "In fiber Bragg grating temperature sensor system for medical applications," *Journal of Lightwave Technology*, vol. 15, pp. 779–785, May 1997.

[12] J. Goodman, *Statistical Optics.* New York: John Wiley & Sons, 1985.

[13] D. Flavin, R. McBride, and J. D. C. Jones, "Short-Scan Interferometric Interrogation and Multiplexing of Fibre Bragg Grating Sensors," *Optics Communications*, vol. 170, no. 4-6, pp. 347–353, 1999.

[14] S. Huang, M. LeBlanc, M. M. Ohm, and R. M. Measures, "Bragg intragrating structural sensing," *Applied Optics*, vol. 34, no. 22, pp. 5003–5009, 1995.

[15] H.-N. Li, D.-S. Li, and G.-B. Song, "Recent Applications of Fiber Optic Sensors to Health Monitoring in Civil Engineering," *Engineering Structures*, vol. 26, pp. 1647–1657, 2004.

[16] I. Riant, "Fiber Bragg gratings for optical telecommunications," *Comptes Rendus Physique*, vol. 4, pp. 41–49, 2003.

[17] G. Meltz, W. W. Morey, and W. H. Glenn, "Formation of Bragg Gratings in Optical Fibres by a Transverse Holographic Method," *Optics Letters*, vol. 14, pp. 823–825, 1989.

[18] J. Albert, K. O'Hill, B. Malo, S. Theriault, F. Bilodeau, D. C. Johnson, and L. E. Erickson, "Apodisation of the spectral response of fibre Bragg gratings using a phase mask with variable diffraction efficiency," *Electronics Letters*, vol. 31, pp. 222–223, February 1995.

[19] L. Dong, J. L. Archambault, L. Reekie, P. S. J. Russell, and D. N. Payne, "Single pulse Bragg gratings written during fibre drawing," *Electronics Letters*, vol. 29, pp. 1577–1578, August 1993.

[20] A. Martinez, M. D. I. Khrushchev, and I. Bennion, "Direct writing of fibre Bragg gratings by femtosecond laser," *Electronic Letters*, vol. 40, pp. 1170–1172, September 2004.

[21] K. O. Hill and G. Meltz, "Fiber Bragg Grating Technology: Fundamentals and Overview," *Journal Of Lightwave Technology*, vol. 15, pp. 1263–1276, August 1997.

[22] R. Kashyap, *Fibre Bragg Gratings.* Optics and Photonics, Academic Press, 1999.

[23] T. Erdogan, "Fiber Grating Spectra," *Journal of Lightwave Technology*, vol. 15, pp. 1277–1294, August 1997.

[24] A. D. Kersey, M. A. Davis, H. J. Patrick, M. LeBlanc, K. P. Koo, C. G. Askins, M. A. Putnam, and E. J. Friebele, "Fibre Grating Sensors," *Journal of Lightwave Technology*, vol. 15, no. 8, pp. 1442–1463, 1997.

[25] M. LeBlanc, S. Y. Huang, M. Ohn, and R. M. Measures, "Distributed strain measurement based on a fiber Bragg grating and its reflection spectrum analysis," *Optics Letters*, vol. 21, pp. 1405–1407, September 1996.

[26] Y.-J. Rao, "In-fibre Bragg grating sensors," *Meas. Sci. Technol.*, vol. 8, pp. 355–375, 1997.

[27] M. Davis and A. Kersey, "Application of a Fibre Fourier Transform Spectrometer to the Detection of Wavelength Encoded Signals from Bragg Grating Sensors," *Journal of Lightwave Technology*, vol. 13, no. 7, pp. 1289–1295, 1995.

[28] K. B. Rochford and S. D. Dyer, "Demultiplexing of Interferometrically Interrogated Fiber Bragg Grating Sensors Using Hilbert Transform Processing," *Journal of Lightwave Technology*, vol. 17, no. 5, pp. 831–836, 1999.

[29] S. L. Hann, *Hilbert Transforms in Signal Processing.* No. ISBN: 0-89006-886-0, Artec House, 1996.

[30] S. D. Dyer, P. A. Williams, R. J. Espejo, J. D. Kofler, and S. M. Etzel, "Fundamental limits in fiber Bragg grating peak wavelength measurements," in *Proceedings of SPIE* (M. Voet, R. Willsch, W. Ecke, J. Jones, and B. Culshaw, eds.), vol. 5855, (Bellingham, WA.), pp. 88–93, SPIE, 2005.

[31] T. Usuki, Y. Sakuma, S. Hirose, K. Takemoto, N. Yokoyama, T. Miyazawa, M. Takatsu, and Y. Arakawa, "Single-photon generator for optical telecommunication wavelength," *Journal of Physics: Conference Series*, vol. 38, pp. 140–143, 2006.

[32] J. H. Rothwell and D. A. Flavin, "Dispersion Measurement by White Light Interferometry Based on Fresnel Reflections," in *CLEO-Europe*, (Munich, Germany), 2002.

[33] G. P. Brady, K. Kalli, D. J. Webb, L. Reekie, and J. L. Archambault, "Simultaneous measurement of strain and temperature using the first and second order diffraction wavelengths of Bragg gratings," *Optoelectronics, IEE Proceedings*, vol. 144, pp. 156–161, June 1997.

[34] G. M. Flockhart, R. R. J. Maier, J. S. Barton, W. N. MacPherson, J. D. C. Jones, K. E. Chisholm, L. Zhang, I. Bennion, I. Read, and P. D. Foote, "Quadratic behaviour of fibre Bragg grating temperature coefficients," *Applied Optics*, vol. 43, no. 13, pp. 2744–2751, 2004.

[35] D. F. Murphy, D. A. Flavin, R. McBride, and J. D. C. Jones, "Interferometric interrogation of in-fiber Bragg grating sensors without mechanical path length scanning," *Journal of Lightwave Technology*, vol. 19, pp. 1004–1009, July 2001.

[36] A. D. Kersey and T. A. Berkoff, "Fiber-optic Bragg grating strain sensor with drift-compensated high-resolution interferometric wavelength-shift detection," *Optics Letters*, vol. 18, pp. 72–74, January 1993.

[37] D. A. Flavin, R. McBride, and J. D. C. Jones, "Short Optical Path Scan Interferometric Interrogation of a Fibre Bragg Grating Embedded in a Composite," *Electronic Letters*, vol. 33, 1997.

Chapter 6

High Speed Bragg Grating Sensor Array Demodulator for Structural Health Monitoring

6.1 Introduction

Structural health monitoring (SHM) is a recent and rapidly growing area of optical metrology [1–6]. SHM involves the routine measurement and analysis of key parameters of a structure's operating conditions, such as stress, temperature and displacement, to provide advance warning of impending abnormal states or failures and provide maintenance advice.

Fibre Bragg gratings (FBG) have been implemented in various capacities in advanced sensing [6–10]. A particular feature of FBGs is that the measurand is directly encoded in the reflected wavelength, which is an absolute parameter and does not suffer from disturbances of the light path i.e. connector or bend loss. Research into the application of these sensors within intelligent structures which can return information on parameters such as strain and temperature is ongoing [11–13].

The development of the phase mask technique for grating inscription [14] and the rising demand for gratings has seen a dramatic reduction in the cost of production. Side writing techniques also allow for inscription of gratings with centre wavelengths far removed from the wavelength of the inscribing laser. This technique makes them ideal for use in cheaper, mass produced telecom fibres, and allows tailoring of the gratings resonant wavelength, making them ideal for wavelength division multiplexing (WDM).

However, the cost of sensor interrogation systems remains high and ease of imple-

mentation of WDM schemes using established approaches to sensor demodulation — tunable laser [15–18], tunable filter [19–21], diode arrays [22] — can be prohibitive. The next step towards commercialisation of fibre Bragg grating based sensors in the field of structural health monitoring has to be capable of producing high speed, high resolution demodulation of all gratings in a serially multiplexed array. The potential ability for demodulation of grating arrays over extended wavelength ranges, ~ 900 nm, from a single interferogram obtained on a single InGaAs photodiode was demonstrated in chapter 5. However, the long OPD scans required to obtain high resolution measurement took ~ 1 minute to capture on the bulk optic interferometer.

The inherently fibre-coupled return signals from an FBG array are directly compatible with a fibre implementation of a Fourier transform spectrometer. For applications which require the use of arrays of sensors, such as structural health monitoring, interferometric Fourier transform interrogators take simultaneous measurements of all sensors in the array in a single scan. The development of an all-fibre grating referenced demodulator will provide the advantages of:

- A reduction in the number of bulk optic components in the demodulation scheme and obviate the need for a reference laser which will decrease the potential cost and size of the system, thereby increasing the portability of the demodulator.
- Allow ~ kHz interrogation. The delay scan in an all-fibre interferometer is executed by stretching the fibre in one arm. Commercially available piezoelectric fibre stretchers, which are based on the inverse piezoelectric effect are capable of ~ kHz delay scanning, as the acceleration and velocity of the stretcher are not limited by rotational inertia.

6.1.1 Hilbert Transform Spectroscopy

The principle of Fourier transform spectroscopy is that the oscillatory component of the interferogram formed by scanning the interferometric optical path difference (OPD), τ, in a two beam interferometer yields the real part of the self coherence func-

tion of the light illuminating the interferometer. This function exhibits a Fourier relationship to the normalised power spectrum of the illuminating source [23] allowing direct determination of the power spectrum from the magnitude of the Fourier transform of the interferogram and was discussed in Section 2.2.7.

The potential of interferometric spectroscopy, implemented as Fourier transform spectroscopy, to demodulate serial arrays of fibre Bragg grating arrays over extended wavelength ranges has been demonstrated in Chapter 5. High resolution measurement of the mean wavelength reflected from a fibre Bragg grating is required for sensing of temperature and strain. The measurement of intra-grating spectral detail, which could be valuable in the detection of non-uniform measurand fields within the grating [24], however, requires long optical path difference scans [25], as described in Section 2.2.9.

The implementation of IFTS using the Hilbert transform technique exhibits an advantage over conventional methods of application in that far shorter OPD scans are required to provide high resolution measurement of the mean reflected wavelengths from an array of fibre Bragg gratings [26]. The theory relating to high resolution spectroscopic measurements using the Hilbert transform technique is detailed below.

The complex signal associated with a real signal, where the imaginary part is the Hilbert transform of the real part is known as the analytic signal (cf. Section 2.2.12). The analytic signal is a generalisation of the phasor from which the amplitude, A(τ), and phase, $\phi(\tau)$ can be calculated from

$$A(\tau) = \sqrt{x(\tau)^2 + y(\tau)^2} \tag{2.2.45}$$

and

$$\phi(\tau) = tan^{-1}\left[\frac{Im[A(\tau)]}{Re[A(\tau)]}\right] \tag{2.2.46}$$

Spectroscopic analysis of the component of light reflected by a Bragg grating, λ_B, is based on high resolution measurement of the phase of the complex analytic signal. The analytic signal obtained from a multiplexed array of fibre Bragg gratings is given by a superposition of signals due to the individual gratings which may be written as

$$A_j(\tau) = \sum_j A(\tau) \tag{6.1.1}$$

Once the analytic signal has been obtained, it is then linearly interpolated to calculate the delay, τ, between the interferometer arms, as measurement accuracy is compromised by non-uniform sampling of τ. The intensity of the beam at the output of the interferometer can be represented as a function of the delay between the interferometer arms

$$I_j(\tau) = A_j(\tau) cos(\omega_j \tau + \xi_j) \tag{6.1.2}$$

where ω_j and ξ_j are the frequency and initial phase terms respectively and $A_j(\tau)$ are slowly varying functions of τ.

The signal phases can be written as

$$\phi_j(\tau) = \omega_j \tau + \xi_j \tag{6.1.3}$$

The individual phase functions cannot be extracted directly from the composite signal. After OPD calibration, the individual components from the gratings will be represented by resolvable sharp peaks in the power spectrum. This allows frequency domain filtering of the individual signals reflected from each individual grating in the array. These peaks are individually windowed and an inverse FFT taken of the appropriate windowed section. The resulting analytic signal is due to a single grating and the corresponding phase can be written as:

$$\phi_B(\tau) = \omega_B \tau + \xi_B \tag{6.1.4}$$

The ratio of the optical frequencies of the measurand and reference gratings is equal to the gradient of the graph $\phi_{BS}(\tau)$ against $\phi_{BR}(\tau)$ and is defined as:

$$\eta_{BS,BR} \equiv \frac{d\phi_{BS}}{d\phi_{BR}} = \frac{\omega_{BS}}{\omega_{BR}} \tag{6.1.5}$$

where the subscripts BS and BR refer to the sensing and reference gratings respectively,

The ratio of the grating centre wavelength to reference wavelength is just the inverse of this

$$\frac{\lambda_{BS}}{\lambda_{BR}} = \frac{\omega_{BR}}{\omega_{BS}} \tag{6.1.6}$$

and hence,

$$\lambda_{BS} = \frac{\lambda_{BR}}{\eta_{BS,BR}} \tag{6.1.7}$$

Therefore, each gratings mean wavelength, λ_i, can be found by unwrapping the phase and finding the gradient,

$$\omega_i = \frac{d\phi_i}{d\tau} \tag{6.1.8}$$

6.1.2 Experimental Motivation and Objectives

The Hilbert transform technique for correction of spectral degradation acquires N samples of the reference and measurand interferogram and corrects based on this sampling rate. This requires long processing times for interpolation of long OPD scans. The interrogation of FBG arrays can be achieved via processing using the Hilbert transform technique based on comparison of the temporal phase vector obtained from a reference interferogram and that obtained from the array of gratings. This technique has been shown to generate higher measurement accuracy, $\sim 5\ pm$, for shorter OPD scans, $\sim 1.2\ mm$, but without yielding measurement of the spectral content of the individual gratings in the array [26].

The objectives of the work reported in this chapter are to:

- develop an all-fibre interferometric demodulator capable of high speed grating

demodulation where the mean reflected wavelengths from the individual gratings in an array are obtained via processing using the Hilbert transform technique based on a reference interferogram obtained from a reference Bragg grating. The resultant analytic signal allows determination of a phase vector for each of the individual gratings in the array by separation of the individual spectra in an intermediate processing step. The mean reflected wavelength is then obtained from the ratio of the reference and measurand phases.

- evaluate the performance of a grating reference relative to that of a laser reference of highly stable mean wavelength for grating array interrogation in the context of temperature and strain sensing.

6.2 Experimental Configuration

Light from a 1550 nm broadband source, Optospeed superluminescent diode (SLED), is launched through a 1550 nm 50/50 coupler, DC1, and is divided to follow two paths (Figure 6.1): one output arm of the coupler is spliced to a temperature stabilised, low reflectivity, narrow linewidth (~ 40 pm), reference Bragg grating and the other arm is spliced to a sensing array of fibre Bragg gratings. The light reflected from the reference grating and the sensor array propagates back through the coupler to an all-fibre Michelson interferometer via a second 1550 nm 50/50 coupler, DC2. One arm of the Michelson interferometer contains a piezo-electric stretcher to scan the interferometric optical path difference. Both arms contain Faraday rotation mirrors for polarisation control. The light reflected from the Faraday rotation mirrors propagates back through coupler DC2 to form a composite interferogram, which is directed to two photodetectors via coupler DC3. The tunable filter passes the light from the reference Bragg grating only to the photodetector for use as a reference signal. The interferograms captured by both photodetectors are then acquired by a PC for processing.

In general, a sawtooth waveform is applied to piezoelectric scanning units [27]. However, a drawback of driving the unit with this type of waveform is that the inter-

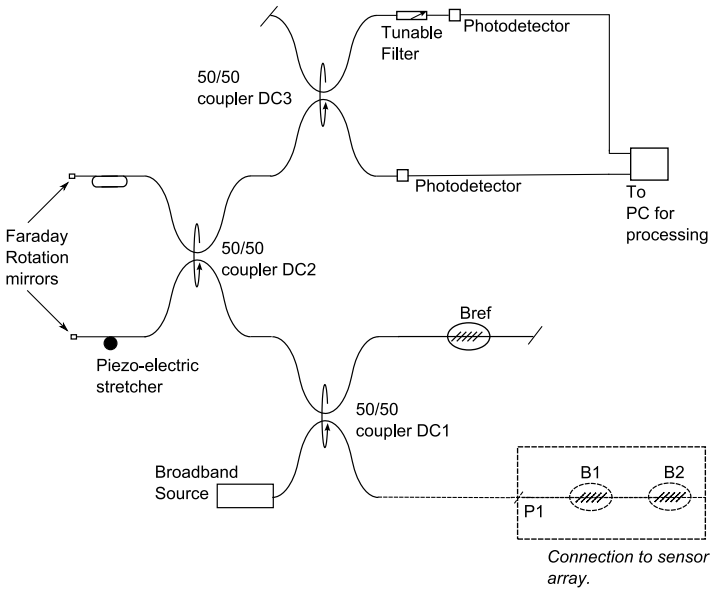

Figure 6.1: All-fibre demodulator for structural health monitoring.

ferogram generated in the flyback leg of the scan is discarded. The interferometric OPD in the work reported here is scanned by applying both a sinusoidal waveform and a triangular (quasi-sawtooth) waveform from a signal generator to the piezo-electric stretcher. The advantage of the sinusoidal waveform is that both interferograms can be used for processing, and also that higher scanning frequencies can be achieved with the piezoelectric stretcher. The total OPD generated by the stretcher is dependent on the frequency and form of the signal applied by the generator. The frequency response of a triangular/sawtooth waveform is limited by the driver to 10 Hz at full amplitude sweep and falls off approximately linearly to 0 at ~ 1 kHz, with higher responses available depending on the waveform applied.

However, the scanning rate of the interrogator in this case is limited by the maximum sampling rate (250 kS/s) of the data acquisition card (National Instruments PCI-6023E) in the PC, allowing a maximum sampling rate of 125 kS/s per channel in the system reported here. A 0.5 Hz signal is applied to provide a full amplitude OPD scan of the interferometer (~ 8 mm).

The sensing array consists of 2 fibre Bragg gratings, with room temperature resonant wavelengths of 1538 nm and 1550 nm. The reference gratings resonant wave-

length was 1566.46 nm. The tunable filter was set to filter the components due to the sensor gratings.

6.3 Results and Discussion

6.3.1 Results

Reference Grating Measurement Repeatability

The measurement repeatability of both a grating reference and a highly stable 1534 nm telecoms laser reference were compared by applying a near sawtooth (pulsed) waveform, c.f. Figure 6.2, to drive the piezoelectric controller to scan the OPD over the full amplitude sweep of the stretcher. The resulting interferograms obtained from the all-

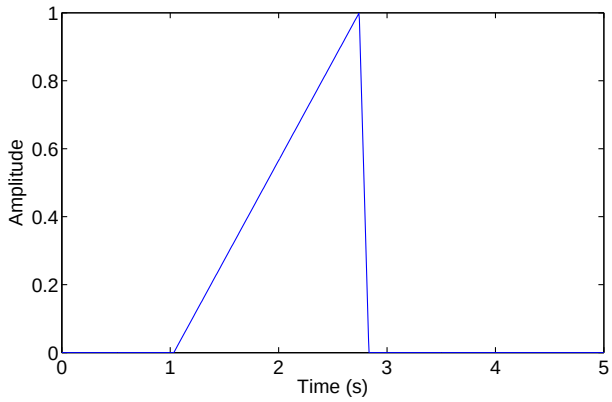

Figure 6.2: Pulsed sawtooth waveform applied to drive the piezoelectric controller.

fibre interferometer are shown in Figure 6.3. The low frequency fringes visible in the interferogram are those generated on the flyback leg of the quasi-sawtooth waveform, where there is a time lag between the applied signal and the relaxation of the fibre. The interferograms obtained on the flyback leg are discarded due to the varying fringe frequency caused by by an initial rapid relaxation of the fibre followed by a much slower settling velocity. The interferograms are Hamming windowed prior to Fourier transform processing to obtain the analytic signals. New delay values are obtained from the unwrapped phase vector and the interferograms are interpolated to distribute them evenly in delay as described previously in Section 2.2.9.

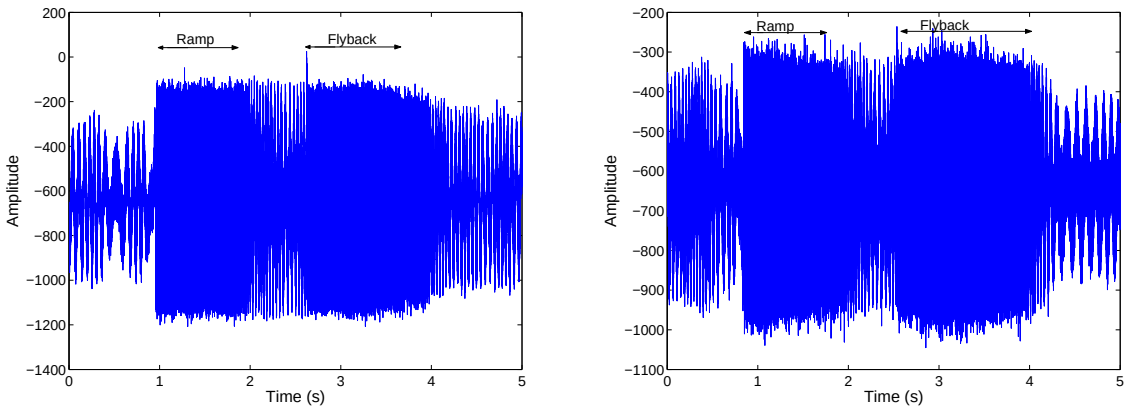

(a) Reference laser interferogram.

(b) Reference grating interferogram.

Figure 6.3: Interferograms obtained from the reference laser and reference grating using a saw-tooth waveform applied to the demodulator of Figure 6.1

The extent of the non-uniform scanning velocity of the piezo-electric stretcher can be seen in the residuals to the unwrapped phase vector (Figure 6.4). Before OPD re-calibration is carried out the total excursion is ~ 500 rad, and after the total excursion is < 0.01 rad.

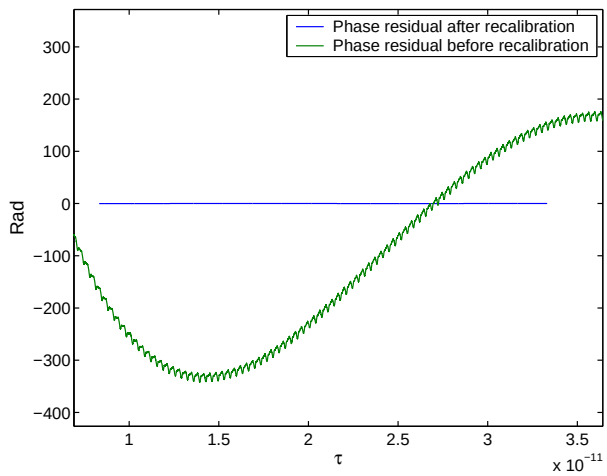

Figure 6.4: Phase residuals before and after recalibration

Spectral Measurements

Figure 6.5 displays the spectral measurements of the reference grating and reference laser. The self referenced spectra (blue and red lines) are those obtained from OPD calibration based on the temporal phase vectors of filtered interferograms using the

tunable filter. The remaining spectra are those obtained by processing the compos-

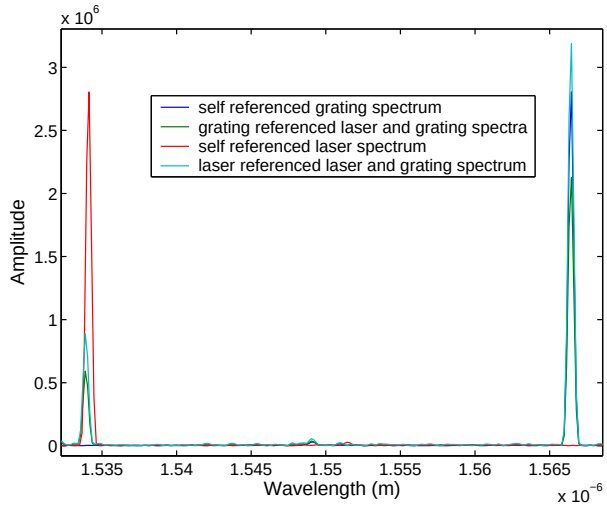

Figure 6.5: Comparison of spectral measurements obtained using both a laser and grating reference

ite interferograms containing both reference grating and laser frequencies. The composite interferograms are referenced from both the filtered grating and laser interferograms. The spectral measurements from the composite interferograms are identical within the resolution of the Fourier transform, ~ 286 pm for an 8.4 mm OPD scan (the relative intensities in Figure 6.5 have been modified for display purposes).

Hilbert Transform Spectroscopic Measurements

The reference grating used for the above spectral measurements was temperature stabilised by submersion in a beaker of water at room temperature. The water temperature was monitored using thermocouples, and was stable to ± ~ 0.1 °C. The wavelength stability of the reference grating is compared to the stability of a 1534 nm telecom laser in Figure 6.6. The stability of the 1534 nm laser is quoted at < 1 pm over a period of 24 hours. A residual to a fit to the recorded wavelengths (Figure 6.6) shows that over the 14 scans taken there is ± ~ 0.9 pm variation in the wavelength of the reference grating over the duration of the experiment. The total OPD of the scans is

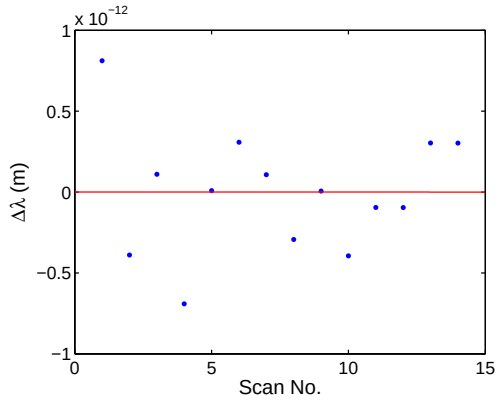

Figure 6.6: Residual to a fit to the recorded resonant wavelength of the reference grating referenced from a highly stable (< 1 pm) 1534 nm telecoms laser

calculated to be 8.4 mm and is obtained from the extracted phase vector according to

$$\Delta_{OPD} = \left[\frac{\phi_{max}}{2\pi}\right] \; x \; 1534.14x10^{-9}m \tag{6.3.1}$$

6.3.2 Application to the Single Parameter Sensing of Temperature

The interferogram generated by the array of gratings is illustrated in Figure 6.7. The interferogram generated from the flyback leg of the scan is discarded for processing. The sampling density corresponds to ~ 5 samples per fringe. The interferograms are

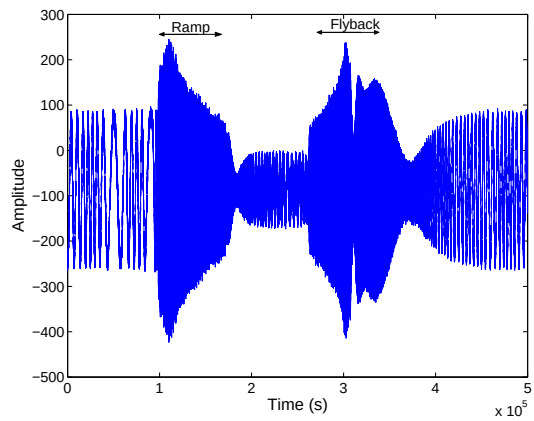

Figure 6.7: Interferogram obtained from the grating array when a sawtooth waveform applied to the demodulator of Figure 6.1

processed as above, with the individual grating spectra being separated in the frequency domain after delay calibration. The analytic signal for each of the individual

gratings in the array can then be obtained, a temporal phase vector calculated for comparison with the reference phase vector, as described above (Section 6.1.1).

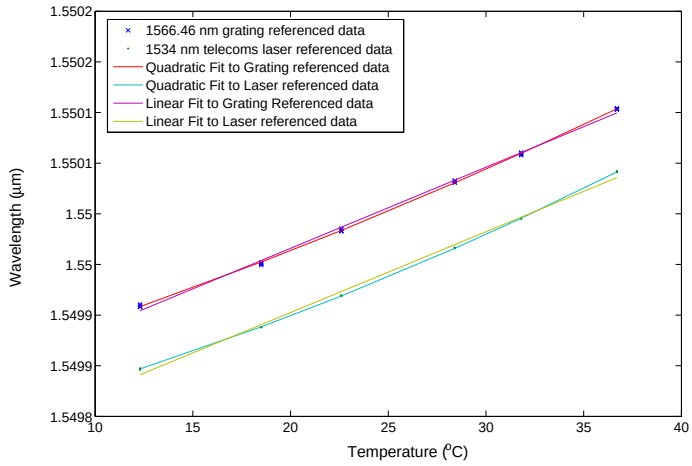

(a) Variation of Bragg wavelength with temperature

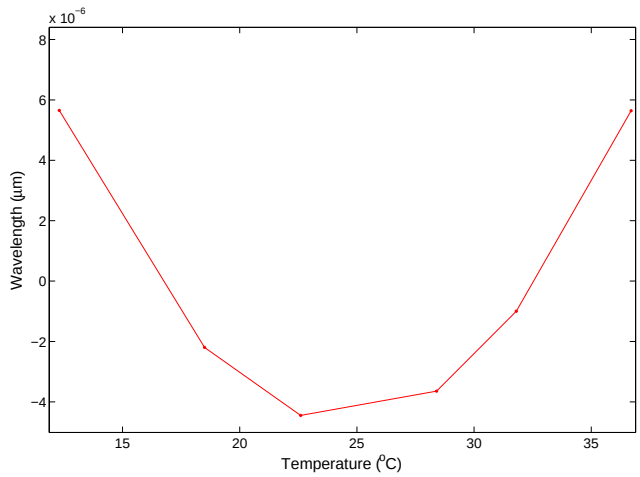

(b) Residual to a linear fit to the variation of Bragg wavelength with temperature

Figure 6.8: Results recorded by gratings subjected to a temperature change from ~ 20^oC - 50^oC referenced from a 1534.14 nm laser and from the 1566.46 nm grating.

Figure 6.8 illustrates the measurements made on the ~ 1550 nm grating when subjected to temperature changes from ~ 12^oC - 37^oC. The measurements displayed are obtained on the stretching leg of the interferometer. The slightly quadratic dependence of the resonant Bragg wavelength to temperature is evident when a residual to the linear fit to the temperature measurements is examined (Figure 6.8(b)).

The error over temperature range (quadratic fit) is ± 3 pm for the grating refer-

enced measurements and ± 1 pm for the telecom laser referenced measurements. The response of the grating to change in temperature obtained from the linear fit is ~ 8 pm /^{o}C. The difference in this value to the value reported in chapter 5 (~ 10 pm /^{o}C) is a consequence of the narrower temperature range, reducing the range of the quadratic dependence and therefore the slope of a linear fit.

Ignoring the quadratic term in the responsivity of the grating introduces an error of ~ ± 5 pm due to the deviation from linearity, corresponding to a limit in measurement accuracy of temperature of ~ ± 0.625 ^{o}C over the temperature range reported here. The error introduced by ignoring the quadratic term also increases as the temperature range is increased, as demonstrated in chapter 5, where ~ ± 7 pm error was reported.

Interferograms generated using a sinusoidal waveform applied to the piezo-electric stretcher

The sine wave applied to the demodulator is shown in Figure 6.9. The signal is DC offset to ensure that a positive voltage is applied to the piezoelectric stretcher at all times.

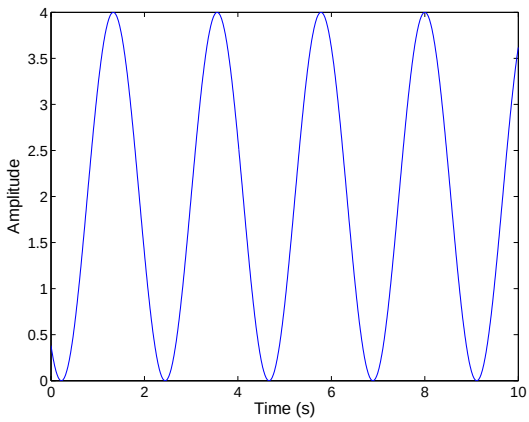

Figure 6.9: Sine wave applied to the piezoelectric stretcher to generate a series of interferograms.

A 10 second acquisition of the interferometric output as the interferometer is repetitively scanned over an OPD by the piezo-electric controller, driven by a sinusoidal signal generated by a signal generator, contains multiple interferograms as shown in

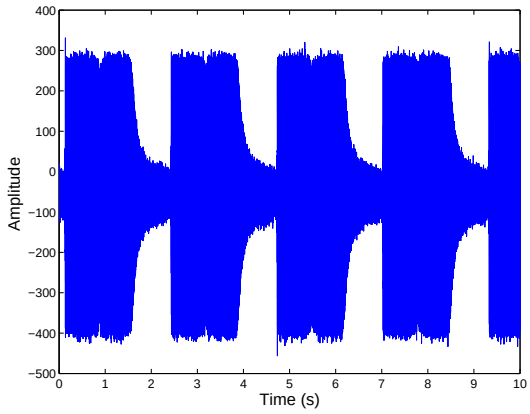

(a) Multiple reference interferograms obtained from a 10 second scan of the interferometer.

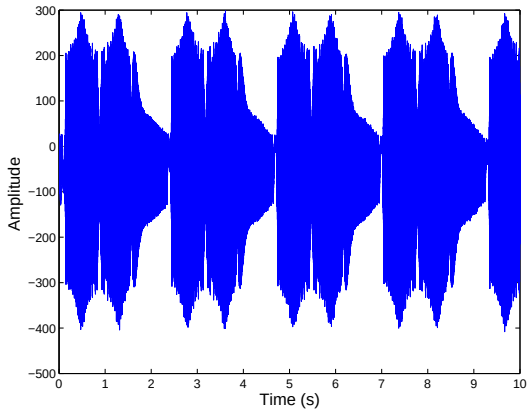

(b) Multiple measurand interferograms obtained from a 10 second scan of the interferometer.

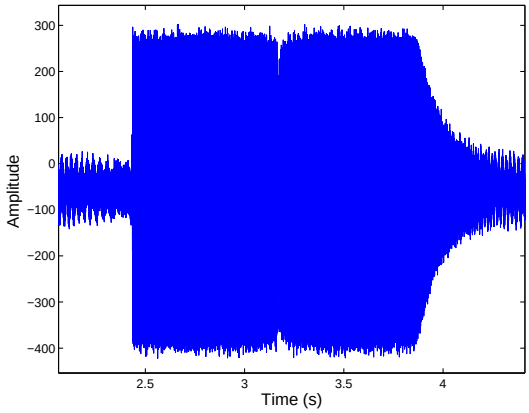

(c) Two reference interferograms obtained from a single sweep of the piezo-electric controller.

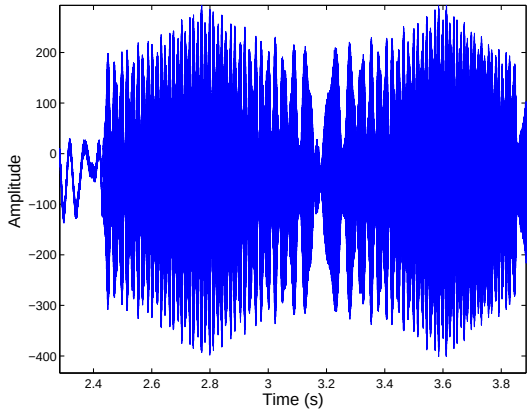

(d) Two measurand interferograms obtained from a single sweep of the piezo-electric controller

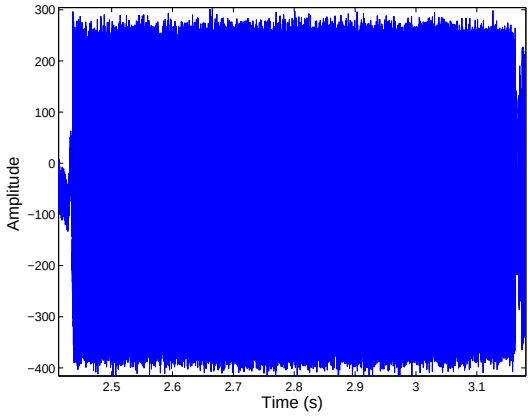

(e) Single reference interferogram for processing.

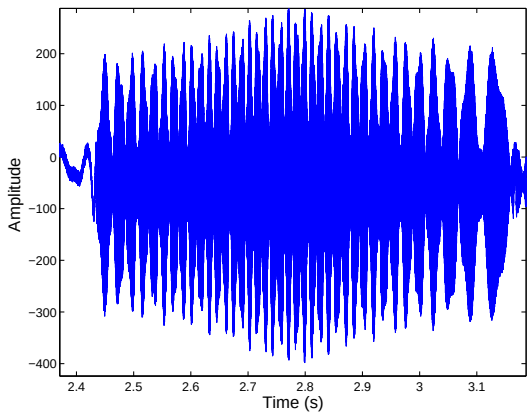

(f) Single measurand interferogram for processing.

Figure 6.10: All-fibre interferometer output with sinusoidal waveform applied to the piezoelectric stretcher.

Figures 6.10(a) - 6.10(b). The reference (grating) and measurand interferograms generated in a single sweep of the piezo-electric controller are shown in Figures 6.10(c) and 6.10(d) respectively. Both of the interferograms from the single sweep can be used for processing as opposed to the stretching leg only using the sawtooth waveform (cf. Section 6.3.1). Prior to processing one of the full interferogram is extracted from both the reference scan and the measurand/sensing scan (Figures 6.10(e) and 6.10(f)). The interferogram is then windowed using a Hamming window to remove any spurious spectral content in the Fourier transform.

Hilbert Transform Spectroscopy

An FFT is then performed on the windowed sections of the interferograms. The negative frequency and dc components of the spectrum are set to 0, which has the effect of multiplying by the Heaviside function (Equation 5.1.2). An inverse FFT is carried out to obtain the Hilbert transform of the original signal.

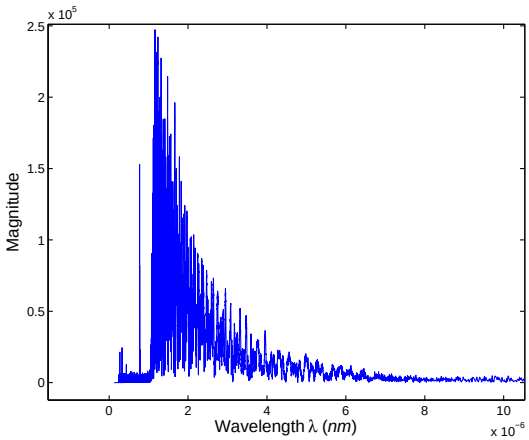

(a) Spectrum of the reference interferogram before OPD calibration.

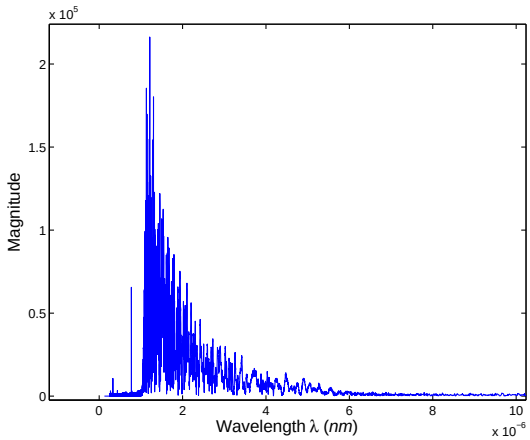

(b) Spectrum of the measurand interferogram before OPD calibration

Figure 6.11: Magnitude of the Fourier transforms of the measurand and reference interferograms

The extent of the spectral degradation in the all-fibre interferometer due to the stretching of the piezo-electric fibre stretcher can be seen in a plot of the spectrum obtained from the section of interferogram, as illustrated in Figures 6.11(a) - 6.11(b). The spectrum of the reference interferogram would be expected to show a single spike

at the reflecting frequency of the reference grating but as can be seen there is additional spectral content due to non-uniform sampling of the interfeometric OPD, τ.

The unwrapped phase is obtained from equation 2.2.46 and applying a Matlab unwrapping algorithm. Any non-uniformities in OPD sampling can then be corrected for.

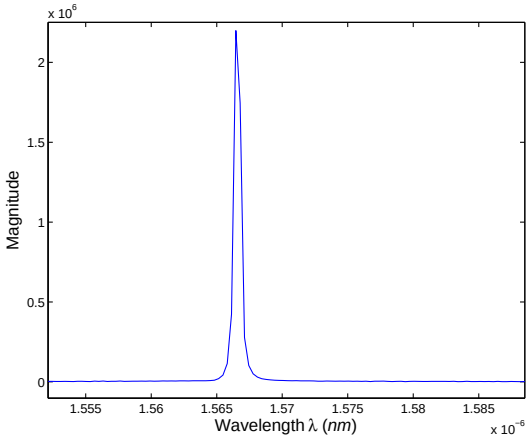

(a) Spectrum of the reference interferogram after OPD calibration.

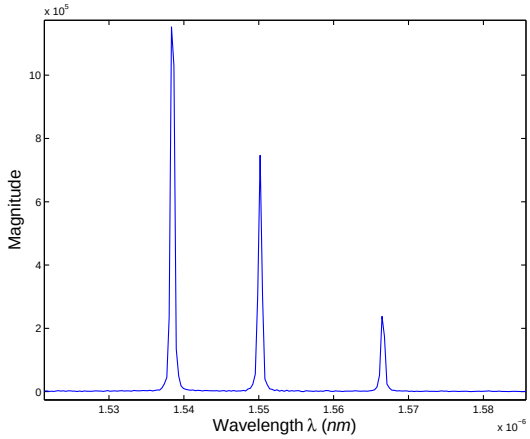

(b) Spectrum of the measurand interferogram after OPD calibration

Figure 6.12: Magnitude of the Fourier transforms of the measurand and reference interferograms after OPD calibration

The ability of the Hilbert transform for correction of spectral degradation is illustrated in Figures 6.12(a)-6.12(b). The spectrum of the reference grating is now a single spike centered at the reflecting wavelength of 1566.46 nm and the individual spectra of all gratings in the array obtained from the measurand interferogram are also clearly resolvable. The wavelength resolution of the Fourier transform (380 pm at 1550 nm) can be obtained using a plot of the unwrapped phase. The number of fringes in the processed component of the interferogram is easily extracted from the phase excursion of 25402 radians. In this case a total OPD of 6.3 mm or a stretching of 2.25 mm is achieved using the piezo-electric stretcher. The residuals to the phase before and after calibration illustrate the extent of the non-uniform sampling problem (Figure 6.13).

After re-sampling, a second FFT is performed on the interferogram. The individual spectra for all of the gratings are separated, which has the effect of removing the dc and negative frequencies. An inverse FFT is then performed to allow determination

of the phase for each grating from Equation 6.1.3. The mean grating wavelengths are determined by unwrapping the phase and finding the gradient, c.f. Equation 6.1.8.

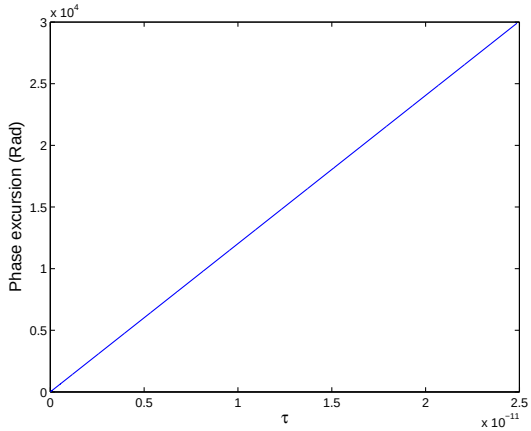

(a) Extracted phase vectors for the measurand and reference interferograms.

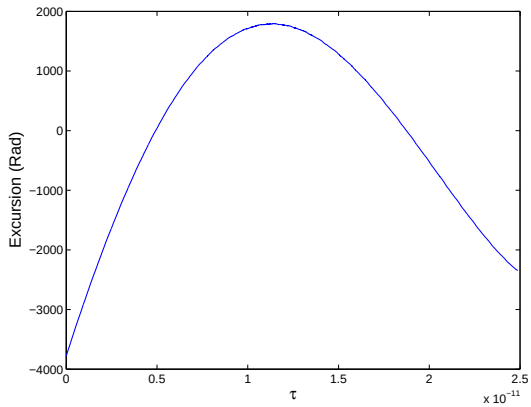

(b) Residual to the phase vectors illustrating the extent of the non-uniform velocity problem

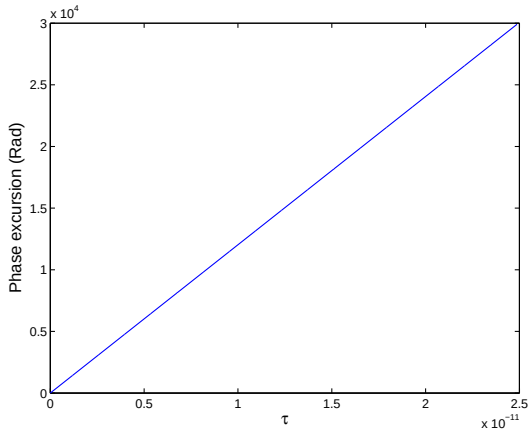

(c) Extracted phase vectors for the measurand and reference interferograms after OPD calibration.

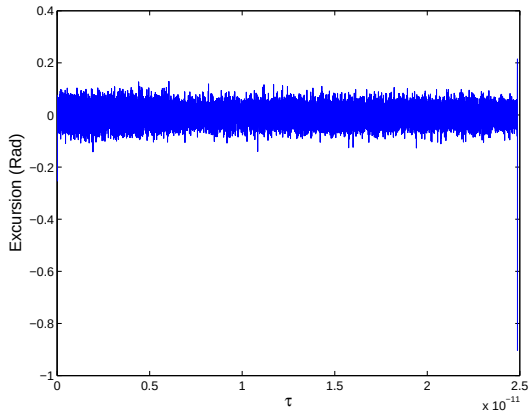

(d) Residual to the phase vectors after OPD calibration.

Figure 6.13: Unwrapped phase vectors and residuals

Application to Single Parameter Sensing of Temperature

The ability of the all-fibre demodulator for single parameter sensing of temperature is illustrated in Figure 6.14. The 1549 nm grating was cooled in an oven to $\sim 5^oC$ and the temperature increased to $\sim 88^oC$. The mean error over the temperature range is $\sim \pm 10$ pm, corresponding to a temperature resolution of $\sim \pm 1^o$C.

Calculation of the gradient of a fit to the temperatures in Figure 6.14 allows determination of the temperature dependent increase in the resonant wavelength of the

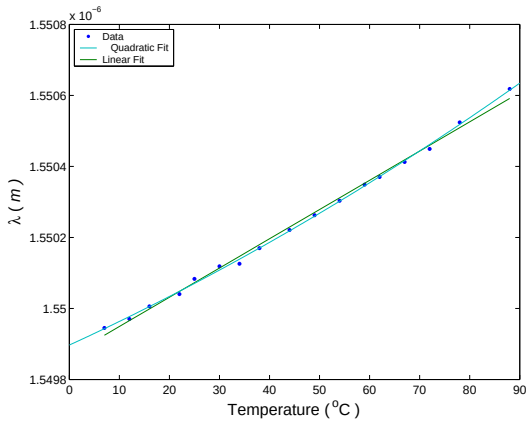

Figure 6.14: Results recorded by gratings subjected to a temperature change from 7^oC to 88^oC.

grating, which yielded 8.3 pm/^oC for this particular grating. However, the temperature control over the reference grating in this case is not as good as in the work reported for the sawtooth waveform and the strain results reported in the next section. A residual of a fit to the points again shows the slightly quadratic nature of the temperature dependence of the Bragg wavelength to temperature.

The mean error over the temperature range reported here when referenced by the grating is ± 15 pm, which corresponds to a temperature resolution of ± 1.5 °C.

Application to Single Parameter Sensing of Strain

To demonstrate the application of the demodulator to the measurement of strain, a 264 nm femtosecond laser inscribed grating was attached to the experimental setup to replace the array of gratings. The grating was inscribed in a 1.3 m length of fibre and both ends of the fibre were fixed to fibre mounts. One of the fibre mounts was mounted on a translation stage and strain applied in 10 $\mu\epsilon$ steps.

Figure 6.15(a) illustrates the capability of the all-fibre demodulator for measurement of strain when referenced from a 1534.14 nm laser. The linear response of the grating to strain can be obtained from the slope of a fit to the points, yielding ~ 1 pm /$\mu\epsilon$. In both cases the tails at the start of the plots are due to the translation stage being moved to take up slack before the fibre was actually being subjected to any strain.

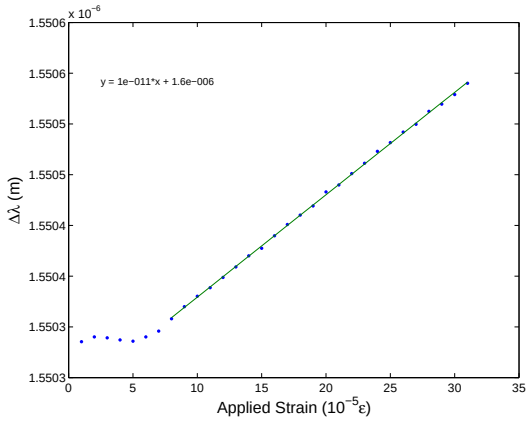

(a) Variation of Bragg wavelength with strain referenced from a 1534.14 nm reference laser

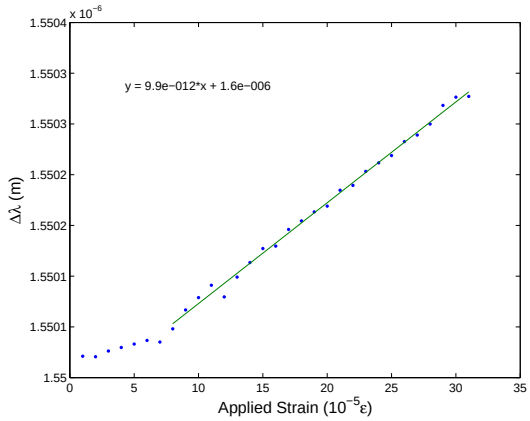

(b) Variation of Bragg wavelength with strain,referenced from a 1566.46 nm reference grating

Figure 6.15: Results recorded by gratings subjected to 10 $\mu\epsilon$ steps, referenced from a 1534.14 nm reference laser and referenced from the 1566.46 nm reference grating.

The efficacy of the demodulator when referenced from the 1566.46 nm reference grating is illustrated in Figure 6.15(b). In this case the slope of a fit yields ~ 0.99 pm/$\mu\epsilon$. The reference grating in this case was temperature stabilised by placing it between two sheets of paper and underneath a bath of water at room temperature.

The results from both the reference laser and reference grating were obtained from interferograms obtained by sweeping an OPD in one arm of the demodulating interferometer by applying a sinusoidal waveform to the piezo-electric controller. The total OPD processed was obtained from the unwrapped phase vector to yield 8.4 mm.

The mean error (referenced from the reference laser) over the range is ± 3 $\mu\epsilon$ which corresponds to a wavelength resolution of ± 3 pm. The mean error over the same range when referenced by the grating is ± 10 $\mu\epsilon$, which corresponds to a wavelength resolution of ± 10 pm. This illustrates the need for tight control over the reference grating temperature, as the wavelength resolution obtained in the last section where the temperature control was not as tightly controlled was ± 15 pm.

6.3.3 Discussion

All-fibre Interferometer

The use of an all-fibre design has several advantages over bulk optic interferometers, chief among which are portability and immunity to vibration. Davis *et al.* [28] have previously applied a fibre Fourier transform spectrometer to the interrogation of an array of FBGs where referencing was based on a 1.319 μm laser using phase locked loop control to provide a highly linear delay scan. However, the configuration reported in [28] required 30 cm delay scans to provide a wavelength resolution of ~ 12 pm. The all-fibre design reported here utilises Hilbert transform processing to achieve ± 3pm wavelength resolution from a processed delay scan of ~ 6.3 mm.

OPD Calibration

Previously reported applications of Hilbert transform processing for calibration of delay [26, 29] have been applied on bulk-optic mechanically scanned interferometers, with calibration based on the temporal phase of a highly stable reference laser. In the work reported here, delay calibration is based on referencing to a temperature stabilised FBG. The efficacy of the referencing scheme based on the interferogram generated from a grating displays identical spectral measurements to a reference interferogram obtained from a highly stable laser (Figure 6.5).

The temperature stabilisation scheme (immersion in a beaker of water) for the reference grating achieved a temperature stability of ± 0.1°C when monitored using thermocouples. While sufficient in laboratory controlled conditions, the same level of stability could not be expected in a variable environment. The extracted phase values, ϕ (=$\omega\tau$), are dependent on the frequency of the light reflected from the reference grating and, therefore, ideally require sub-picometer wavelength stability for accurate delay tracking, as the Hilbert transform technique corrects for common mode non-uniformities in the delay.

Hilbert Transform Spectroscopy

Hilbert transform processing of an array of gratings requires that the individual gratings are filtered in the spectral domain in an intermediate processing step. The minimum wavelength resolution of FTS is dependent on the length of the delay scan. The ~ 6.3 mm scans reported in this chapter provide a wavelength resolution of ~ 380 pm in the Fourier transformation, which is much greater than the spectral bandwidths of the reference and measurand spectra. Figure 6.5 illustrated the identical spectral measurements obtained from the reference laser and grating. However, Figure 6.6 showed that the measurements obtained from the reference grating varied by ~ ± 0.9 pm (corresponding to a ~ 0.09^{o}C change in temperature at the grating site). This variation, and the variation in strain measurements shown in Figure 6.15(b) where thermal control of the grating was not as tight, demonstrate the need to have very good control over the thermal stability of the reference grating.

Quadratic Dependence of the Bragg Wavelength

The quadratic dependence of the Bragg grating temperature coefficients has previously been reported by Flockhart *et al.* [30], and observed in the work reported in chapter 5. The linear strain measurements obtained using the laser reference, illustrated in Figure 6.15(a), when compared to the temperature measurements using an identical interrogation unit and signal processing, as shown in Figure 6.14, illustrate that the quadratic effect is not an artifact of the signal processing techniques reported in this thesis.

6.4 Conclusion

This chapter reports on the development of a grating referenced all-fibre Michelson interferometer for high speed demodulation of grating arrays. FTS and Hilbert transform processing techniques are applied to interferograms obtained on the all-fibre, mechanically scanned Michelson interferometer which is referenced from both a narrow linewidth, temperature stabilised fibre Bragg grating and a highly stable (< 1 pm)

reference laser for comparison. Delay calibration based on both referencing schemes exhibit identical FTS measurements.

The ability of the scheme to demodulate a fibre Bragg grating array is demonstrated and applied to the measurement of both the thermally induced mean wavelength shift and strain induced mean wavelength shift in the light reflected from a single fibre Bragg grating in the array. Grating interrogation is conducted using Hilbert transform spectroscopic techniques where calculation of the mean resonant wavelength of the grating is based on comparison of temporal phase vectors of measurand and reference interferograms obtained in a single scan of the interferometric OPD.

Wavelength resolutions of $\pm \sim 3$ pm are attainable when the configuration is referenced from a source with a highly stable mean wavelength. Also demonstrated is the capability for referencing based on an interferogram obtained from the light reflected from a reference Bragg grating. In this case, the wavelength resolution attained was $\sim \pm 10$ pm. Measurement resolution could be improved by having tighter control over the temperature stability of the grating allied to a narrower linewidth grating.

References

[1] X. Pan, D. Liang, and D. Li, "Optical fiber sensor layer embedded in smart composite material and structure," *Smart Materials and Structures*, vol. 15, pp. 1231–1234, 2006.

[2] D. C. Betz, G. Thursby, B. Culshaw, and W. J. Staszewski, "Identification of structural damage using multifunctional Bragg grating sensors: I Theory and implementation," *Smart Materials and Structures*, vol. 15, pp. 1305–1312, 2006.

[3] D. C. Betz, W. J. Staszewski, G. Thursby, and B. Culshaw, "Structural damage identification using multifunctional Bragg grating sensors: II Damage detection results and analysis," *Smart Materials and Structures*, vol. 15, pp. 1313–1322, 2006.

[4] W. Du, X. M. Tao, H. Y. Tam, and C. L. Choy, "Fundamentals and applications of optical fiber Bragg grating sensors to textile structural composites," *Composite Structures*, vol. 42, pp. 217–229, 1998.

[5] M. A. Davis, D. G. Bellmore, and A. D. Kersey, "Distributed fiber Bragg grating strain sensing in reinforced concrete structural components," *Cement and Concrete Composites*, vol. 19, pp. 45–47, 1997.

[6] H.-N. Li, D.-S. Li, and G.-B. Song, "Recent Applications of Fiber Optic Sensors to Health Monitoring in Civil Engineering," *Engineering Structures*, vol. 26, pp. 1647–1657, 2004.

[7] A. Ezbiri, S. E. Kanellopoulos, and V. A. Handerek, "High resolution instrumentation system for demodulation of Bragg grating aerospace sensors," *Optics Communications*, vol. 150, pp. 43–48, May 1998.

[8] J. Mandal, T. Sun, K. T. V. Grattan, A. T. Augousti, S. A. Wade, S. F. Collins, G. W. Baxter, B. Dussardier, and G. Monnom, "A wide temperature tunable fibre laser using a chirped grating and a type IIA fibre Bragg grating," *Meas. Sci. Technology*, vol. 15, pp. 1113–1119, 2004.

[9] J. H. Lee, J. Kim, Y.-G. Han, S.-H. Kim, and S.-B. Lee, "Investigation of Raman fiber laser temperature probe based on fiber Bragg gratings for long-distance remote sensing applications," *Optics Express*, vol. 12, pp. 1747–1752, April 2004.

[10] M. Buric, J. Falk, and K. P. Chen, "Piezo-electric tunable fiber Bragg grating diode laser for chemical sensing using wavelength modulation spectroscopy," *Optics Express*, vol. 14, pp. 2178–2183, March 2006.

[11] J. A. Siqueira, R. L. leite, and E. C. Ferreira, "Electronic technique for temperature compensation of fibre Bragg gratings sensors," *International Journal of Electronics and Communications*, 2007.

[12] C. Caucheteur, F. Lhomme, K. Chah, M. Blondel, and P. Megret, "Simultaneous strain and temperature senosr based on the numerical reconstruction of polarisation maintaining fiber Bragg gratings," *Optics and Lasers in Engineering*, vol. 44, pp. 411–422, 2006.

[13] E. Udd, "Structural health monitoring using FBGs for aerospace and composite manufacturing," in *18th International Optical Fiber Sensors Conference Technical Digest*, no. MF2, Optical Society of America, Washington DC., 2006.

[14] K. O. Hill and G. Meltz, "Fiber Bragg Grating Technology: Fundamentals and Overview," *Journal Of Lightwave Technology*, vol. 15, pp. 1263–1276, August 1997.

[15] A. G. Simpson, K. Zhou, K. Zhang, L. Everall, and I. Bennion, "Optical sensor interrogation with a blazed fiber Bragg grating and a charged coupled device linear array," *Applied Optics*, vol. 43, pp. 33–40, January 2004.

[16] L. A. Ferreira, E. V. Diatzikis, J. L. Santos, and F. Farahi, "Frequency modulated multimode laser diode for fibre Bragg grating sensors," *Journal of Lightwave Technology*, vol. 16, pp. 1620–1630, September 1998.

[17] K. Peters, P. Pattis, J. Botsis, and P. Giaccari, "Experimental verification of response of embedded optical fiber Bragg grating sensors in non-homogeneous strain fields," *Opticas and Lasers in Engineering*, vol. 33, pp. 107–109, 2000.

[18] A. Arie, B. Lissak, and M. Tur, "Static fiber Bragg grating strain sensing using frequency locked lasers," *Journal of Lightwave Technology*, vol. 17, pp. 1849–1855, October 1999.

[19] S.-C. Ye, S. E. Staines, S. W. James, and R. P. Tatum, "A polarization maintaining fibre Bragg grating interrogation system for multi-axis strain sensing," *Meas. Sci. Technology*, vol. 13, pp. 1446–1449, 2002.

[20] C. Boulet, D. J. Webb, M. Douay, and P. Niay, "Simultaneous interrogation of fiber Bragg gratings using an acousto-optic tunable filter," *IEEE Photonics Technology Letters*, vol. 13, pp. 1215–1217, November 2001.

[21] M. G. Xu, H. Geiger, J. L. Archembault, L. Reekie, and J. P. Dakin, "Novel interrogating system for fibre Bragg grating sensors using an acousto-optic tunable filter," *Electronics Letters*, vol. 29, pp. 1510–1511, August 1993.

[22] Y.-J. Rao, D. J. Webb, D. A. Jackson, L. Zhang, and I. Bennion, "In fiber Bragg grating temperature sensor system for medical applications," *Journal of Lightwave Technology*, vol. 15, pp. 779–785, May 1997.

[23] L. Mandel and E. Wolf, *Optical Coherence and Quantum Optics*. Cambridge University Press, 1995.

[24] S. Huang, M. LeBlanc, M. M. Ohm, and R. M. Measures, "Bragg intragrating structural sensing," *Applied Optics*, vol. 34, no. 22, pp. 5003–5009, 1995.

[25] D. Derickson, *Fibre Optic Test and Measurement*. Prentice Hall, 1998.

[26] D. Flavin, R. McBride, and J. D. C. Jones, "Short-Scan Interferometric Interrogation and Multiplexing of Fibre Bragg Grating Sensors," *Optics Communications*, vol. 170, no. 4-6, pp. 347–353, 1999.

[27] W.-K. Kuo, J.-Y. Kuo, and C.-Y. Huang, "Electro-optic heterodyne interferometer," *Applied Optics*, vol. 46, pp. 3144–3149, June 2007.

[28] M. Davis and A. Kersey, "Application of a Fibre Fourier Transform Spectrometer to the Detection of Wavelength Encoded Signals from Bragg Grating Sensors," *Journal of Lightwave Technology*, vol. 13, no. 7, pp. 1289–1295, 1995.

[29] D. A. Flavin, R. McBride, and J. D. C. Jones, "Short Optical Path Scan Interferometric Interrogation of a Fibre Bragg Grating Embedded in a Composite," *Electronic Letters*, vol. 33, 1997.

[30] G. M. Flockhart, R. R. J. Maier, J. S. Barton, W. N. MacPherson, J. D. C. Jones, K. E. Chisholm, L. Zhang, I. Bennion, I. Read, and P. D. Foote, "Quadratic behaviour of fibre Bragg grating temperature coefficients," *Applied Optics*, vol. 43, no. 13, pp. 2744–2751, 2004.

Chapter 7

Conclusion

7.1 Achievement of Objectives

The objectives of this thesis were; the development of a high resolution Fourier transform spectroscopic (FTS) interrogator for measurement of the light reflected from an array of fibre Bragg gratings (FBG); and the development of an all-fibre interrogator based on Hilbert transform processing (HTP). These have been achieved through the application of interferometric Fourier transform spectroscopy and the associated Hilbert transform processing technique, to interferograms captured using customised interferometric approaches.

FTS is an established spectroscopic tool for spectral measurement and an ideal technique for the measurement of wavelength division multiplexed fibre Bragg gratings. High resolution measurements of the reflected wavelengths from Bragg grating sensors have been obtained when operating in distinct environments. In the reported mechanically scanned interferometric configurations, Hilbert transform processing (HTP) has been shown to provide accurate optical path delay calibration based on the recovery of the respective temporal phase values of co-captured high coherence interferograms. This is despite the accumulating effects of spectral degradation in the **long-scan** case.

FTS and HTP techniques have also been shown to be capable of high resolution measurement of the intra-grating spectral detail of the individual gratings in an array. The efficacy of a scheme based on collinear propagation of the reference and measurand beams in the interrogating interferometer, allowing capture of both reference

and measurand interferograms on a single photodiode, was proven to provide identical spectral measurements to those obtained from a singlemode reference.

HTP processing has also been applied to the high resolution interrogation of fibre Bragg grating (FBG) sensors in an all-fibre interferometric configuration. HTP processing bases measurement of the mean reflected wavelength from a fibre Bragg grating on the ratio of the slope of the extracted temporal phase vector to that of a known reference. The performance of a grating based reference relative to a laser based reference has also been evaluated.

Chapter 1 introduces the work reported in the later chapters. This work is then put into context in the literature review in Chapter 2. The literature review offers a review of the fields of interferometry and optical sensing, with particular focus on sensing using fibre Bragg gratings. The theory of the processing techniques used throughout this thesis is also discussed.

In Chapter 3, the observations on the failure of near infrared (NIR) femtosecond laser inscribed FBGs were made when the gratings were exposed to high optical powers. The analysis was conducted using a drift compensated high resolution interferometric wavelength-shift detection scheme based on comparison of signal and reference phases. Grating spectra were also monitored using an optical spectrum analyser for comparison with the wavelength shifts recorded by the interferometric configuration. Measurements of optically induced wavelength shifts and damage experienced by the gratings when exposed to high optical powers were achieved. The limitations of the interferometric interrogation scheme for interrogation of gratings over extended wavelength ranges were also demonstrated.

In Chapter 4, the Hilbert transform technique for delay calibration was applied to long optical path difference (OPD) scans. The capability of the Hilbert transform technique for delay calibration in a mechanically scanned, customised Michelson interferometric configuration was demonstrated, despite the accumulating effects of non-uniform delay sampling in the Fourier transform. The efficacy of a calibration scheme based on propagation of a 632.8 nm Helium-Neon (HeNe) laser in 1550 nm fibre, where

higher order modes were suppressed using a 50/50 coupler was also investigated and compared to that of a single mode HeNe beam.

The customised Michelson interferometer and long-OPD calibration techniques demonstrated in chapter 4 were applied to the high resolution Fourier transform spectroscopic (FTS) measurement of the light reflected from an array of fibre Bragg gratings in Chapter 5. Both the measurement and reference beams were acquired on a single InGaAs photodetector using collinear propagation of the ~ 1550 nm measurand beam and 632.8 nm reference beam in 1550 nm fibre. Measurement of all of the gratings in the array was made in a single scan of the delay in one arm of the interferometer. The technique was evaluated, in the context of temperature sensing using one of the gratings in the array, relative to the performance of a conventionally parallel propagating single mode reference. The robustness of the technique for measurement of non-uniform temperature gradients was also demonstrated by introducing a chirp across the grating.

In chapter 6, the Hilbert transform processing approach, used in Chapters 4 and 5 for high accuracy calibration of the mechanically scanned delay in the bulk optic interferometer, was applied to interferograms captured in an all-fibre Michelson interferometric configuration. The all-fibre configuration has potential for high measurement bandwidths, and is ideally suited for application in structural health monitoring. This approach demonstrated high resolution, absolute measurements of the mean resonant wavelengths reflected from an array of fibre Bragg gratings. High resolution measurement of the temperature and strain induced grating wavelength shifts was achieved in spite of short delay scans. The efficacy of a technique based on referencing to an interferogram obtained from a reference Bragg grating was analysed and compared to the results where referencing was based on interferograms obtained from a highly stable reference laser.

7.2 Summary of Results

In this section a summary of the results of the individual chapters is given below. The reader is referred to the discussion sections of the relevant chapters for a more detailed discussion on the results.

Chapter 3

Chapter 3 presents observations on optically induced wavelength shifts in NIR femtosecond laser inscribed FBGs, and the implications of the high power losses. NIR inscription involves inducing damage (3 μm spot size) in the core of the fibre producing scattering sites along the length of the grating. The scattering of light into the cladding results in varying temperature increases (~ 40 - 540 °C) at the grating site, with longer gratings showing the greater temperature increases. The optically induced activity can potentially result in damage to the gratings, inducing permanent spectral modification. The implications of spectral modification for the interrogation unit deployed for grating interrogation were also observed, with the spectral broadening incurring a mean measurement of the wavelength shift (1 nm shift for the interferometric phase comparison technique compared to spectral measurements using an OSA of ~ 7 nm).

Chapter 4

The Hilbert transform technique for calibration of the delay in mechanically scanned interferometers was applied to scan lengths > 25x those previously reported in the literature. The efficacy of the technique for long-scan calibration was demonstrated for two reference beams. The first was a transversely singlemode 632.8 nm HeNe beam launched in to a customised Michelson interferometric configuration through 633 nm fibre. The second was a quasi-singlemode HeNe where the 632.8 nm HeNe beam was launched into the interferometer through 1550 nm fibre with suppression of the higher order modes using a wavelength flattened 1330 - 1550 nm 50/50 coupler. Both references exhibited identical spectral recovery, within the resolution of the Fourier transform (1 pm).

Chapter 5

The long-opd configuration demonstrated in Chapter 4 was applied to interrogation of an array of FBGs in Chapter 5. High resolution measurements of the light reflected from the individual gratings in an array were made in a single scan of the interferometric OPD, with both the measurand (~ 1550 nm) and reference (632.8 nm) beams captured on a single InGaAs photodiode. A 240 mm scan length provided a wavelength resolution of ~ 10 pm at 1550 nm. The results when referenced from both the reference beams described in Chapter 4, provided identical measurement within the measurement resolution of the Fourier transform. The results were compared in the context of temperature sensing on one of the gratings. Also demonstrated was a potential measurement range of ~ 900 nm, but more practically could be applied over the entire E, S, C and L telecommunication bands.

Chapter 6

The Hilbert transform techniques for delay calibration used in Chapters 4 and 5 were applied to an all-fibre Michelson interferometric configuration. The all-fibre interferometric configuration was scanned at a frequency 0f ~ 0.5 Hz to provide a delay scan of 6.3 mm. The efficacy of the interrogation unit to provide high resolution measurement when referenced from both a Bragg grating and a telecom laser were evaluated in the context of temperature and strain measurement. High resolution measurement of the reflected wavelengths from an array of FBGs was demonstrated, providing ~ 3 pm wavelength resolution, corresponding to a ~ 0.3 °C temperature resolution or ~ 3 $\mu\epsilon$ strain resolution, was achieved when referencing from a highly stable telecom laser. A ~ 10 pm wavelength resolution, corresponding to a ~ 0.3 °C temperature resolution or ~ 10 $\mu\epsilon$ strain resolution, when referenced from a Bragg grating.

7.3 Future Investigations

Near infrared femtosecond laser inscribed FBG losses

The work reported in Chapter 3 demonstrates the need to have tight control over

grating quality in high power applications. Further investigations are required to fully understand the loss mechanism and to optimise the inscription mechanism. Work needs to be done to minimise such losses, which are not necessarily intrinsic to the femtosecond writing process.

Bulk-optic interferometric interrogation of FBG arrays

The bulk-optic interferometric configuration which was demonstrated in Chapters 4 and 5, where delay calibration is conducted entirely in software using the Hilbert transform technique, could be implemented in an all-fibre configuration. Such a scheme could also provide simultaneous measurement of all of the gratings in an array, potentially spanning a 900 nm range, in a single scan of the interferometric OPD. The scheme would also be capable of providing high resolution measurement of the intra-grating spectral detail, which could be valuable for the detection of non-uniform measurand fields at the grating site. Implementation in an all-fibre configuration would be more suitable for application outside laboratory conditions, where vibration would become more of an issue, introducing further spectral content in the Fourier transform, in a bulk-optic interferometer.

All-fibre Interferometer

The work presented in this thesis shows strong potential for development from the proof of concept stage to commercialisation. All-fibre interferometers are an attractive alternative to bulk-optic interferometers for real world applications because of the ease of removing from laboratory conditions. Higher measurement bandwidths can be achieved with piezo-electric stretchers compared to conventional translation stages, however there is a corresponding decrease in the length of the delay scans ($\sim$ 1 mm @ $\sim$ 900 Hz). However, high resolution measurements of the mean reflected wavelength from a fibre Bragg grating have been reported for far shorter OPD scans using Hilbert transform processing than achievable with conventional FTS, with Flavin *et al.* [1] reporting wavelength resolutions of $\sim$ 7 pm obtained from a 1.2 mm scan.

In the all-fibre interferometric configuration, the gain-bandwidth product of the amplifiers and the maximum sampling rate of the data acquisition card (DAQ) card limited the scanning velocity of the stretcher. The use of amplifiers with higher gain-bandwidth products, cascaded amplifiers, or higher power power broadband sources, such as those based on the supercontinuum effect, in conjunction with higher specification DAQ cards, would allow higher measurement bandwidth.

The demonstration of the different responses to temperature and strain open up the possibility of a single demodulator capable of discriminating between strain and temperature. Simultaneous measurement of strain and temperature has been reported using the first and second order diffraction wavelengths of Bragg gratings [2], where the particular condition that the ratio of the temperature and strain coefficients at both diffraction wavelengths differ must be met.

References

[1] D. Flavin, R. McBride, and J. D. C. Jones, "Short-Scan Interferometric Interrogation and Multiplexing of Fibre Bragg Grating Sensors," *Optics Communications*, vol. 170, no. 4-6, pp. 347–353, 1999.

[2] G. P. Brady, K. Kalli, D. J. Webb, L. Reekie, and J. L. Archambault, "Simultaneous measurement of strain and temperature using the first and second order diffraction wavelengths of Bragg gratings," *Optoelectronics, IEE Proceedings*, vol. 144, pp. 156–161, June 1997.

Appendix A

Electromagnetic Wave Theory

The wave equations describing electromagnetic wave propagation can be derived from Maxwell's equations. These equations can be applied to the analysis of wave propagation in optical fibres once the following assumptions have been made on the physical structure and composition of the waveguide.

- The waveguide is assumed to consist of a linear, isotropic, homogenous, lossless dielectric material without any sources such as currents and free charges aswell as an absence of ferromagnetic medium [1].

Defining **E** as the electric field vector, **D**= ϵ **E** as the electric displacement vector, where ϵ is the permittivity, **H** as the magnetic field vector and **B**= μ**H** as the magnetic flux vector, where μ is the permeability, Maxwell's equations

$$\oint_C \mathbf{E} \cdot dl = -\iint_A \frac{\delta \mathbf{B}}{\delta t} \cdot dS \tag{A.0.1}$$

$$\oint_C \mathbf{B} \cdot dl = \mu_0 \epsilon_0 \iint_A \frac{\delta \mathbf{E}}{\delta t} \cdot dS \tag{A.0.2}$$

$$\oiint_A \mathbf{B} \cdot dS = 0 \tag{A.0.3}$$

$$\oiint_A \mathbf{E} \cdot dS = 0 \tag{A.0.4}$$

can be written as follows: [1,2]

$$\nabla \times \mathbf{E} = -\frac{\delta \mathbf{B}}{\delta t} \tag{A.0.5}$$

$$\nabla \times \mathbf{H} = \frac{\delta \mathbf{D}}{\delta t} \tag{A.0.6}$$

$$\nabla . \mathbf{D} = 0 \tag{A.0.7}$$

$$\nabla.\mathbf{B} = 0 \tag{A.0.8}$$

Wave equations describing the phenomena of electromagnetic fields within an optical waveguide can be obtained by taking the curl of A.0.5 and substituting A.0.6 to get

$$\nabla \times (\nabla \times \mathbf{E}) = -\epsilon\mu \frac{\delta^2 \mathbf{E}}{\delta t^2} \tag{A.0.9}$$

Using the vector identity $\nabla \times (\nabla \times \ ) = \nabla.(\nabla. \ ) - \nabla^2$ provides one homogenous wave equation

$$\nabla^2 E = \epsilon_0 \mu_0 \frac{\delta^2 E}{\delta t^2} \tag{A.0.10}$$

Similarly, for the magnetic field, taking the curl of equation A.0.6 yields the second wave equation

$$\nabla^2 B = \epsilon_0 \mu_0 \frac{\delta^2 B}{\delta t^2} \tag{A.0.11}$$

These are the scalar wave equations for the electric and magnetic field components.

For a guided wave traveling in the z-direction (along the fibre axis) with a radian frequency ω and a propagation constant β, as defined in Section 2.1.3, the electric field vectors are usually defined in cylindrical co-ordinates to be spatially and temporally harmonic phasors [3]

$$E = E_0(r, \phi) e^{i(\omega t - \beta z)} \tag{A.0.12}$$

$$B = B_0(r, \phi) e^{i(\omega t - \beta z)} \tag{A.0.13}$$

Substitution of A.0.13 into A.0.10 and A.0.11 provide

$$\frac{1}{r}\left(\frac{\delta E_z}{\delta \phi} + ir\beta E_\phi\right) = -i\omega\mu B_r \tag{A.0.14}$$

$$i\beta E_r + \frac{\delta E_z}{\delta r} = i\omega\mu B_\phi \tag{A.0.15}$$

$$\frac{1}{r}\left[\frac{\delta}{\delta r}\left(rE_\phi\right) - \frac{\delta E_r}{\delta \phi}\right] = -i\omega\mu B_z \tag{A.0.16}$$

$$\frac{1}{r}\left(\frac{\delta B_z}{\delta \phi} + ir\beta B_\phi\right) = -i\omega\epsilon E_r \tag{A.0.17}$$

$$i\beta B_r + \frac{\delta B_z}{\delta r} = -i\omega\epsilon E_\phi \tag{A.0.18}$$

$$\frac{1}{r}\left[\frac{\delta}{\delta r}\left(rB_\phi\right) - \frac{\delta B_r}{\delta \phi}\right] = -i\omega\epsilon E_z \tag{A.0.19}$$

By eliminating variables these equations can be rewritten such that when E_z and B_z are known the remaining transverse components can be determined [3, 4]. Doing so yields

$$E_r = -\frac{i}{q^2}\left(\beta\frac{\delta E_z}{\delta r} + \frac{\mu\omega}{r}\frac{\delta H_z}{\delta \phi}\right) \tag{A.0.20}$$

$$E_\phi = -\frac{i}{q^2}\left(\frac{\beta}{r}\frac{\delta E_z}{\delta \phi} - \mu\omega\frac{\delta H_z}{\delta r}\right) \tag{A.0.21}$$

$$H_r = -\frac{i}{q^2}\left(\beta\frac{\delta H_z}{\delta r} - \frac{\epsilon\omega}{r}\frac{\delta E_z}{\delta \phi}\right) \tag{A.0.22}$$

$$H_\phi = -\frac{i}{q^2}\left(\frac{\beta}{r}\frac{\delta H_z}{\delta \phi} + \epsilon\omega\frac{\delta E_z}{\delta r}\right) \tag{A.0.23}$$

where $q^2 = \omega^2\epsilon\mu - \beta^2 = k^2 - \beta^2$ Substitution back into A.0.19 results in the wave equation in cylindrical co-ordinates [2–5],

$$\left[\frac{\delta^2}{\delta r^2} + \frac{1}{r}\frac{\delta}{\delta r} + \frac{1}{r^2}\frac{\delta^2}{\delta \phi^2} + \left[k^2 - \beta^2\right]\right]\begin{bmatrix} E_z \\ H_z \end{bmatrix} = 0 \tag{A.0.24}$$

References

[1] R. Kashyap, *Fibre Bragg Gratings.* Optics and Photonics, Academic Press, 1999.

[2] J. L. Arce-Diego, *HandBook of Optical Fibre Sensing Technology: Light and Waveguiding*, ch. 3, pp. 33–55. John Wiley and Sons Ltd., 2002.

[3] G. Keiser, *Optical Fiber Communications.* Electrical and Electronic Engineering, Singapore: McGraw-Hill, 2nd ed., 1991. ISBN 0-07-100785-7.

[4] J. A. Buck, *Fundamentals of Optical Fibres.* New York: Wiley-Interscience, 1995. ISBN 0-471-30818-8.

[5] G. Lachs, *Fibre Optic Communications: Systems, Analysis and Enhancements.* McGraw-Hill, 1998, ISBN:0-07-038279-4.